Single-Shot Optical Sectioning Using Polarised Illumination Coded Structured Illumination Microscopy (picoSIM)

Appelt, Daniel

Awarding institution:
King's College London

Title: Single-Shot Optical Sectioning Using Polarised Illumination Coded Structured Illumination Microscopy (picoSIM)

Author: Daniel Appelt

Single-Shot Optical Sectioning Using Polarised Illumination Coded Structured Illumination Microscopy (picoSIM)

Daniel Appelt

King's College London

Randall Division of Cell and Molecular Biophysics

October 31, 2013

A thesis submitted for the degree of Doctor of Philosophy at King's College London

ABSTRACT

The conventional epi-fluorescent wide-field microscope features a uniform illumination of an extended sample region. A problem arises with this setup since light from out-of-focus fluorophores is also detected. The result is poor quality in the final image, as out-of-focus structures appear blurred; furthermore, their emission light contributes to the background and leads to a reduction in image contrast.

Removing out-of-focus light yields an optically sectioned image: a thin slice of a thick sample that only contains in-focus information. Taking a stack of such sectioned images allows for a three-dimensional (3D) view of the specimen. Structured illumination microscopy for sectioning (sSIM) is a method to obtain optically sectioned data, similar to that obtained from the widely used confocal microscope. However, sSIM suffers from a limited acquisition rate, as at least three individual raw images are needed to reconstruct one sectioned slice.

The technique of polarised illumination coded structured illumination microscopy (picoSIM) combines optical sectioning with high temporal resolution. In picoSIM the individual light patterns needed to acquire the raw sSIM images are encoded in the polarisation of the illumination light. This enables the simultaneous acquisition of the data needed for the sSIM reconstruction, allowing optical sectioning with high acquisition rates. This thesis describes the theory of picoSIM and presents experimental results.

Contents

List of Figures

List of Tables

ACKNOWLEDGEMENTS

I would like to take this opportunity to thank all of the people who supported me in completing my PhD project as well as the British Heart Foundation for funding this work.

I wish to thank my supervisor Rainer Heintzmann for giving me the opportunity to start my PhD in his research group at King's College London. Thank you for your assistance and advice, for having an open ear and a helping hand whenever I needed it.

My special thanks go to Kai Wicker without whose continuous support and guidance this work would not have been possible.

All my colleagues are thanked not only for their professional support but also for making our lab a joyful place to work. In particular, I would like to acknowledge the help of Martin Kielhorn, whose practical advice was invaluable for my experimental work. Also, I would like to thank my second supervisor Elisabeth Ehler for her assistance in the field of biology and for preparing the biological samples.

Thanks to all my proof readers for their comments, particularly to Jonathan Boulle, Kai and Rainer who did the main work.

All my friends are thanked for taking my head away from work and for giving me so many great experiences during the recent years. Special thanks go to Gina for her understanding in times when work seemed to affect my general mood.

Lastly, my deep gratitude goes to my family. The support of my parents and my uncle Karl-Heinz made it possible for me to finish my studies. In particular, I would like to thank my parents for their understanding during my years of exploration.

ABOUT THIS THESIS

This thesis is about the experimental realisation of polarised illumination coded structured illumination microscopy (picoSIM), a fluorescence microscopy technique for obtaining optically sectioned data in a single exposure.

It is addressed to readers familiar with the topic of fluorescence microscopy. However, the first three chapters give a short introduction to the field. After a general introduction given in chapter 1, chapter 2 introduces basic optical concepts needed to understand the following chapters. Chapter 3 explains the theory of picoSIM and structured illumination microscopy (SIM), the microscopy technique behind picoSIM.

Chapter 4 describes the setup, the sample preparation methods and the details of the data acquisition and processing. The experimental results are shown and discussed in chapter 5. Chapter 6 gives an outlook on future work that can be done to advance picoSIM.

1. INTRODUCTION

The conventional epi-fluorescent wide-field microscope features a uniform illumination of an extended sample region. A problem arises with this setup when specimens are used whose thickness in the direction of the optical axis (i.e. the z-direction) is greater than the objective's depth of field. In this case, not only in-focus fluorophores but also those lying above or below the plane of focus are excited. Since the objective is not able to distinguish from which part of the sample the emission light originates, light from out-of-focus fluorophores is also detected. The result is poor quality in the final image, as out-of-focus structures appear blurred; furthermore, their emission light contributes to the background and leads to a reduction in image contrast and signal-to-noise (Fig. 1.1a).

Removing out-of-focus light, i.e. filling the "missing cone" of the optical transfer function (see 2.3.2), yields an optically sectioned image: a thin slice of a thick sample that contains only in-focus information (Fig. 1.1b). Acquiring a stack of sectioned images allows for a 3D reconstruction of the specimen.

Various microscopy techniques have been developed to obtain optically sectioned data. The most-used variant is single spot confocal microscopy [5, 6], where an illumination laser scans the region of interest (ROI) in the sample point-by-point. On the emission side a pinhole physically blocks the out-of-focus light to achieve the desired result. This configuration allows the investigation of thick samples. However, confocal microscopy is inherently limited by scan speed, which is in turn limited by fluorescence saturation.

A method with improved penetration depth is single spot multiphoton scanning microscopy [7], where multiple lower energy photons are used for excitation. Due to the

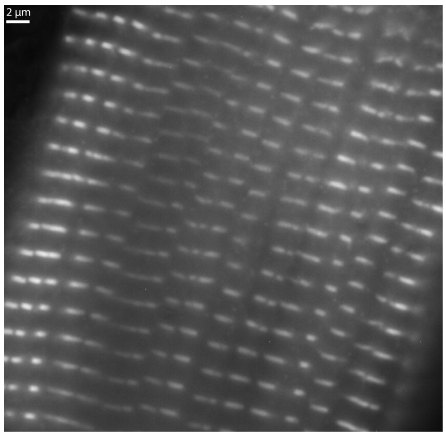

(a) Wide-field fluorescence image

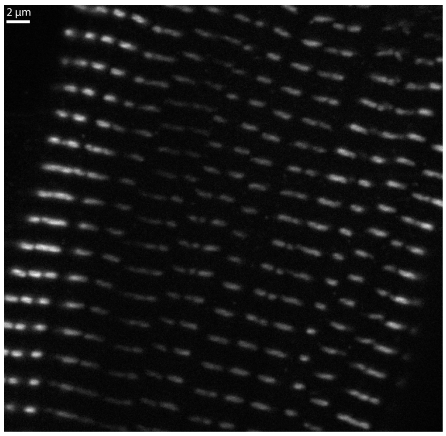

(b) Sectioning SIM reconstruction

Fig. 1.1: Wide-field image versus sSIM reconstruction: Two images of adult rat cardiomyocytes stained with monoclonal mouse antibodies against the titin epitope T12 and secondary Cy2-conjugated anti-mouse immunoglobulin antibodies. The data was acquired with the Zeiss ApoTome and reconstructed in accordance with [3]. *Images adopted from [4].*

non-linear relationship between illumination intensity and absorption probability, more light is absorbed in the focal plane, leading to a suppressed background and thus an optically sectioned image without the necessity of a detection pinhole. Due to the longer wavelength of the illumination light, this method enables deep tissue penetration with reduced phototoxicity in out-of-focus planes. However, the longer wavelength entails a reduced sectioning performance as compared to single spot confocal microscopy.

Spinning disk systems [8–10] are an approach to overcome the speed limitation of the techniques mentioned before by scanning the specimen simultaneously by multiple

illumination beams. However, the multiple pinholes on the detection side result in a reduced axial resolution as out-of-focus light can be detected through an adjacent pinhole; a phenomenon known as pinhole crosstalk. Another limitation is the low light efficiency as the major part of the illumination light is blocked by the pinhole disk. This can be improved by using micro-lenses in combination with the pinhole disk.

A more light efficient spinning disk variant is aperture correlation microscopy [11] where an alternative optical design guarantees the parallel detection of both the wide-field and the sectioned in-focus information. In addition to being more light efficient than conventional spinning disk systems, this variant overcomes the problem of pinhole crosstalk by subtracting the two raw images and thus yields an improved optical sectioning performance. However, as two images have to be acquired simultaneously, the field of view is reduced.

Structured illumination microscopy for sectioning (sSIM) is a non-scanning method to obtain optically sectioned data [3]. A more advanced variant of structured illumination microscopy (SIM), subsequently referred to as high-resolution SIM (hrSIM), can provide optical sectioning combined with a significantly higher resolution in all three dimensions [12, 13]. As a wide-field technique SIM is potentially significantly faster than scanning techniques. However, the need for acquiring at least three individual images for a computational reconstruction of a sectioned image limits the acquisition rate.

All microscopy techniques discussed so far are limited in their acquisition rate. In confocal microscopy and its variants, the scan process is the limiting factor; in SIM it is the requirement to acquire multiple images. Although frame rates above $100 Hz$ have been described [14] none of the above methods allows for imaging fast biological processes taking place on the microsecond time scale.

A fast alternative to single spot two-photon scanning microscopy is wide-field two-photon excitation imaging by multifocal temporal focusing [15], where at each time point several temporally focused [16] diffraction limited spots are non-mechanically scanned across the sample, yielding an axial resolution comparable to that of two-

photon scanning microscopy but on a picosecond timescale.

Selective plane illumination microscopy (SPIM) [17,18] and oblique plane microscopy (OPM) [19] also do not suffer from slow acquisition rates. In addition, photobleaching and phototoxicity are reduced, as only the plane of interest is illuminated. This allows the imaging of biological processes over a long period of time without damaging the sample. However, both variants suffer from a relatively large slice thickness, increasing for larger fields of view. A major drawback of SPIM is the requirement to separate the illumination and emission path. While illuminating the sample from the side, i.e. from a direction perpendicular to the optical axis, allows the illumination of only the focal plane, it entails that conventional glass slide samples cannot be used. Furthermore, it complicates the setup making it difficult to implement SPIM in a conventional wide-field microscope. In contrast to SPIM, OPM uses the same objective lens for illumination and emission. As the excitation of an oblique plane in the sample is achieved by illuminating an off-centre line in the objective's back focal plane (BFP), OPM can be implemented in a conventional wide-field microscope. It therefore allows the imaging of conventional glass slide samples. The use of high *NA* objectives is not possible in SPIM as it requires an objective with a long working distance. In OPM the effective *NA* is decreased as part of the objective's back aperture is used for illumination and another part is used for detection.

The microscopy technique described in this thesis is polarised illumination coded structured illumination microscopy (picoSIM) [20]. It combines optical sectioning with high temporal resolution. In picoSIM the individual light patterns needed for a SIM reconstruction are encoded in the polarisation of the illumination light. This enables the simultaneous acquisition of all raw images in one single exposure, in principle allowing optical sectioning with a temporal resolution limited only by the pulse duration of the laser and, in the case of fluorescence microscopy, the lifetime of the fluorophores. As compared to other high speed optical sectioning techniques like SPIM and OPM, picoSIM in theory has a better sectioning performance over a larger field of view and allows the use of high *NA* objectives.

2. BASIC OPTICAL CONCEPTS

This chapter gives an introduction to some basic optical concepts. Its purpose is to recapitulate some topics that will be needed in the following chapters as well as to introduce the notation used throughout the thesis. Readers not familiar with the field of optics may find it convenient to read a more detailed explanation in the cited literature. Readers not familiar with Fourier optics can find an advanced description of the topic in [21].

2.1 Image of a point source

The performance of any optical imaging system is fundamentally limited by effects associated with the diffraction of light [22].

Here, we assume a self-luminous, monochromatic point-like source in the sample emitting a perfect spherical wave, i.e. emitting light homogeneously in all spatial directions. Due to the limited acceptance angle of the objective lens not all of this light can be captured by the microscope. In the case of an objective lens with a circular aperture, only a cone shaped fraction of the emitted light is collimated into a plane wave and refocused by the tube lens to form an image. The loss of light during the imaging process corresponds to a loss of information about the point source. Consequently, the image is not a perfect copy of the object but rather one of reduced quality [1]. In the specific case of a point-like source, the image resembles a spot of finite size, elongated along the optical axis, i.e. the z-axis as shown in Fig. 2.1. The intensity distribution in this image is referred to as the point spread function (PSF, see 2.2). The PSF is a

[1] Even a perfect 4π objective, capturing all the light emitted by the point source, would not generate a perfect image, as some information present in the near-field is lost in the far-field [23, 24]

characteristic feature of a microscope and can be used to define its resolution capability (see 2.3.1).

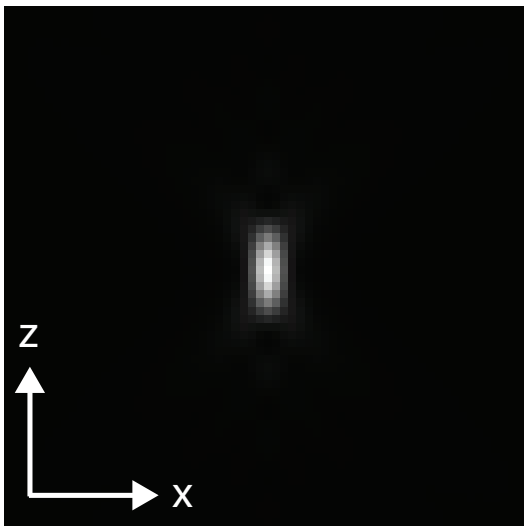

Fig. 2.1: Simulated wide-field point spread function (PSF): A point source in the sample generates an intensity distribution, referred to as PSF, in the image. Due to the loss of information during the imaging process, the image resembles a spot of finite size, elongated along the optical axis, i.e. the z-axis. The PSF used here was obtained from a simulation which is based on the vectorial high-NA theory [25, 26] and was written by Rainer Heintzmann and Peter Vermeer.

2.2 Point spread function and optical transfer function

This section follows the explanations in [27].

The intensity distribution in the image can be seen as a superposition of plane waves approaching under different angles. The higher the angle of incidence, the higher the lateral frequency k of the pattern the waves contribute to form the image in the camera plane.

The Fourier transform (FT) of an image reveals its spatial frequency spectrum, which corresponds to its information content. High spatial frequencies in the FT correspond to fine details whereas low spatial frequencies carry the information about brightness in the image.

For a point source situated in the origin of sample space and emitting light with a

single wavelength, all k-vectors lie on the so-called Ewald sphere [28], centred at the origin in k-space (Fig. 2.2a). The radius of the sphere is defined by the wavelength of the emission light and the refractive index of the optical medium; the k-vector's angle represents the propagation angle of the corresponding plane wave. The frequencies contributing to the image of the point source are defined by the acceptance angle of the objective lens, represented by the objective's pupil function. Projecting the pupil function onto the Ewald sphere yields a part of a spherical shell that represents the k-vectors available to form the image. This so-called McCutchen generalised aperture [29] corresponds to the amplitude transfer function (ATF) which defines the k-vectors of the field distribution in the image of the point source (Figs. 2.2a and 2.2b). The inverse FT of the ATF yields the amplitude point spread function (APSF), which corresponds to the field distribution in the image generated by the point emitter in the sample. The intensity distribution generated by this emitter is the PSF. It can be calculated as the absolute square of the field distribution (APSF). An auto-correlation of the ATF yields the optical transfer function (OTF, Figs. 2.2d and 2.2c). Alternatively the OTF can be obtained from the FT of the PSF.

2.3 Resolution in microscopy

2.3.1 Real space considerations

If a sample consists of two mutually incoherent emitters situated at the same z-position, the image will be the sum of their two PSFs. The closer the emitters in the sample, the more their PSFs will overlap. Eventually, they will form one spot that cannot be identified as having been generated by two rather than one point source. The lateral resolution of a microscope is defined as the minimum lateral distance of the two emitters in the sample that still enables to distinguish them in the image. According to the Rayleigh criterion, the two emitters are distinguishable, i.e. they can be resolved, if the distance between the intensity maxima of their PSFs is greater than or equal to the distance between the PSF's maximum and its first minimum [30]. The Sparrow

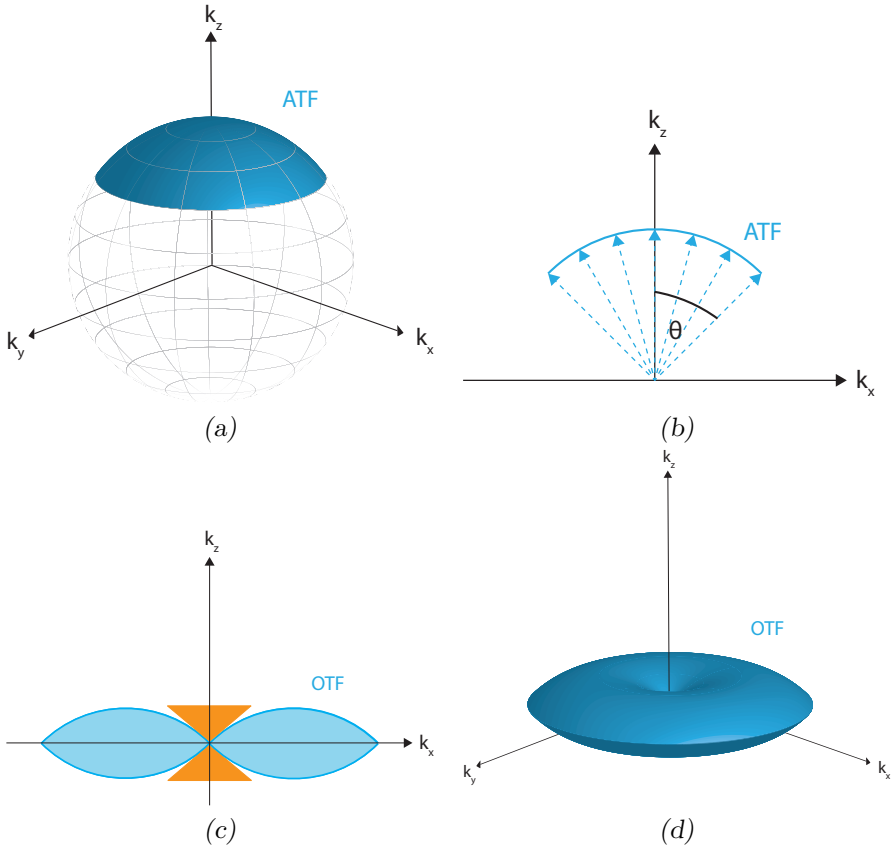

Fig. 2.2: ATF and OTF: (a) The Ewald sphere (shown in grey), centred at the origin in k-space, defines all k-vectors of the light emitted by a monochromatic point source. Projecting the objective's pupil function onto the Ewald sphere yields the ATF (shown in blue), which defines all k-vectors accepted by the optical system and hence contributing to the imaging process. (b) is a 2D illustration of the ATF with θ denoting the half acceptance angle of the objective lens. The blue arrows represent a fraction of the k-vectors defined by the ATF. Their length is defined by the wavelength of the emitted light and the refractive index of the optical medium whereas their angle corresponds to their propagation direction (c) An auto-correlation of the ATF, i.e. a convolution of the ATF($\vec{k}$) with its mirrored complex conjugate ATF$^*(-\vec{k})$, yields the OTF (here in 2D). The "missing cone" around the k_z-axis, leading to out-of-focus light in the conventional wide-field image, is shown in orange. A 3D representation of the OTF support is shown in (d).

criterion defines the two emitters as resolvable as long as their image exhibits a central intensity dip between their summed PSFs [31].

According to [27] the PSF, on which the above definitions are based on, is not the ideal parameter to define the resolution of a microscope. Digital filters can be

retroactively applied to an image to change the width of a PSF. This can lead to a resolution improvement according to the above criteria without gaining additional sample information.

2.3.2 Fourier space considerations

A less ambiguous way to judge the performance of a microscope is a Fourier space consideration using the OTF [27].

Like the PSF, the OTF is also characteristic for the microscope in question. It defines which information about the object, i.e. which spatial frequencies, are transmitted in the imaging process and contribute to the image. In this process of imaging, the microscope acts as a low-pass filter. The maximum lateral spatial frequency k_{max} that can be transmitted is defined by the support of the OTF (Fig. 2.2d) and can be used to judge the lateral resolution of the microscope:

$$k_{max} = 2\pi \frac{2NA}{\lambda_{em}} , \tag{2.1}$$

where λ_{em} is the wavelength of the emission light and NA the numerical aperture of the objective:

$$NA = n \sin(\theta) , \tag{2.2}$$

where n denotes the refractive index of the medium between the objective lens and the sample coverslip and θ the half acceptance angle of the objective lens as depicted in Fig. 2.2b.

The extent of the OTF in the k_z-direction defines the z-resolution of the microscope. Object frequencies beyond the support of the OTF are lost during the imaging process and cannot be retrieved by conventional means. Figures 2.2c and 2.2d depict the OTF of a conventional wide-field microscope. The missing frequencies around the k_z-axis,

referred to as the "missing cone", are the cause of the out-of-focus light being present in the image of a conventional wide-field microscope.

The inverse of k_{max} (multiplied by 2π) is the Abbe limit of resolution [22] which defines the smallest resolvable grating period d_{min} as:

$$d_{min} = \frac{\lambda_{em}}{2NA} \, . \tag{2.3}$$

2.4 Image formation in Fluorescence Mircoscopy

Due to the emission light in fluorescence microscopy being incoherent, the 3D image of a sample consisting of multiple point emitters can be obtained by summing the individual PSF images of all points. Mathematically, this can be described as a convolution of the local fluorophore distribution in the sample $S(\vec{r})$ and the PSF $h(\vec{r})$, which is assumed to be shift invariant:

$$I(\vec{r}) = [S \otimes h](\vec{r}) \, , \tag{2.4}$$

with $\vec{r} = (x, y, z)$ denoting the spatial sample coordinate and $\otimes$ the convolution operator. Following the Convolution Theorem, a convolution in real space corresponds to a multiplication in Fourier space. Equation 2.4 therefore can be written as:

$$\tilde{I}(\vec{k}) = \tilde{S}(\vec{k})\tilde{h}(\vec{k}) \, , \tag{2.5}$$

where $\tilde{}$ denotes the FT of the respective function, $\vec{k} = (k_x, k_y, k_z)$ the spatial frequency and $\tilde{h}(\vec{k})$ the OTF.

Both Eqs. 2.4 and 2.5 assume a homogeneous illumination of the sample. If the

sample is instead illuminated with an illumination intensity $I_{illu}(\vec{r})$, depending on the sample coordinate, Eq. 2.4 will become:

$$I(\vec{r}) = [(I_{illu}S) \otimes h](\vec{r}) \; . \tag{2.6}$$

Similarly, Eq. 2.5 becomes:

$$\tilde{I}(\vec{k}) = [\tilde{I}_{illu} \otimes \tilde{S}](\vec{k})\tilde{h}(\vec{k}) \; . \tag{2.7}$$

Here, a linear relationship between the emitted intensity $[I_{illu}(\vec{r})S(\vec{r})]$ and the illumination intensity $I_{illu}(\vec{r})$ is assumed. This linear relationship is true for all microscopy techniques described in chapter 3. However, microscopes utilising a non-linear sample response are also in use [32–34].

The transition from 3D to 2D is necessary to obtain the intensity distribution imaged onto the camera:

$$I(\vec{r}_{xy}) = [(I_{illu}S) \otimes h](\vec{r})\Big|_{z=0} \; . \tag{2.8}$$

Projecting $\tilde{I}(\vec{k})$ along k_z yields the FT of the 2D image in the camera plane:

$$\tilde{I}(\vec{k}_{xy}) = \int_{-\infty}^{+\infty} [\tilde{I}_{illu} \otimes \tilde{S}](\vec{k})\tilde{h}(\vec{k})\, dk_z \; . \tag{2.9}$$

2.5 Polarisation

PicoSIM is based on the idea of illuminating a microscope sample with a distribution of polarised light. To understand the mathematical description of picoSIM in 3.2.2, this

section introduces the tools to mathematically describe polarised light.

Light can be treated as a transverse electromagnetic wave, i.e. the electric field vector $\vec{E}$ is perpendicular to the light wave's propagation vector $\vec{k}$. Polarisation is defined by the orientation of $\vec{E}$ at a certain point of the wave over time [23]. If the orientation of the electric field is constant, the light is referred to as linear polarised. If the scalar amplitude of $\vec{E}$ is constant and the vector makes one complete rotation during one oscillation period of the wave, the light is circular polarised. Depending on the direction of rotation, one speaks of right-circular and left-circular polarised light respectively. Both linear polarised and circular polarised light are special cases of elliptically polarised light. Elliptical polarisation means that $\vec{E}$ both rotates and changes its magnitude. Natural light consists of an incoherent superposition of light waves with different polarisation states and is therefore referred to as randomly polarised. [1]

2.5.1 The Stokes parameters

In 1852 G. G. Stokes introduced four parameters to describe the polarisation state of an incoherent beam of light [1]. These so-called Stokes parameters S_0, S_1, S_2 and S_3 are commonly arranged in the form of a column vector, the Stokes vector $\vec{S}$:

$$\vec{S} = \begin{pmatrix} S_0 \\ S_1 \\ S_2 \\ S_3 \end{pmatrix} = \begin{pmatrix} I_{total} \\ I_x - I_y \\ I_{45^\circ} - I_{-45^\circ} \\ I_{\circlearrowright} - I_{\circlearrowleft} \end{pmatrix} . \tag{2.10}$$

As described in [35], the first element S_0 represents the overall intensity I_{total} while S_1, S_2 and S_3 determine the state of polarisation. When investigating the beam of light in question using a polarisation filter, S_1 equals the difference of the intensity I_x (transmitted by a linear polariser whose transmission axis is horizontal) and I_y (transmitted by a linear polariser whose transmission axis is vertical). The third element S_2 is equal to the difference in intensity I_{45° (transmitted by a linear polariser whose transmission axis is at 45°) and I_{-45° (transmitted by a linear polariser whose transmission axis is

at $-45°$). The fourth element S_3 represents the difference in intensity transmitted by a right-circular polariser (i.e. a polariser that transmits right-circular polarised light) $I_{\circlearrowright}$ and a left-circular polariser (i.e. a polariser that transmits left-circular polarised light) $I_{\circlearrowleft}$. Thus, following [1], S_1 indicates whether the beam of light tends to be horizontally polarised ($S_1 > 0$), vertically polarised ($S_1 < 0$) or whether its orientation is not in favour of one of these directions ($S_1 = 0$). Likewise, S_2 indicates whether the light tends to be linearly polarised at $45°$ ($S_2 > 0$), at $-45°$ ($S_2 < 0$) or neither ($S_2 = 0$). Similarly, S_3 shows whether the light tends to be right-circularly polarised ($S_3 > 0$), left-circularly polarised ($S_3 < 0$) or neither ($S_3 = 0$). Hence, with normalised Stokes parameters (normalised by dividing each parameter by the value of S_0) natural light can be represented by the Stokes vector $\vec{S} = (1, 0, 0, 0)$. The Stokes vectors for the basic polarisation states are listed in Table 2.1. [1]

State of polarisation	Stokes vector
linear, $0°$	$\begin{pmatrix} 1 \\ 1 \\ 0 \\ 0 \end{pmatrix}$
linear, $90°$	$\begin{pmatrix} 1 \\ -1 \\ 0 \\ 0 \end{pmatrix}$
linear, $45°$	$\begin{pmatrix} 1 \\ 0 \\ 1 \\ 0 \end{pmatrix}$
linear, $-45°$	$\begin{pmatrix} 1 \\ 0 \\ -1 \\ 0 \end{pmatrix}$
right circular	$\begin{pmatrix} 1 \\ 0 \\ 0 \\ 1 \end{pmatrix}$
left circular	$\begin{pmatrix} 1 \\ 0 \\ 0 \\ -1 \end{pmatrix}$

Tab. 2.1: Stokes vectors for some basic polarisation states [1, 2]

2.5.2 Mueller matrix formalism

The polarisation state of a beam of light, and correspondingly its Stokes vector, can be altered when passing an optical element. This corresponds mathematically to a multiplication of the Stokes vector of the incident light $\vec{S_i}$ with the 4×4 transformation matrix $\mathbf{T}$, characteristic for the optical element in question:

$$\vec{S_t} = \mathbf{T}\vec{S_i} \ , \tag{2.11}$$

where $\vec{S_t}$ is the Stokes vector of the transmitted wave. This matrix method was devised by Hans Mueller and is therefore known as Mueller matrix formalism. The Mueller matrices for some optical elements are listed in Table 2.2. [1]

Optical element	Mueller matrix
linear polariser at 0°	$\frac{1}{2}\begin{pmatrix} 1 & 1 & 0 & 0 \\ 1 & 1 & 0 & 0 \\ 0 & 0 & 0 & 0 \\ 0 & 0 & 0 & 0 \end{pmatrix}$
linear polariser at 90°	$\frac{1}{2}\begin{pmatrix} 1 & -1 & 0 & 0 \\ -1 & 1 & 0 & 0 \\ 0 & 0 & 0 & 0 \\ 0 & 0 & 0 & 0 \end{pmatrix}$
linear polariser at angle α	$\frac{1}{2}\begin{pmatrix} 1 & \cos(2\alpha) & \sin(2\alpha) & 0 \\ \cos(2\alpha) & \cos^2(2\alpha) & \sin(2\alpha)\cos(2\alpha) & 0 \\ \sin(2\alpha) & \sin(2\alpha)\cos(2\alpha) & \sin^2(2\alpha) & 0 \\ 0 & 0 & 0 & 0 \end{pmatrix}$
$\lambda/4$-plate, fast axis at 45°	$\begin{pmatrix} 1 & 0 & 0 & 0 \\ 0 & 0 & 0 & -1 \\ 0 & 0 & 1 & 0 \\ 0 & 1 & 0 & 0 \end{pmatrix}$
$\lambda/4$-plate, fast axis at $-45°$	$\begin{pmatrix} 1 & 0 & 0 & 0 \\ 0 & 0 & 0 & 1 \\ 0 & 0 & 1 & 0 \\ 0 & -1 & 0 & 0 \end{pmatrix}$

Tab. 2.2: Mueller matrices for some optical elements [1, 2]

2.6 Fluorescence anisotropy

In picoSIM it is crucial that the emission light retains at least part of the polarisation of the excitation light (see 3.2.1). Fluorescence anisotropy describes the extent to which the emission light keeps the polarisation of the excitation light. [36]

Assuming a two-state model, the dipole character of a fluorophore entails that it only absorbs light with a polarisation component parallel to the fluorophore's transition dipole moment. This property is commonly known as photoselection. Likewise, the light emitted by the fluorophore will be polarised along this fixed axis in the fluorophore. However, flouorophores are not static: their transition moment may rotate within the fluorescence lifetime, causing the electric field vector of the emission light to no longer be parallel to that of the excitation light.

As suggested in [36], a setup to measure the fluorescence anisotropy for a specific sample is depicted in Fig. 2.3. The sample is illuminated with linear polarised light. On the emission side of the system, the fluorescence is detected through a linear polariser. The intensity $I_{\parallel}$ is measured with the polariser oriented parallel to the polarisation direction of the excitation light. When measuring $I_{\perp}$, the emission polariser is oriented perpendicular to the direction of the input polarisation. The fluorescence anisotropy r then calculates to:

$$r = \frac{I_{\parallel} - I_{\perp}}{I_{\parallel} + 2I_{\perp}} \,. \tag{2.12}$$

For the simplified case, assuming the fluorophore resembling a sphere, the time-resolved fluorescence anisotropy is given by:

$$r(t) = r_0 e^{-t/\tau_c} \,, \tag{2.13}$$

with r_0 being the maximum anisotropy and τ_c the rotational correlation time. A flu-

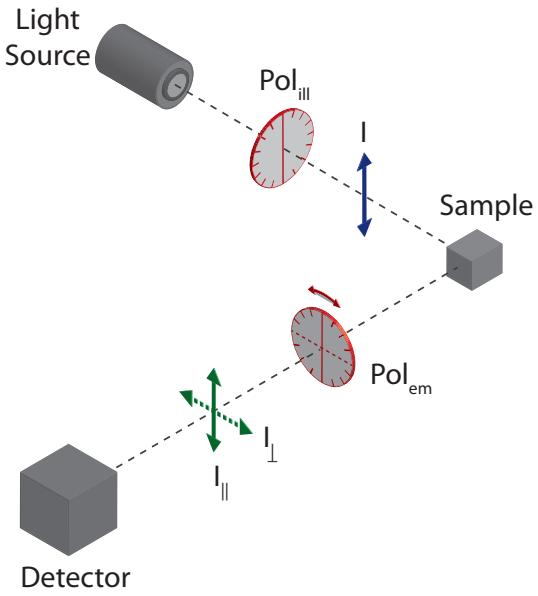

Fig. 2.3: Setup for measurement of fluorescence anisotropy: The sample is illuminated with linearly polarised light. The angle of polarisation (indicated by the blue arrow) is defined by a polarisation filter Pol_{ill} in the illumination beam path. The fluorescent emission light is detected through a polarisation analyser Pol_{em} whose transmission axis can be rotated in the direction indicated by the red arrows. Pol_{em} is positioned to be parallel (orthogonal) to the polarisation of the illumination light to detect $I_{\parallel}$ ($I_{\perp}$) (polarisation direction indicated by the green arrows). From the detected intensities $I_{\parallel}$ and $I_{\perp}$, the fluorescence anisotropy r can be calculated.

orescence anisotropy of $r_0 = 1$ can only be observed for oriented samples (or in the non-fluorescent case for scattered light). Homogeneous unoriented samples will always lead to lower values due to the angular dependence of photoselection. For a single photon process the value can be as high as $r_0 \leq 0.4$ [37]. In [38], the anisotropy for different fluorophores in solution has been measured to values of $r_0 = 0.019$ for Fluorescein, $r_0 = 0.27$ for Erythrosin and $r_0 = 0.28$ for Rose Bengal. For large molecules such as Green Fluorescent Protein (GFP), values of $r_0 \geq 0.32$ (in solution) have been described [39].

The main cause for a rotation of the transition dipole moment within the fluorescence lifetime is rotational diffusion [36]. This becomes clear when considering that the rotational correlation time τ_c is reciprocally proportional to the rotational diffusion coefficient D_τ:

$$\tau_c = \frac{1}{6D_\tau} \, . \tag{2.14}$$

According to the Stokes-Einstein equation the rotational diffusion coefficient - and with it the rotational correlation time - depends on the Temperature T, the hydrodynamic molecular volume of the fluorophore V and the viscosity of the surrounding medium η [36]:

$$D_\tau = \frac{RT}{6V\eta} \, . \tag{2.15}$$

In addition to rotational diffusion, the anisotropy depends on a possible binding of the fluorophore to a macromolecule [36]. This fact is especially important when dealing with fluorescence microscopy where fluorophores are widely used to label molecules. A labelled macromolecule with a rotational correlation time which is large compared to the fluorophore lifetime will decrease rotational diffusion and increase anisotropy. Furthermore, the linker between the fluorophore and the labelled molecule must be taken into account, as it may be rigid or allow the rotation of the fluorophore around the linker axis and thus influence the anisotropy.

The binding of the fluorophore to a macromolecule not only influences the anisotropy but can also lead to a preferred orientation of the fluorophores within the sample. This can be the case if the macromolecule itself exhibits a preferred orientation, e.g. along a structure within a cell. In picoSIM, a preferred orientation can cause artefacts in the final image.

In summary, an ideal specimen for picoSIM exhibits a high anisotropy value, which is homogeneous over the entire sample. Moreover, an even distribution and a random orientation of the fluorophores is desired.

3. THEORY OF STRUCTURED ILLUMINATION MICROSCOPY

Parts of this chapter including figures have been published in [4] D. Appelt and R. Heintzmann, Structured Illumination Microscopy (SIM), in Encyclopedia of Biophysics, G. Roberts, ed. (Springer, 2013).

This chapter explains the theory of picoSIM (see 3.2). To understand the benefit of this technique and how it works, it is necessary to first become familiar with SIM, the microscopy method which is the basic concept behind picoSIM. Hence, the first section of this chapter is dedicated to SIM (see 3.1). The picoSIM setup explained in chapter 4.1 is capable of removing out-of-focus light, the lateral resolution improvement is not relevant. Consequently, it is more so related to sSIM than to hrSIM (see chapter 1). However, there are two reasons why the first section of this chapter deals with both variants of SIM (sSIM and hrSIM). First, the picoSIM setup employs coherent illumination as does hrSIM rather than incoherent illumination as does sSIM. Second, a reconstruction algorithm developed for hrSIM is used to reconstruct the picoSIM data presented in chapter 5, since, in contrast to the sSIM algorithm, it is able to correct experimental parameters not according perfectly to theory (see 4.4.2).

3.1 SIM

Structured illumination microscopes are characterised by their use of spatially modulated light to illuminate the sample. Figure 3.1 shows the typical setup used for SIM. The main component is the illumination mask, inserted at the field diaphragm position in the illumination path of a conventional fluorescence microscope. The illumination mask, which is typically a line-grating, is projected onto the sample and can be shifted

along the lateral axis by well-defined displacements.

A typical data set obtained from a structured illumination apparatus comprises a z-stack of image sets, each set corresponding to a different focus position in the sample. Each image set contains images acquired with different positions of the illumination pattern in sample space. Variants of SIM like sSIM and hrSIM differ with respect to the light source used for illumination (incoherent for sSIM and coherent for hrSIM respectively) as well as with respect to the required image processing.

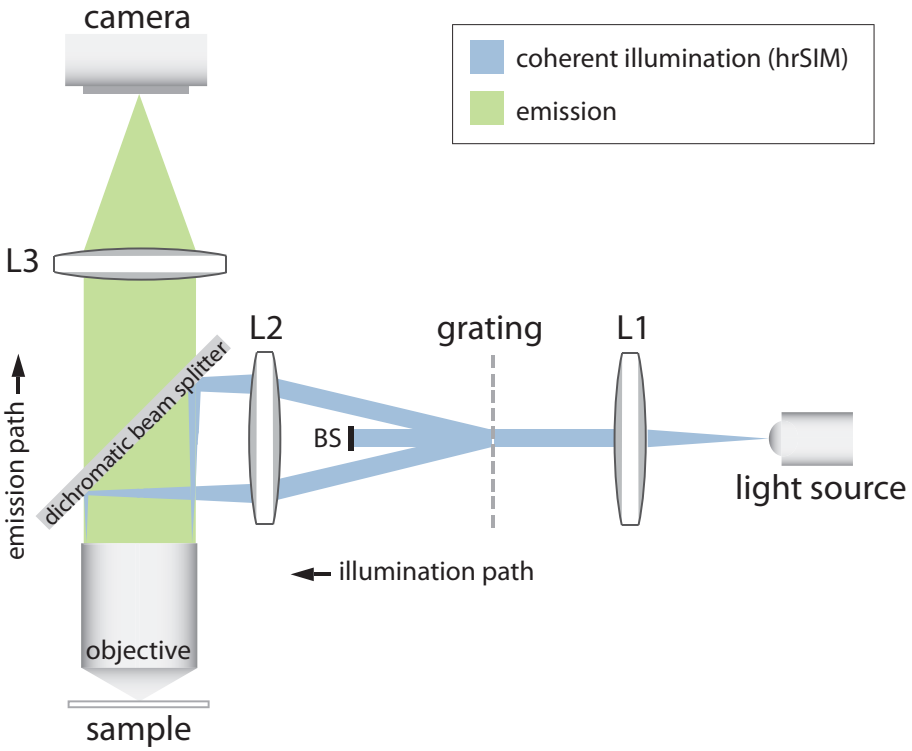

Fig. 3.1: Setup for SIM employing coherent two-beam illumination: The illumination mask, which is typically a line-grating, is inserted at the field diaphragm position in the illumination path of a conventional wide-field fluorescence microscope and projected onto the sample using an incoherent (not depicted) and a coherent light source for sSIM and hrSIM, respectively. The beam stop BS blocks the 0^{th} order leading to a two-beam illumination. Lenses L1, L2 and the objective are in telecentric arrangement. The tube lens L3 directs the light onto the camera.

All derivations in this section assume a two-beam illumination setup yielding a standing wave (i.e. sin^2) intensity pattern in the objective's focal plane (see appendix A.1).

3.1.1 Optical sectioning - sSIM

sSIM - Principle

One benefit of sSIM is its property of removing out-of-focus light (Fig. 1.1). During this process an algorithm is applied to the set of images taken at a specific focus position to yield an optical section of the sample. One set consists typically of three raw images with relative illumination pattern phases of 0°, 120° and 240° (Fig. 3.2). From these three images one final, optically sectioned image can be calculated. As mentioned before, it is common to use a line-grating as the illumination mask. To achieve optical sectioning a grating, relatively coarse (approx. 900 nm periodicity in sample space for a 63×, 1.4 *NA* oil immersion objective) compared to the resolution limit, illuminated by an incoherent light source is used.

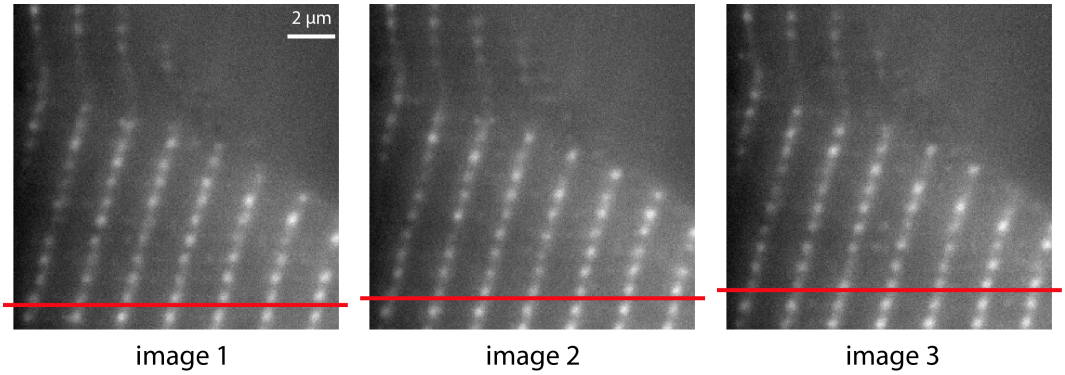

Fig. 3.2: The sSIM raw images: Three raw images are necessary for the sSIM reconstruction algorithm. Each image is acquired at a different position of the grating in sample space. For illustration purposes the same grid line is marked with a red bar in each image. Specimen: Adult rat cardiomyocytes, stained with monoclonal mouse antibodies against the titin epitope T12 and secondary Cy2-conjugated anti-mouse immunoglobulin antibodies.

It is possible to identify, based on the detected intensity variation over the three images, the part of the sample from which the light originated. Due to the use of incoherent light to illuminate the grating, the contrast of the illumination pattern in sample space is lower for out-of-focus planes. Consequently, the degree of modulation over the three images is strongest for the in-focus slice. Out-of-focus structures experience a

reduced degree of modulation, or, if they lie distinctly outside of the focal plane, no modulation at all. Accordingly, the intensity of light emitted by in-focus structures (Fluorophore II in Fig. 3.3) is not constant over the three images, whereas that of light emitted by out-of-focus structures (Fluorophore I in Fig. 3.3) is.

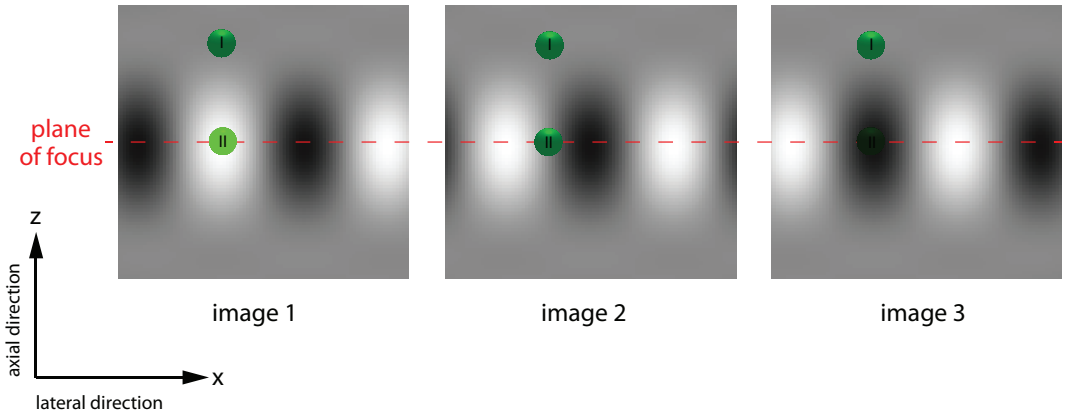

Fig. 3.3: The sSIM principle: Simulation of a x-z cross section through sample space showing the illumination distribution in the three raw sSIM images and the effect of the varying grating position on the light intensity emitted from fluorophores I and II. Due to the decreasing contrast of the illumination pattern for out-of-focus planes, the displacement of the grating leads to an intensity modulation for the in-focus fluorophore II, but not the out-of-focus fluorophore I. The reconstruction algorithm compares the intensity in each pixel over the three images and suppresses the unmodulated out-of-focus part.

The degree of modulation further depends on the 3D distribution of fluorophores in the sample. Since neighbouring fluorophores may experience the intensity modulation with a different phase, the overlap of their images can result in a decrease of the modulation effect. Due to blurring, the mutual overlap and thus the decrease in modulation is far greater for out-of-focus regions than for the focal slice.

The reconstruction algorithm compares the intensity in each pixel over the three images, retaining the modulated component and suppressing the unmodulated part. Hence, both incoherent illumination and the detected out-of-focus blurring contribute to the sectioning effect of sSIM. However, the need for a high-contrast illumination pattern in the focal slice and the best filling of the "missing cone" calls for a relatively coarse grating to be used, under incoherent illumination; a grating which is too coarse

to achieve an in-plane resolution improvement as featured by hrSIM.

sSIM - Image formation

The mathematical description of sSIM is based on [20]. Assuming a sinusoidal line-grating being incoherently imaged into the sample, the illumination intensity distribution $I_{illu,n}(\vec{r})$ can be described as:

$$I_{illu,n}(\vec{r}) = \frac{A}{2}\left[\delta(z)[1+\cos(\vec{k}_{illu}\cdot\vec{r}+\frac{2\pi n}{3})]\right]\otimes h_{illu}(\vec{r}) \quad , n=(1,2,3)\ , \tag{3.1}$$

where $\vec{r}=(x,y,z)$ is the spatial sample coordinate, A the amplitude of the sinusoidal grating, $\delta(z)$ the Dirac delta function, $\vec{k}_{illu}$ the grating's k-vector in reciprocal sample coordinates (which is assumed to have lateral components k_x and k_y only) and $h_{illu}(\vec{r})$ the illumination PSF. The index n designates the image number and thereby the phase position of the grating in sample space.

The emitted light intensity $I_{em,n}(\vec{r})$ is assumed to be proportional to the local fluorophore distribution in the sample $S(\vec{r})$ and to the local illumination intensity $I_{illu,n}(\vec{r})$:

$$I_{em,n}(\vec{r}) = I_{illu,n}(\vec{r})S(\vec{r})\ . \tag{3.2}$$

The imaging process can then be described as a convolution of the emitted intensity distribution $I_{em,n}(\vec{r})$ with the detection PSF $h_{det}(\vec{r})$, yielding a two-dimensional (2D) image on the camera:

$$I_n(\vec{r}_{xy}) = [I_{em,n}\otimes h_{det}](\vec{r})\Big|_{z=0}\ . \tag{3.3}$$

sSIM - Image reconstruction

From the three raw images $I_1(\vec{r}_{xy})$, $I_2(\vec{r}_{xy})$ and $I_3(\vec{r}_{xy})$ the sectioned image $I_{sSIM}(\vec{r}_{xy})$ can be calculated by [3]:

$$I_{sSIM}(\vec{r}_{xy}) = \sqrt{[I_1(\vec{r}_{xy}) - I_2(\vec{r}_{xy})]^2 + [I_2(\vec{r}_{xy}) - I_3(\vec{r}_{xy})]^2 + [I_3(\vec{r}_{xy}) - I_1(\vec{r}_{xy})]^2}\,, \tag{3.4}$$

which is mathematically identical to:

$$I_{sSIM}(\vec{r}_{xy}) = |\sum_{n=1}^{3} I_n(\vec{r}_{xy}) \quad exp(\imath\frac{2\pi n}{3})|\,, \tag{3.5}$$

where $\imath = \sqrt{-1}$ is the imaginary unit.

sSIM - Filling the missing cone

As shown in appendix A.2, when omitting constant factors, Eq. 3.5 can be written as [20]:

$$I_{sSIM}(\vec{r}_{xy}) = |[(mS) \otimes h'_{det}](\vec{r})|\Big|_{z=0}\,, \tag{3.6}$$

with the sample modulation function (Fig. 3.4):

$$\begin{aligned} m(\vec{r}) &= \delta(z) \otimes [h_{illu}(\vec{r}) exp(\imath\vec{k}_{illu} \cdot \vec{r})] \\ &= \mathcal{F}^{-1}\{\delta(k_x)\delta(k_y)\tilde{h}_{illu}(\vec{k} - \vec{k}_{illu})\}(\vec{r}) \end{aligned} \tag{3.7}$$

and the effective detection PSF:

$$\begin{aligned} h'_{det}(\vec{r}) &= exp(\imath\vec{k}_{illu}\cdot\vec{r})h_{det}(\vec{r}) \\ &= \mathcal{F}^{-1}\{\tilde{h}_{det}(\vec{k}-\vec{k}_{illu})\}(\vec{r}) \ , \end{aligned} \tag{3.8}$$

where $\mathcal{F}^{-1}$ denotes the inverse FT of the respective function. It can be seen from Eq. 3.8 that the effective detection OTF $\tilde{h}'_{det}(\vec{k}) = \tilde{h}_{det}(\vec{k}-\vec{k}_{illu})$ is shifted to the position of the illumination pattern's k-vector in Fourier space (Fig. 3.4a). Hence, sample information around the k_z-axis can be retrieved, filling the "missing cone" of the conventional wide-field OTF. Due to the modulus in Eq. 3.6 the imaging process is no longer a linear convolution of the sample with a PSF. However, the reconstructed sSIM image will contain frequency information from within the support of the OTF [27]:

$$\tilde{h}_{sSIM}(\vec{k}) = \tilde{m}(\vec{k}) \otimes [\tilde{h}'_{det}(\vec{k}) + \tilde{h'}_{det}(-\vec{k})] \ . \tag{3.9}$$

As can be seen in Fig. 3.4b, $\tilde{h}_{sSIM}(\vec{k})$ not only fills the "missing cone" but also extends the transmitted frequency spectrum in all three dimensions. Extending the frequency support corresponds to a resolution improvement (see 2.3.2). However, due to the coarse grating being used in sSIM, the lateral resolution improvement is not appreciable.

3.1.2 Resolution improvement - hrSIM

hrSIM - Principle

By utilising a smaller grating in sample space and more complex image processing, hrSIM employing two-beam illumination can alternatively provide optical sectioning or a significantly improved resolution in the lateral plane. The resolution improvement is associated with the moiré effect, which occurs when two high-frequency patterns are multiplied. Since the illumination of the sample corresponds mathematically to a multiplication of the illumination pattern (Fig. 3.5a) with fine details of the sample

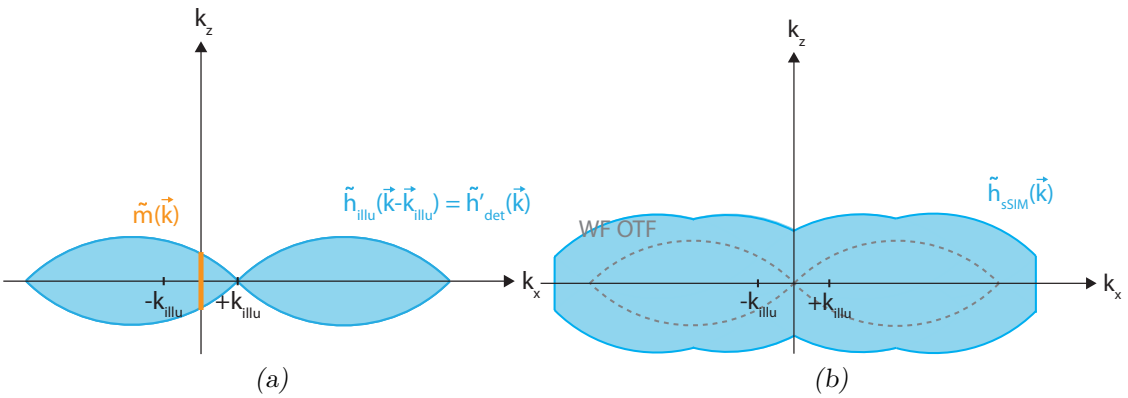

Fig. 3.4: Filling the "missing cone" in two-beam sSIM: (a) shows the modulation function $\tilde{m}(\vec{k})$, a direct consequence of the incoherent illumination in sSIM. Together with the shifted detection OTF $\tilde{h}'_{det}(\vec{k})$ shown in blue, it leads to an extended support of the effective sSIM OTF $\tilde{h}_{sSIM}(\vec{k})$ compared to the conventional wide-field OTF (shown in grey) as can be seen in (b). This extended support not only fills the "missing cone" of the wide-field OTF around the k_z-axis but also increases the resolution in all three dimensions. However, due to the coarse grating used in sSIM the lateral resolution improvement is not relevant.

structure (Fig. 3.5b), hrSIM entails a moiré effect. The multiple moiré images (one of them is shown in Fig. 3.5c) obtained during the hrSIM data acquisition process, in combination with knowledge of the illumination pattern, allow one to infer details of the sample structure that are not detected in a conventional microscope. For a more complete explanation, a description in Fourier space must be considered (see next section).

In order to obtain a significant in-plane resolution improvement, an illumination pattern with a sufficiently fine structure (approx. 200 nm grating periodicity in sample space for a 63×, 1.4 *NA* oil immersion objective) must be used. To ensure an isotropic effect in all in-plane directions, one usually acquires, at each focus position, three image sets, each with a different orientation of the grating in the x-y plane. For a setup employing two-beam illumination, one image set consists usually of three images with different positions of the illumination structure in sample space. In order to achieve 100% illumination contrast at the finest possible generated illumination structure, a spatially coherent light source is used.

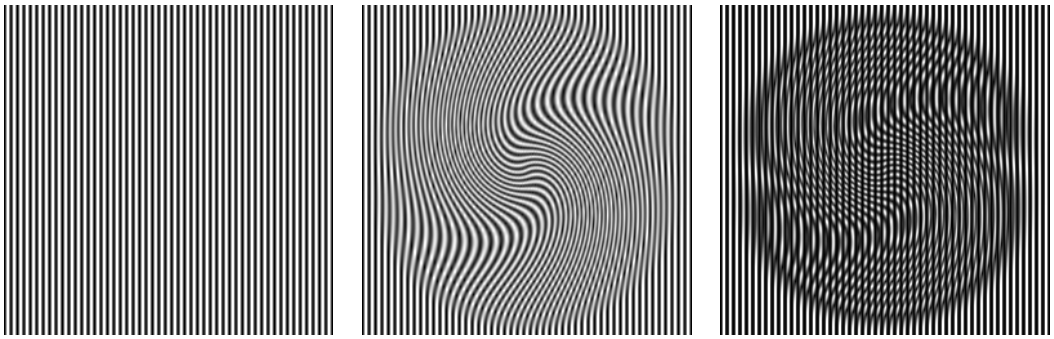

(a) Illumination pattern *(b)* Sample *(c)* Moiré pattern

Fig. 3.5: The moiré effect in hrSIM: (a) A high-frequency illumination pattern. If multiplied with a sample (b), containing fine details that cannot be resolved by the optical system, a moiré pattern forms (c). The illumination pattern is known and can be removed computationally; through this procedure, which implies the acquisition of multiple moiré images (c), each with a different position of the illumination pattern in sample space, otherwise undetectable structures can be uncovered.

In addition to the sectioning effect, a lateral resolution improvement up to a factor of two (slightly higher due to the wavelength of the illumination light being smaller than that of the emission light) is possible with this approach compared to conventional wide-field microscopy. However, the lateral resolution improvement competes with the sectioning performance (see "hrSIM - Filling the missing cone" below). A two-beam hrSIM setup optimised for in-plane resolution improvement yields no optical sectioning. In practice, two-beam hrSIM is mostly used when imaging thin samples, or in total internal reflection microscopy (TIRFM), where optical sectioning is achieved by other experimental means. If both optical sectioning and resolution improvement is required, a hrSIM setup employing three-beam illumination is the best option. Such a system can improve the resolution in all three dimensions. Three-beam illumination SIM systems are not discussed in this thesis.

hrSIM - Image formation

A mathematical analysis allows the image reconstruction process to be understood in more detail [27]. According to the image formation described for sSIM (see 3.1.1), the emitted intensity $I_{em}(\vec{r})$ is considered to be proportional to the local fluorophore

distribution $S(\vec{r})$ and to the local illumination intensity $I_{illu}(\vec{r})$:

$$\begin{aligned} I_{em}(\vec{r}) &= [\delta(x)\delta(y)\delta(z-z_0) \otimes S(\vec{r})]I_{illu}(\vec{r}) \\ &= S^{(z_0)}(\vec{r})I_{illu}(\vec{r}) \ . \end{aligned} \tag{3.10}$$

Here, z_0 denotes the focus position of the sample. Refocussing the sample to the focus position $z = z_0$ corresponds to physically moving the sample by a distance of z_0. The illumination intensity, only depending on the position of the objective, is unaffected by any movement of the sample. This multiplication in real space corresponds to a convolution in Fourier space:

$$\tilde{I}_{em}^{(z_0)}(\vec{k}) = [e^{-\imath k_z z_0}\tilde{S}(\vec{k})] \otimes \tilde{I}_{illu}(\vec{k}) \ . \tag{3.11}$$

A coherent two-beam illumination will generate a standing wave illumination pattern $I_{illu}(\vec{r})$ with constant contrast along the z-direction in the sample (see appendix A.1). Its FT $\tilde{I}_{illu}(\vec{k})$ corresponds to three delta peaks:

$$I_{illu}(\vec{r}) = \frac{A}{2}[1 + \cos(\vec{k}_{illu} \cdot \vec{r} + \phi)] \ , \tag{3.12}$$

$$\tilde{I}_{illu}(\vec{k}) = \frac{A}{2}\left[\delta(\vec{k}) + \frac{1}{2}[e^{-\imath\phi}\delta(\vec{k} + \vec{k}_{illu}) + e^{\imath\phi}\delta(\vec{k} - \vec{k}_{illu})]\right] \ , \tag{3.13}$$

where A is the amplitude of the illumination pattern and $\vec{k}_{illu}$ its k-vector in reciprocal sample coordinates (which is assumed to have lateral components k_x and k_y only). The variable ϕ designates the phase of the pattern and thereby the position of the grating in sample space.

Equation 3.11 thus yields a sum of $M = 3$ Fourier-transformed objects (Fig. 3.6c), referred to as object components of order m (with $m = -1, 0, +1$). Note that two of

the three object components are displaced from the centre position by the illumination patterns k-vector $\vec{k}_{illu}$. Only the conventional wide-field component remains unshifted. The position and shape of the illumination mask in real space determines the individual position, strength, and complex phase of the object components in Fourier space.

The imaging process, a convolution of $I_{em}^{(z_0)}(\vec{r})$ with the detection PSF $h_{det}(\vec{r})$ in real space, can be described as a multiplication of the FT of the emitted intensity distribution $\tilde{I}_{em}^{(z_0)}(\vec{k})$ with the detection OTF $\tilde{h}_{det}(\vec{k})$ in Fourier space. A projection along k_z yields the 2D Fourier image in the camera plane $\tilde{I}^{(z_0)}(\vec{k}_{xy})$:

$$\tilde{I}^{(z_0)}(\vec{k}_{xy}) = \int_{-\infty}^{+\infty} \sum_m A_m e^{\imath m\phi} \left[[e^{-\imath k_z z_0} \tilde{S}(\vec{k})] \otimes \delta(\vec{k} - m\vec{k}_{illu}) \right] \cdot \tilde{h}_{det}(\vec{k})\, dk_z \ , \quad (3.14)$$

where A_m is the amplitude of the m^{th} component. Figure 3.6d shows that only low object frequencies of the unshifted wide-field component lie within the detection passband defined by $\tilde{h}_{det}(\vec{k})$. In consequence, high spatial frequencies, which correspond to fine details of the sample, are lost during the conventional wide-field imaging process (Fig. 3.6b). In hrSIM the shifted object components compensate for some of this loss. Due to their displacement in Fourier space, higher object frequencies are shifted into the transmittable region of the detection passband and thus contribute to the image (Fig. 3.6d).

hrSIM - Image reconstruction

Taking a set of three 2D images, each with a different phase position of the grating in the sample, allows for computational separation of the individual components and shifting them back to their correct position in Fourier space (Fig. 3.6e). For optimal performance, overlapping information, stemming from different separated components, is averaged with frequency dependent weights (Fig. 3.6f). Repeating this process for at least three different orientations of the grating yields a reconstructed image with

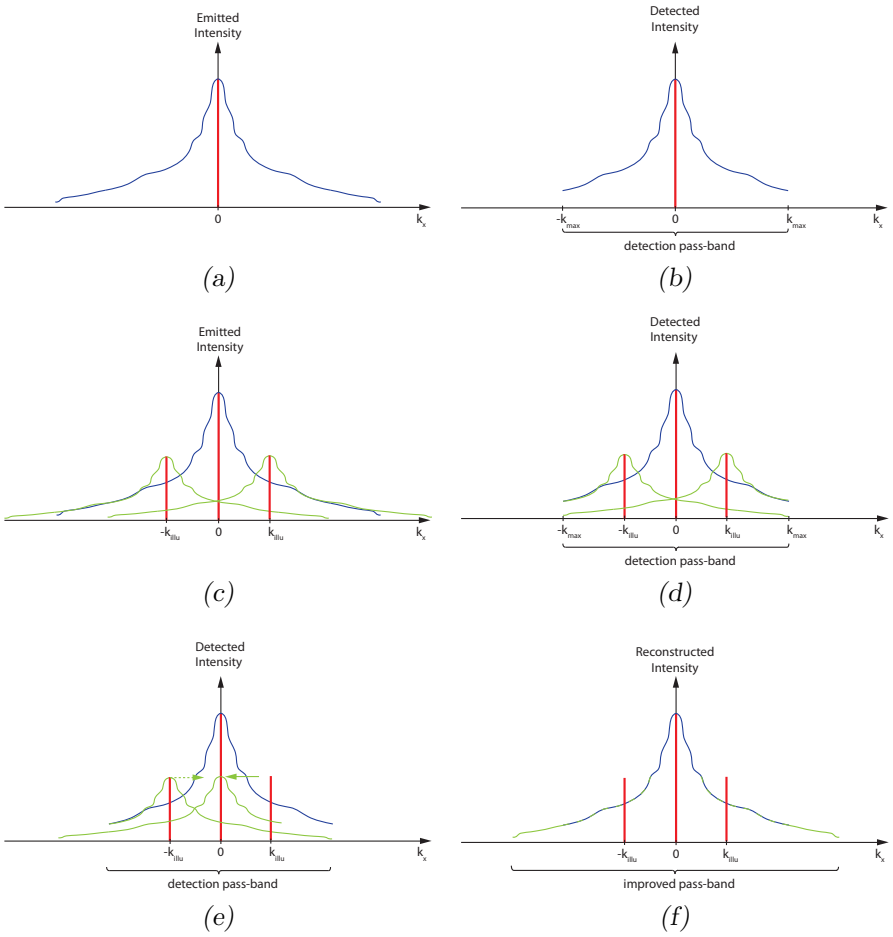

Fig. 3.6: The hrSIM image formation and reconstruction principle: (a) Uniform illumination in a conventional wide-field microscope leads to a delta peak (red bar) centred in Fourier space denoting the position of the Fourier-transformed object (blue) in the emitted light distribution. (b) The process of optical imaging corresponds to a multiplication of the emitted light distribution with the OTF (the shape of the OTF is assumed to be rectangular for illustration purposes) in Fourier space. The optical system acts therein as a low-pass filter. High spatial frequencies, i.e., $|k_{xy}| > k_{max}$, are lost during the conventional wide-field imaging process. (c) The FT of the emitted light distribution in a two-beam illumination hrSIM device yields, in addition to the conventional component (blue), two side components (green) located at $\pm\vec{k}_{illu}$. The frequency information in each of the side components is the same as in the conventional component but shifted. (d) Due to their displacement the low-pass filter acts asymmetrically with respect to the shifted side components and therefore transmits object frequencies formerly rejected. (e) After computational separation of the individual components both side components can be shifted to the correct position in Fourier space. (f) The combination of all components, using weighted averaging, leads to an improved passband and hence to an improved resolution.

near-isotropic lateral resolution enhancement.

The linear sample response leads to the Abbe limits for detection and illumination being combined, yielding a new, extended limit of:

$$k_{max,hrSIM} = k_{max} + k_{illu} \ . \tag{3.15}$$

As the Abbe limit defines the smallest sample structure that can be resolved by the optical system (see 2.3.2), this extension corresponds to a lateral resolution enhancement.

Note that Fig. 3.6 only illustrates the resolution improvement in the lateral plane. The optical sectioning that can be achieved with a two-beam hrSIM system employing coherent illumination is depicted in Fig. 3.7 in the next section.

For a detailed mathematical description of the hrSIM reconstruction process see appendix A.3.

hrSIM - Filling the missing cone

The lateral resolution improvement possible with hrSIM has already been depicted in Fig. 3.6. Figure 3.7 is a 2D representation that illustrates the improved support of the reconstructed hrSIM image both in the lateral and the axial direction.

Although the coherent two-beam illumination of hrSIM employs an intensity pattern with no modulation along z (see appendix A.1), hrSIM can yield optically sectioned images; the shifted object components being present in the Fourier-transformed raw images not only allow to extend the lateral support (Fig. 3.7b) but also to fill the "missing cone" (Fig. 3.7c). The extent to which either of these are done depends on the position of the shifted object components, i.e. on the illumination patterns k-vector $\vec{k}_{illu}$.

In summary, a two-beam hrSIM system optimised for optical sectioning can fill the "missing cone" but not extend the frequency support along k_z to higher frequencies as a two-beam sSIM setup employing incoherent illumination can do. A two-beam hrSIM

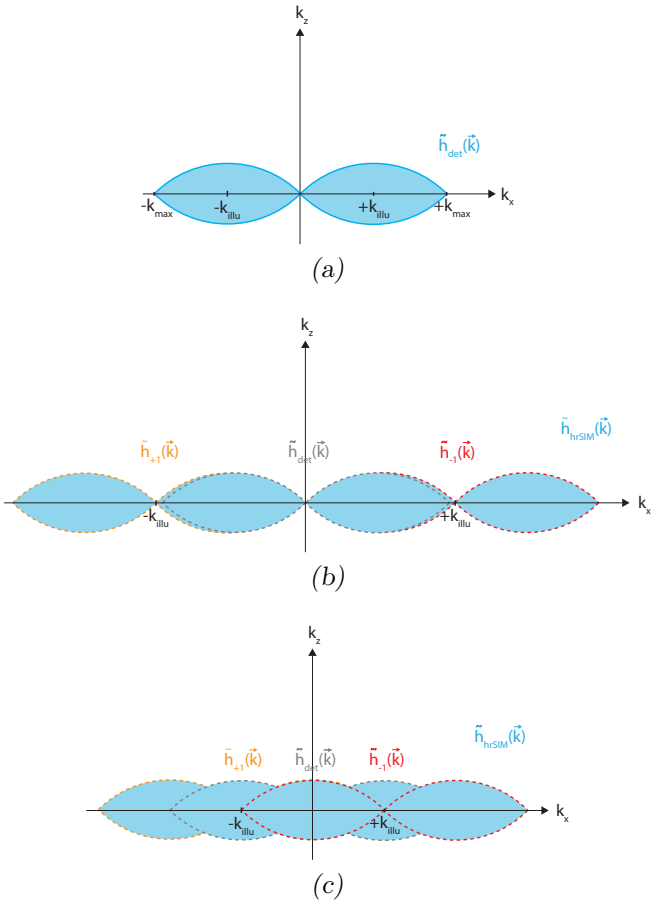

Fig. 3.7: Filling the "missing cone" in two-beam hrSIM: (a) shows the detection OTF $\tilde{h}_{det}(\vec{k})$. Due to the structured illumination there are multiple object components (not shown) present in each of the raw images; the 0^{th} order component at the zero frequency position in k-space and the $+1^{st}$ (-1^{st}) order component at the position of the illumination pattern's k-vector $\vec{k}_{illu}$ $(-\vec{k}_{illu})$. In the course of the hrSIM reconstruction, the higher order object components are shifted to their true frequency positions in k-space. As can be seen from Eq. A.15, this corresponds to an extension of the frequency support by the effective component specific OTFs $\tilde{h}_{-1}(\vec{k})$ and $\tilde{h}_{+1}(\vec{k})$. The extended frequency support $\tilde{h}_{hrSIM}(\vec{k})$ is shown in (b) and (c). A hrSIM system optimised for lateral resolution improvement does not fill the "missing cone" as can be seen in (b). Consequently, it yields no optical sectioning but a lateral resolution improvement slightly higher than twice the value of k_{max}. (c) shows that a hrSIM setup can be optimised for optical sectioning. The "missing cone" is optimally filled for $\vec{k}_{illu} = 0.5\vec{k}_{max}$. However, there is still no resolution improvement along z.

system optimised for an in-plane resolution improvement cannot fill the "missing cone" but can extend the support in the lateral direction to values slightly higher than twice the value of k_{max}, exceeding the performance of a sSIM system by far. A significant

resolution improvement in all three dimensions requires a hrSIM setup utilising three-beam illumination [40].

3.2 Single-shot optical sectioning - picoSIM

3.2.1 picoSIM - Principle

In contrast to SIM, which employs an intensity modulated illumination pattern, picoSIM is based on the idea of illuminating the sample with a light distribution of homogeneous brightness but varying linear polarisation, with the lateral polarisation component depending linearly on the lateral sample coordinate, e.g. the x-coordinate as defined in Fig. 3.8. If the light emitted by the sample retains at least part of the polarisation of the illumination light, as in the case of reflection microscopy or fluorescence microscopy with high anisotropy, a polarisation analyser in the emission path will transmit light with a certain angle of linear polarisation and partially reject light with a different polarisation angle. Hence, the light distribution imaged onto the camera resembles the detected light distribution in SIM (Fig. 3.8).

In conventional SIM, a shift of the illumination pattern can be achieved by altering the illumination accordingly. In contrast, the position of the effective illumination pattern in picoSIM is determined retroactively by the orientation of the polarisation analyser in the emission beam path (Fig. 3.8).

Splitting the emission light into three identical components and filtering each of them using a polarisation analyser oriented at a different angle allows for acquiring the three images necessary for SIM in one single exposure.

3.2.2 picoSIM - Mathematical description

The mathematical description of picoSIM is based on [20]. The angle of illumination with respect to the optical axis is assumed to be small in this derivation. This is a justifiable assumption if one assumes a low-NA objective being used. The low angle condition allows to apply the Mueller matrix formalism (see 2.5.2) to describe the

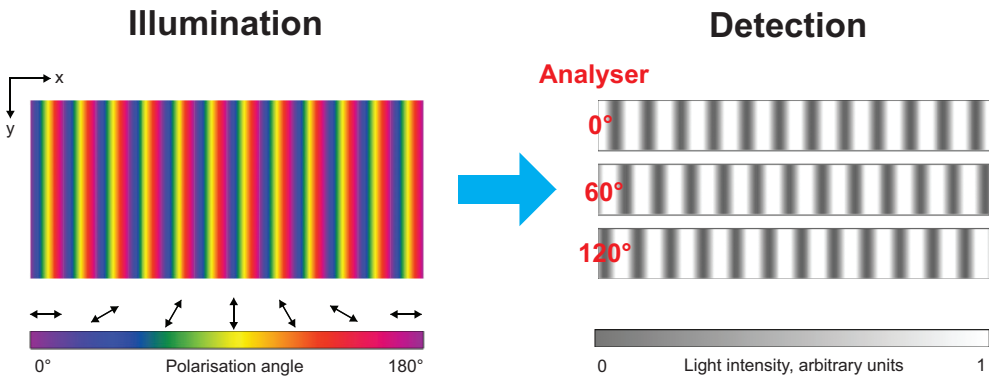

Fig. 3.8: The picoSIM illumination light distribution in sample space for small angles of illumination: In picoSIM, the sample is illuminated with linearly polarised light of constant intensity over the whole field of view. However, the polarisation direction of the illumination light (left part) varies with the lateral sample coordinate (here the x-coordinate). Each colour depicted corresponds to light with a well defined angle of linear polarisation. If the emission light retains the polarisation distribution of the illumination light (due to high fluorescence anisotropy), a polarisation analyser in the emission beam path will define the effective illumination pattern imaged onto the camera. Depending on its orientation it will transmit light with a certain angle of linear polarisation. A rotation of the polarisation analyser will result in a phase shift of the pattern (right part). *Figure redrawn from [41].*

incoherent, partially polarised light. It also allows the independent treatment of the Stokes vector components. In practice, low angles of illumination can lead to a deviation from theory as will be discussed in 5.1.1 and 5.1.2.

Illumination

In order to obtain the incoherent illumination intensity $\vec{I}_{illu}(\vec{r})$, a distribution of polarised light is generated by filtering a sheet of unpolarised light, represented by the Stokes vector $\vec{s}(\vec{r}) = (\delta(z), 0, 0, 0)$, by a linear polariser, represented by the Mueller matrix $\mathbf{F}(\vec{r}) = \mathbf{P}(\alpha(\vec{r}))$ [2]:

$$\mathbf{P}(\alpha(\vec{r})) = \frac{1}{2}\begin{pmatrix} 1 & \cos(2\alpha) & \sin(2\alpha) & 0 \\ \cos(2\alpha) & \cos^2(2\alpha) & \sin(2\alpha)\cos(2\alpha) & 0 \\ \sin(2\alpha) & \sin(2\alpha)\cos(2\alpha) & \sin^2(2\alpha) & 0 \\ 0 & 0 & 0 & 0 \end{pmatrix}, \tag{3.16}$$

with a position dependent linear polarisation $\alpha(\vec{r}) = \frac{1}{2}\vec{k}_{illu} \cdot \vec{r}$. Here, $\vec{k}_{illu}$ was chosen in analogy to the grating's k-vector in SIM. The sheet of polarised light is then imaged into the sample:

$$\begin{aligned} \vec{I}_{illu}(\vec{r}) &= [(\mathbf{F}\vec{s}) \otimes h_{illu}](\vec{r}) \\ &= \Big[\delta(z)[1, \cos(\vec{k}_{illu} \cdot \vec{r}), \sin(\vec{k}_{illu} \cdot \vec{r}), 0]\Big] \otimes h_{illu}(\vec{r}) \ , \end{aligned} \tag{3.17}$$

where each element of the Stokes vector can independently be convolved with the illumination PSF $h_{illu}(\vec{r})$.

Emission

The emitted light intensity $\vec{I}_{em}(\vec{r})$ can be obtained by a multiplication of the illumination intensity $\vec{I}_{illu}(\vec{r})$ with the local fluorophore distribution $S(\vec{r})$. In this step we have to account for the emitted light only retaining a fraction m_{an} of the input polarisation due to fluorescence anisotropy. This leads to:

$$\vec{I}_{em}(\vec{r}) = S(\vec{r})\left(\Big[\delta(z)[1, m_{an}\cos(\vec{k}_{illu} \cdot \vec{r}), m_{an}\sin(\vec{k}_{illu} \cdot \vec{r}), 0]\Big] \otimes h_{illu}(\vec{r}) \right) . \tag{3.18}$$

Imaging

The imaging process can be described as a convolution of the emitted light distribution $\vec{I}_{em}(\vec{r})$ with the detection PSF of the optical system $h_{det}(\vec{r})$:

$$\vec{I}_{out}(\vec{r}) = [\vec{I}_{em} \otimes h_{det}](\vec{r}) \ . \tag{3.19}$$

However, before this light distribution reaches the camera it passes a polarisation filter oriented at an angle β. The effect of the filter element can be expressed by a multiplication with the linear polariser operator $\mathbf{P}(\beta)$, yielding the final light distribution in the camera plane $\vec{I}_\beta(\vec{r}) = \mathbf{P}(\beta)\vec{I}_{out}(\vec{r})$. Since the camera is insensitive to the state of polarisation and only detects the intensity distribution, only the first component of the resulting stokes vector $[\vec{I}_\beta(\vec{r})]_1$ is of interest, corresponding to a 2D image in the camera plane:

$$[\vec{I}_\beta(\vec{r}_{xy})]_1 = \left\{ S(\vec{r}) \left(\left[\delta(z)[1 + m_{an}\cos(\vec{k}_{illu} \cdot \vec{r} - 2\beta)] \right] \otimes h_{illu}(\vec{r}) \right) \right\} \otimes h_{det}(\vec{r}) \Big|_{z=0} . \tag{3.20}$$

This is equivalent to one of the raw images acquired using an intensity modulated illumination pattern as in SIM, albeit with a pattern contrast reduced by a factor m_{an}. Splitting the emission light into three identical beams, each of which is then directed onto a polarisation analyser oriented at a different angle, allows the acquisition of the three SIM raw images in one single exposure.

3.2.3 picoSIM - Implementation

Since a linear polariser with a position dependent orientation was not available, the picoSIM illumination light distribution described in Eq. 3.17 was generated by other experimental means.

The SIM illumination pattern can be generated by interference of the -1^{st} and $+1^{st}$ diffraction orders of a physical grating in sample space. In picoSIM, these linearly polarised diffraction orders are circularly polarised in opposite directions (left- and right-handed respectively) by means of $\lambda/4$-plates. Their superposition in sample space then leads to the polarised illumination pattern shown in Fig. 3.8.

The situation in sample space is depicted in Fig. 3.9. The -1^{st} and $+1^{st}$ diffraction

orders are projected onto the sample by the objective lens. Since the plane waves impinge on the sample under a certain angle of incidence, different points of the same wave-front reach the sample temporally delayed. Due to this, the phase of the electric field vector in the sample depends on the lateral sample coordinate. The superposition of the left- and right-circularly polarised waves, stemming from the -1^{st} and $+1^{st}$ diffraction orders, yields a sum field vector of fixed orientation in time, with a direction depending on the phases of the circularly polarised illumination orders, and hence the desired polarisation pattern.

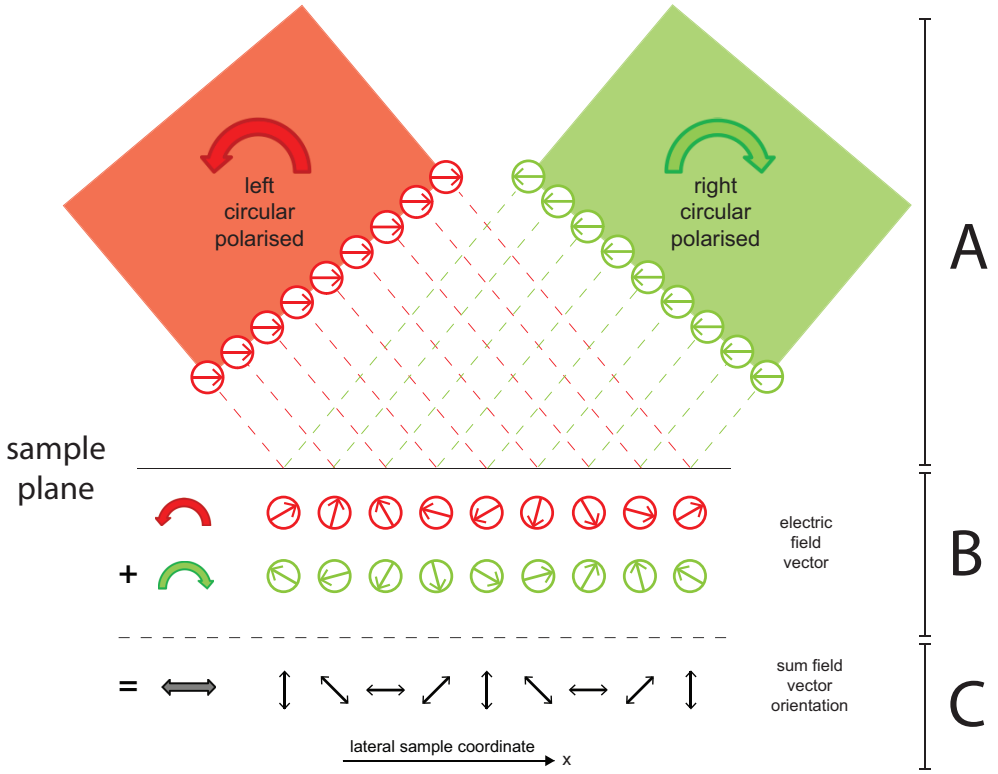

Fig. 3.9: The picoSIM electric field vector distribution in the sample: The circularly polarised -1^{st} and $+1^{st}$ diffraction orders are projected via the objective lens and impinge on the sample under a certain angle of incidence (A). Consequently, different points of the same wave-front reach the sample temporally delayed yielding a distribution of electric field vectors in the sample whose phases depend on their lateral position (B). In picoSIM one of the diffraction orders is left-circularly polarised (shown in red) whereas the other is right-circularly polarised (shown in green). The superposition of these two circularly polarised diffraction orders in the sample yields a distribution of sum field vectors whose orientations depend on their lateral position and thus the desired distribution of linear polarised light (C).

3.2.4 picoSIM - Filling the missing cone

In contrast to the previous explanations concerning picoSIM, the setup presented in 4.1 employs a coherent rather than an incoherent two-beam illumination. Consequently, the support of the final image will resemble the one presented in 3.1.2 for a two-beam hrSIM setup optimised for optical sectioning rather than the one presented in 3.1.1 for sSIM. Furthermore, for the reconstruction of the raw picoSIM images, not the sSIM (see 3.1.1) but the hrSIM reconstruction algorithm (see 3.1.2) was used, albeit just for one orientation of the grating. The reasons for this choice will be discussed in section 4.4.2.

4. MATERIALS AND EXPERIMENTAL METHODS

This chapter gives an overview of the optical and non-optical hardware being used to build the picoSIM setup and describes the reasons that led to the employment of the respective components (see 4.1). Furthermore, the samples and the respective sample preparation methods are described in section 4.2. Finally, sections 4.3 and 4.4 explain respectively the data acquisition process and the data processing for the picoSIM data presented in 5.2.

The constituent steps of the setup alignment process are described in appendix B.

4.1 picoSIM setup

The picoSIM setup and all its components described in this section are depicted in Fig. 4.1. A list of setup parameters can be found in appendix E.

To conduct the experiments an off-the-shelf inverted wide-field microscope (Zeiss Axiovert 200 M, Carl Zeiss AG, Germany) was modified to meet the requirements of picoSIM. Specifically, the reflector turret, the objective nosepiece, the sample stage and the components of the emission path are used as a basic module; however, the components of the original illumination path up to the filter cube were removed entirely and replaced by the optics described below. On the emission side of the system, the original Zeiss tube lens is used. The camera mount at the sideport is used to mount the four-way image splitter, which is an essential part of the picoSIM setup.

The picoSIM setup described in this thesis allows the placement of the grating at two different positions in the illumination path (before L_3 and before L_5 respectively). This allows the generation of illumination patterns with two different periodicities in the sample. Moreover, the setup is designed for coherent illumination. Due to the

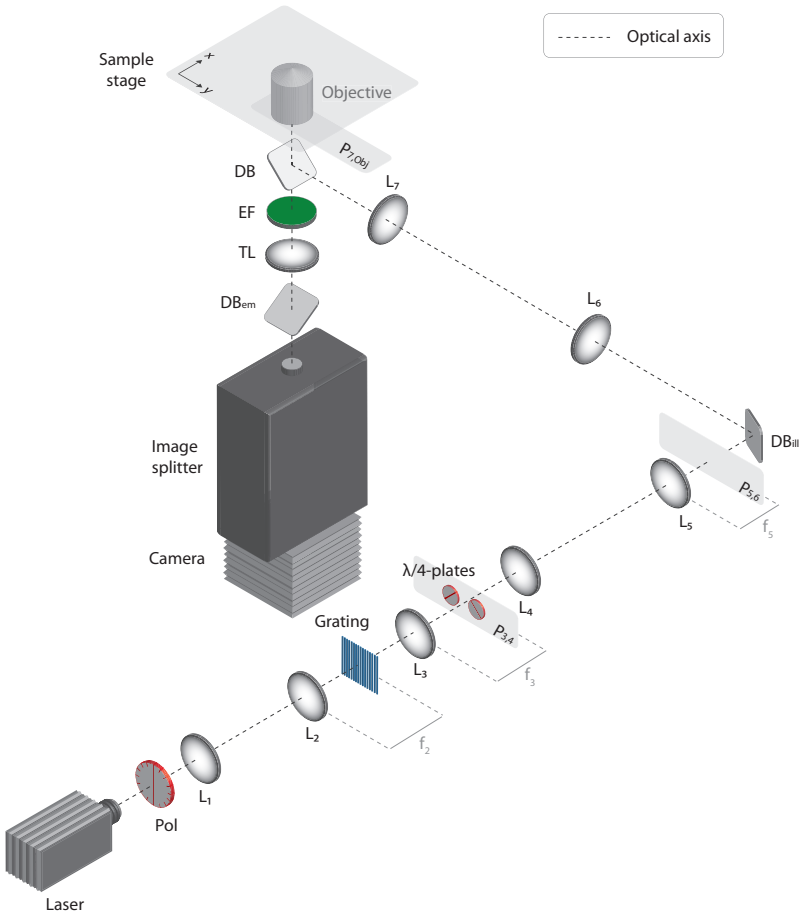

Fig. 4.1: The picoSIM setup with the grating positioned in the Fourier plane before L_3: All lenses are in telecentric arrangement. After being linearly polarised by the polarisation filter Pol, the light is relayed via the lenses L_1 and L_2 (focal length f_2) to illuminate the diffraction grating. The two $\lambda/4$-plates are positioned in the Fourier plane $P_{3,4}$ behind L_3 (focal length f_3) to left- (right-) circularly polarise the -1^{st} ($+1^{st}$) diffraction order. Moreover, at this position the 0^{th} order and all higher orders are mechanically blocked. The lenses L_4, L_5, L_6 and L_7 direct the circularly polarised orders into the back focal plane of the objective $P_{7,Obj}$. On its way to the objective the illumination light is reflected by the dichromatic beamsplitters DB_{ill} and DB. Alternatively (not depicted), the grating can be positioned in the Fourier plane before L_5 (focal length f_5). In this case, the $\lambda/4$-plates must be placed in plane $P_{5,6}$. In this configuration of the setup, the grating imaged into the sample has a smaller periodicity d_s ($d_s = 308nm$ instead of $d_s = 1.23\,\mu m$).
On the detection side of the system, the light passes the dichromatic beamsplitter DB, which separates the emission light from the illumination light, the emission filter EF, the tube lens TL and another dichromatic beamsplitter DB_{em} before it enters the four-way image splitter to which the camera is mounted. DB_{ill} and DB_{em} are integrated in the setup to compensate for depolarisation effects caused by DB.

design constraints described below this seemed to be the most feasible approach to start with.

4.1.1 Objective

The objective used to conduct the experiments presented in this thesis is an oil immersion objective (Plan-Apochromat 100×/1.4 Oil DIC, ∞/0.17, Carl Zeiss AG, Germany) with a magnification of $M = 100$ and a numerical aperture of $NA = 1.4$. The diameter D of the back aperture, also referred to as pupil diameter, can be calculated using $D = 2f_{obj}NA$ [42]. The effective focal length f_{obj} of the objective lens can be derived from its magnification M which results from $M = f_{tl}/f_{obj}$. This equation clarifies that any objective is designed to be used along with the corresponding detection tube lens of focal length f_{tl}. When using the incorrect objective/tube lens combination the magnification of the optical system will deviate from the value indicated on the objective. Moreover, the aberration-correction, for which modern Zeiss objectives are designed, will only yield the best performance if the objective fits to the tube lens in use.

The nominal focal length of the detection tube lens in the Zeiss Axiovert 200 M microscope stand is $f_{tl} = 164.5\,mm$. Hence, the effective focal length of the objective in use calculates to $f_{obj} = 1.645\,mm$. This yields a pupil diameter of $D = 4.61\,mm$. The size of the back aperture can be used to find the grating period in the sample leading to the best optical sectioning performance (see paragraph Lenses).

4.1.2 Objective lens nano-positioner

In order to acquire images of different z-positions in the sample it is necessary to change the focus position. This can be accomplished in various ways, of which the most common are to move the sample stage of the microscope or to move the objective. In the Axiovert 200 M the re-focusing is carried out by moving the objective along the optical axis.

When acquiring a stack of images of different focus positions, fast and accurate repositioning of the objective is essential. For this reason a piezo-driven nano-focusing

device (P-725.2CD, Physik Instrumente, Germany) along with the requisite controller (Physik Instrumente, Germany) was included in the system. The nano-positioner has a travel range of 250 μm, a closed loop resolution of 0.75 nm, a closed loop linearity of 0.03% and a repeatability of $\pm 5\, nm$ as specified by the supplier.

Due to the dimensions of the nano-positioner the objective moves closer to the sample stage. To avoid a reduced focus range, custom-made spacers (IPHT Jena workshop, Germany) are placed beneath the sample stage to raise it.

4.1.3 Light source

For the alignment of the picoSIM setup as well as for the coherent illumination in the experiments presented in 5.1, a laser (Unknown company) with a wavelength of $\lambda = 473\, nm$, a beam diameter of approximately 2 mm and an output power of $130mW$ was used.

For the experiments discussed in 5.2 this light source was replaced by a laser (Lasever, China) with the same wavelength and beam diameter but with an output power of $600mW$.

4.1.4 Diffraction grating

The purpose of the diffraction grating is to generate the -1^{st} and $+1^{st}$ diffraction orders which are then directed onto the $\lambda/4$-plates.

There are also other ways to generate two beams that can then be polarised accordingly. However, using a grating is an easy way to ensure that the two beams are in phase. Furthermore, as the grating is imaged into the sample this arrangement also works for partially coherent or incoherent light.

The grating used in the picoSIM setup is a transmission grating with a grating period of $d = 12.5\, \mu m$ ($46 - 069$, Edmund Optics GmbH, Germany). Many commercial diffraction gratings distribute the major part of the incident power to the 0^{th} order. Due to the 0^{th} order block in the picoSIM setup, a major amount of illumination intensity would be lost in this case, not allowing the short exposure times needed for fast imaging.

The diffraction grating used distributes 25% of the incident beam power to the -1^{st}, 0^{th} and $+1^{st}$ order each. These specifications are given by the manufacturer when using a wavelength of 632 nm.

For the 473nm laser used in the picoSIM setup the power distribution was measured to be 22% in the -1^{st} order, 17% in the 0^{th} order and 25% in the $+1^{st}$ order.

4.1.5 $\lambda/4$-plates

The $\lambda/4$-plates can be positioned in plane $P_{3,4}$ or $P_{5,6}$ of the picoSIM setup to circularly polarise the -1^{st} and $+1^{st}$ diffraction orders. Moreover, at this position the 0^{th} order and all higher orders are mechanically blocked.

The wave plates (Meadowlark Optics Inc., USA) used in the picoSIM setup are true zero-order polymer retarders with a retardance accuracy of $\leq \lambda/350$, specified for light of 473 nm wavelength. They stem from the same batch, have a diameter of 0.50 $inch$, a clear aperture of 0.40 $inch$ and a thickness of 0.13 $inch$ as specified by the supplier. A custom-made holder was designed to mount them. The $\lambda/4$-wave plates convert linear polarised light into circular polarised light when the angle between the linear polarisation and the fast axis of the wave plate is 45°. In order to polarise the laser light linearly, a polarisation filter *Pol* (Comar Instruments, U.K.) is included in the setup. The wave plates are specified for a retardance change of less than 1% over ±10° incidence angle. With 0.23°, the incident angle on the wave plates in the picoSIM setup lies well within the tolerance threshold.

The distance between the -1^{st} and $+1^{st}$ diffraction orders cannot be chosen arbitrarily, as described in 4.1.6. That is to say, the distance cannot be chosen to be arbitrarily large in order to ensure a most convenient order separation. Because of this, the *diameter/clearaperture* ratio had to be considered when ordering the wave plates. The smaller the distance between the -1^{st} and $+1^{st}$ diffraction orders in $P_{3,4}$ and $P_{5,6}$ respectively, the smaller the *diameter/clearaperture* ratio has to be. If the ratio is too large, the diffraction orders will impinge on the rim of the wave plates that are positioned right next to each other, rather than on the clear aperture. The desire for

the ratio to be as small as possible led us to order the unmounted wave plates with a ratio of 1.25 rather than the mounted ones with a ratio of 1.43. Hence, it was necessary to design a mounting device.

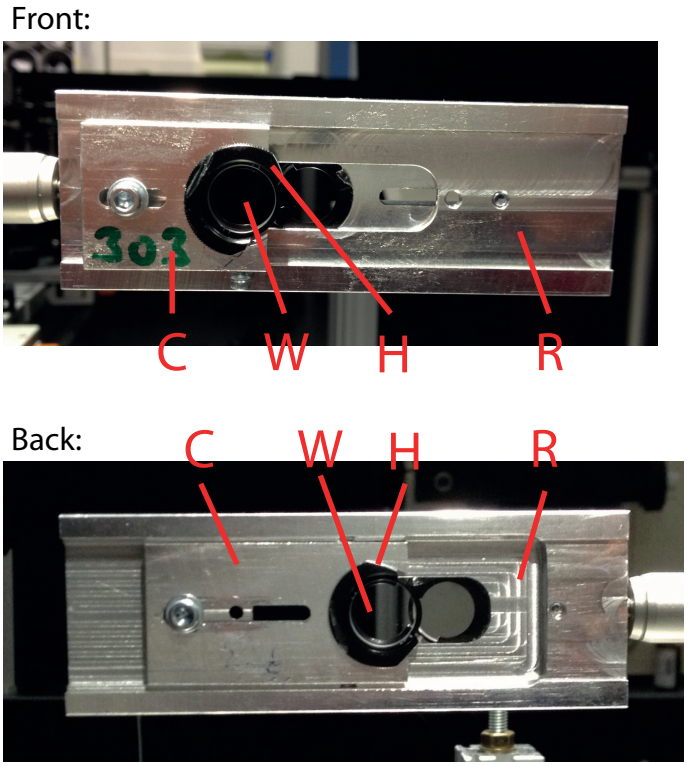

Fig. 4.2: The $\lambda/4$-plate mounting device: Shown are the front and the back of the $\lambda/4$-plate mounting device. On either side a $\lambda/4$-plate (W) is mounted using a commercial holder (H), amended to meet our requirements. Each holder is attached to a carrier (C), still allowing to rotate the wave plate holder manually for alignment reasons. Both carriers can be moved along the rail (R).

The custom-made mounting device (Fig. 4.2) consists of two parts: the wave plate holders and a guide rail system. The design of the wave plate holders (Micos GmbH, Germany) conforms with the design of a standard mirror or lens mount. The optics rests against a small shoulder and is fixed by means of a retaining ring. However, the shoulder against which the wave plate rests is minimised in such a way that the clear aperture is usable entirely. Each wave plate holder sits on a carrier that can be moved along a rail. The two carriers are attached to opposing sides of the rail. This makes it possible to bring the $\lambda/4$-plates to overlap, allowing for a smaller distance between

the -1^{st} and $+1^{st}$ diffraction orders. The engineering drawings for both the carriers and the guide rail system were provided by Robert Kretschmer (IPHT, Jena). The manufacturing was conducted in the workshop of the IPHT Jena.

4.1.6 Lenses

Except for the detection tube lens TL, which is an original Zeiss component, all lenses along with the mounting systems were purchased from Thorlabs (Thorlabs GmbH, Germany). Achromatic doublets with an anti-reflection coating optimised for a wavelength range of $400\,nm - 700\,nm$ and a diameter of $1\,inch$ were used exclusively. We decided on these lenses due to their property of reducing spherical aberrations. For higher precision in the lateral direction, translation mounts with a micrometer sensitivity were used to mount the lenses.

The lens combination for the illumination side of the setup had to be chosen very carefully. In fact, there are four constraints that had to be considered:

1. The design of the Axiovert 200 M microscope stand limits the possibilities in choosing an illumination tube lens L_7.

2. The distance between the diffraction orders in plane $P_{3,4}$ and $P_{5,6}$ must be sufficient to enable the separation of the individual orders.

3. The $\pm 1^{st}$ diffraction orders must impinge on the back aperture of the objective at the correct lateral position and with the correct distance between each other to allow for the reconstruction of an optically sectioned image.

4. The illumination light must not be cut by any of the lenses, i.e. each lens must accept the full cross-section of incoming light.

Since the original illumination path of the Axiovert 200 M was entirely removed, a new illumination tube lens had to be integrated. After an original Zeiss illumination tube lens with a focal length of 164.5 mm, the best choice would have been a lens with a focal length similar or smaller to that of the original lens. Unfortunately, the design of the microscope stand makes it difficult to integrate a non-Zeiss illumination tube lens with such a short focal length. Therefore, L_7 was chosen to have a focal length of $f_7 = 200\,mm$. This was the best possible compromise. In 4.1.1 the importance to use the correct objective/tube lens combination was pointed out. However, this comment refers mainly to the tube lens on the emission side, which understandably has a higher impact on the imaging process than the tube lens on the illumination side. Moreover, due to the laser illumination used in the setup, chromatic aberrations do not pose a problem. Hence, the deviation from the ideal focal length value on the illumination side is less severe.

The necessity for order separation, the dimensions of the $\lambda/4$-plates and the design of the custom made mounting device for the wave plates entail the need for a sufficient distance between the diffraction orders in plane $P_{3,4}$ and $P_{5,6}$ respectively.

As shown in Fig. 4.3, the distance y between the 0^{th} and the $+1^{st}$ order (which is the same as the distance between the 0^{th} and the -1^{st} order) in $P_{3,4}$ ($P_{5,6}$) is proportional to the focal length f_3 (f_5) of lens L_3 (L_5), positioned at distance f_3 (f_5) behind the grating: $y = f_3 tan\varphi$ ($y = f_5 tan\varphi$), with φ being the angle between the optical axis and the central ray of the $+1^{st}$ diffraction order before it impinges on L_3 (L_5). The longer the focal length f_3 (f_5), the larger the distance between the diffraction orders in plane $P_{3,4}$ ($P_{5,6}$). A large distance obviously simplifies the order separation. However, it might have a negative influence on the fulfilment of the fourth constraint mentioned above; the larger the distance between the diffraction orders in plane $P_{3,4}$ ($P_{5,6}$), the more likely the light is cut by one of the following lenses. Experiments showed that a focal length of $f_3 = 50\,mm$ ($f_5 = 50\,mm$) for L_3 (L_5), which corresponds to a value for y of 1.9 mm in the final picoSIM setup, is a good choice.

Since coherent two-beam illumination is used, theory suggests to project the -1^{st}

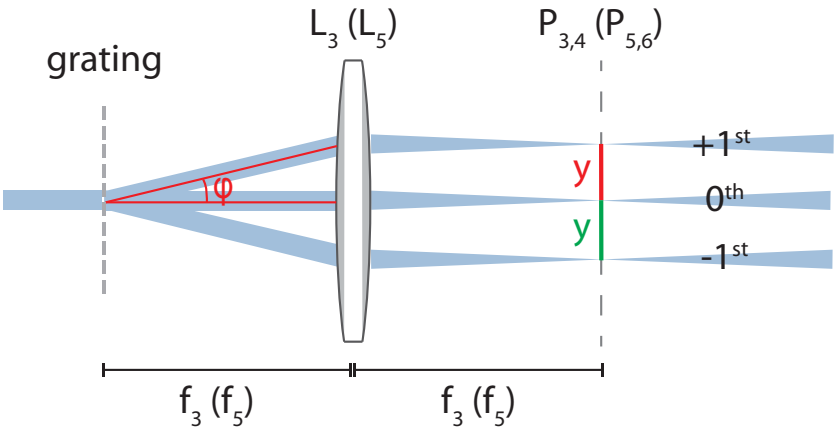

Fig. 4.3: Lens considerations: The distance y between the diffraction orders (-1^{st}, 0^{th} and $+1^{st}$) in plane $P_{3,4}$ ($P_{5,6}$) depends linearly on the focal length f_3 (f_5): $y = f_3 tan\varphi$ ($y = f_5 tan\varphi$), where φ denotes the angle between the optical axis and the central ray of the $+1^{st}$ diffraction order. A sufficient size of y is crucial to allow the separation of the individual orders beyond L_3 (L_5).

and $+1^{st}$ diffraction orders in such a way that $\vec{k}_{illu} = 0.5\ \vec{k}_{max}$. This will lead to the best sectioning performance in theory, as the higher order object components will be positioned at $-0.5\ k_{max}$ and $+0.5\ k_{max}$ in Fourier space respectively (see Fig. 3.7c). Accordingly, the aim is to project a grating with a period length of approximately $d_s = 360\,nm$ into the sample.

Positioning the grating in the Fourier plane between L_4 and L_5 (with $f_6 = 300\,mm$ and $f_7 = 200\,mm$) yields a value for d_s of $308\,nm$ which is finer than the optimum.

The illumination side of the setup was designed with two additional lenses guaranteeing an alternative image plane between L_2 and L_3. Placing the grating at this position (with $f_4 = 200\,mm$) leads to a value for d_s of $1.23\,\mu m$. Projecting such a relatively coarse grating into the sample will not only improve the signal-to-noise (due to the shape of the component specific 2D OTF shown in Fig. 4.8b) but also reduce the axial component in the illumination light's field vector, leading to the residual grating discussed in 5.1.1, albeit at the expense of a reduced sectioning performance.

Various lens combinations satisfy the constraints mentioned so far. Nevertheless, the need for short exposure times requires that as much light intensity as possible reaches the sample. For that reason only lens combinations that relay the entire cross-section

of illumination light can be used.

In this context it is important to consider the field of view and thereby the size of the laser beam that illuminates the grating. Since the grating is positioned in an image plane, the region of the grating illuminated corresponds to an illuminated region in the sample. The size of the illuminated sample region should correspond to the field of view. Otherwise, light intensity will be lost by illuminating regions in the sample that are not imaged. Due to the four-way image splitter, the field of view, which is actually the size of the camera sensor divided by the magnification in the emission path, calculates to a region of $44.4\,\mu m \times 33.5\,\mu m$ when using the CCD camera described in 4.1.9. The magnification on the illumination side can be used to calculate the corresponding size of the grating region that must be illuminated. The lenses L_1 and L_2 of the inverted beam expander have to be chosen carefully to adjust the laser beam diameter. According to these assumptions the beam diameter of the laser that is incident on the grating positioned before L_3 must be $0.23\,mm$. The actual diameter used in the picoSIM setup is approximately $0.4\,mm$. It was chosen to be larger than necessary since the light intensity in the border area of the illuminated sample region tends to decrease. A larger field of view ensures that the actual sample region imaged is illuminated evenly.

The chosen lens combination meets all targets. In particular, seven lenses with the following focal lengths are positioned in the illumination path: $f_1 = 150\,mm$, $f_2 = 30\,mm$, $f_3 = 50\,mm$, $f_4 = 200\,mm$, $f_5 = 50\,mm$, $f_6 = 300\,mm$, $f_7 = 200\,mm$.

4.1.7 Filters

The filter cube in the microscope stand contains a dichromatic beam splitter DB (XF2010 505DRLP, Omega Optical Inc., USA) and an emission filter EF (XF3084 535AF45, Omega Optical Inc., USA).

The dichromatic beam splitter DB is polarisation sensitive. Having a different effect on the s- and p-state, it both disturbs the circular polarisation of the -1^{st} and $+1^{st}$ diffraction orders in the illumination path and the polarisation distribution emitted by

the sample in the emission path.

To correct for this, an additional dichromatic beamsplitter (DB_{ill} and DB_{em} respectively) with identical specifications as the one in the filter cube is positioned both in the illumination path and the emission path. As suggested in [43], to correct the negative effect of the beamsplitter in the filter cube, the orientation of the extra beam splitters has to be such that incident light that is s-polarised for one of the beamsplitters is p-polarised for the other, and vice versa. The ideal case would be to position the additional beamsplitters in a $4f$ distance from DB. Although this is done for DB_{ill} on the illumination side, the design of the image splitter complicates the realisation on the emission side. However, the small angles allow the placement of DB_{em} in the Fourier plane relative to DB to yield a positive effect.

4.1.8 Four-way image splitter

The four-way image splitter and all its components described in this paragraph are depicted in Fig. 4.4.

The image splitter (Rainer Pick, Max-Planck-Institut für biophysikalische Chemie, Göttingen, Germany) divides the emission light into four identical beams. Although only a minimum of three images are required for the SIM reconstruction algorithm, using a four-way image splitter, and thus four images for the reconstruction, is advantageous as no emission light is unnecessarily discarded. In contrast, even with perfect optics the design of a three-way image splitter entails a 50% loss of emission light.

The image splitter was delivered without optical components. All the components described below were ordered separately. They were chosen carefully to fit the special needs of the picoSIM setup. Some of them had to be amended by an optical workshop to meet the requirements of the image splitter.

Before going into detail, the basic points, important to understand the principle of how the image splitter works are listed:

1. The incoming emission light is divided into two identical beams by means of a non-polarising beam splitter BS.

2. Each of the two beams is directed onto a polarising beam splitter (PBS_1 and PBS_2 respectively) via a lens (L_{1a} and L_{2a} respectively).

3. In each case, the polarising beam splitter splits the light in two components, each with a different angle of linear polarisation.

4. Each of the four resulting beams is directed onto a different region of the same camera chip via another lens (L_{1b}, L_{1c}, L_{2b} and L_{2c} respectively) to re-image the intermediate image created at RA.

After passing the intermediate image plane at the rectangular aperture RA, the emission light reaches the non-polarising beam splitter BS (AHF Analysetechnik AG, Germany) to be divided into two identical beams. The beam splitter was chosen to come as close as possible to a $50:50$ splitting ratio that is independent of the polarisation of the incident light. The non-polarising beam splitter BS is designed for a wavelength range of $510\,nm$ to $570\,nm$, has a surface figure of $\lambda/10$ and a substrate thickness of $6\,mm$.

Beyond the beam splitter BS, each of the two beams passes the first lens (L_{1a} and L_{2a} respectively). The achromatic doublet lenses (OptoSigma, USA) are coated with a broadband anti-reflection coating and have a focal length of $f = 150\,mm$.

Various metallic mirrors with silver coating (M_{1a}, M_{2a} and M_{2b}; Thorlabs GmbH, Germany) reflect the beams onto the polarising beam splitters PBS_1 and PBS_2. Mirrors have the property of adding a phase on the light reflected. The phase added depends both on the polarisation of the incident light and the angle of incidence (AOI). Metallic mirrors ensure a far better performance than dielectric mirrors when dealing

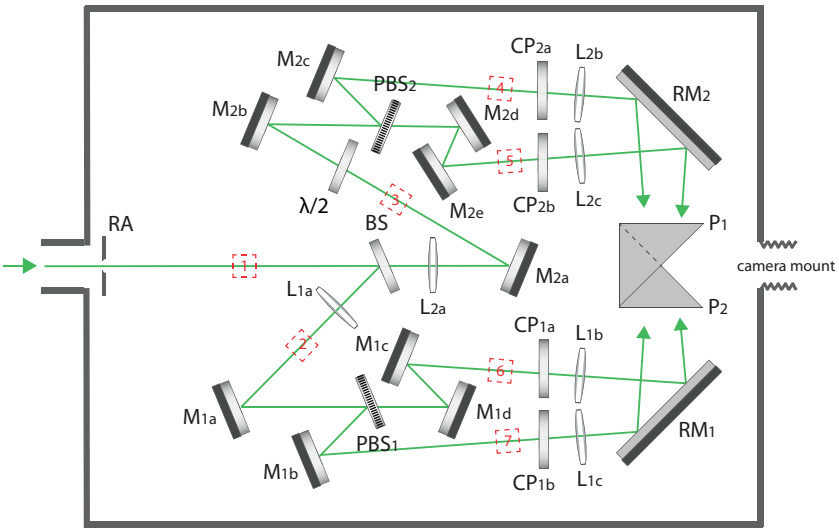

Fig. 4.4: The four-way image splitter: The fluorescence emission light (light path depicted in green) enters the image splitter via the rectangular aperture RA, coinciding with the intermediate image plane. The non-polarising beam splitter BS divides the light into two identical beams. Each of these beams is then directed onto a polarising beam splitter (PBS_1 and PBS_2 respectively) via a first lens (L_{1a} and L_{2a} respectively) and the mirrors M_{1a}, M_{2a} and M_{2b} respectively. The beam directed onto PBS_2 first passes a $\lambda/2$-plate that rotates the polarisation direction of the light by 45°. The polarising beam splitters divide the light into four beams with relative polarisation angles of 0°, 45°, 90° and 135°. Each of the four beams is then imaged onto the camera (not depicted in this figure) via a series of mirrors (M_{1b}, M_{1c}, M_{1d}, M_{2c}, M_{2d} and M_{2e} respectively), a clean-up polariser (CP_{1a}, CP_{1b}, CP_{2a} and CP_{2b} respectively), a second lens (L_{1b}, L_{1c}, L_{2b} and L_{2c} respectively), a rectangular mirror (RM_1 and RM_2 respectively) and a 90° prism mirror (P_1 and P_2 respectively). P_1 and P_2 are positioned on top of each other. The position of the alignment pinholes AP_1 to AP_7, that are integrated in the setup only during alignment (see appendix B.2), is indicated by the dashed red squares.

with polarised light. The silver mirrors were chosen because they offer the highest reflectivity in the visible spectrum of any metallic mirror.

The polarising beam splitters PBS_1 and PBS_2 (Moxtek Inc., USA) utilise the wire-grid technology. Their orientation is chosen to maximise their efficiency. Consequently, both beam splitters are oriented identically. However, before the light reaches PBS_2 it passes a $\lambda/2$-plate that is oriented in such a way that it rotates the polarisation of the incoming light by 45°. This arrangement allows for dividing the emission light in four beams with four different angles of linear polarisation. PBS_1 transmits the 0° component and reflects the 90° component. The second polarising beam splitter PBS_2

transmits the 45° component and and reflects the 135° component.

After the separation of the different polarisation components another series of metallic silver mirrors (M_{1b}, M_{1c}, M_{1d}, M_{2c}, M_{2d} and M_{2e} respectively; Thorlabs GmbH, Germany) direct each of the four beams to a second lens (L_{1b}, L_{1c}, L_{2b} and L_{2c} respectively; OptoSigma, USA). The specifications for the second lenses in the beam path are identical to the ones mentioned above for the first lenses. The image splitter is designed in accordance with the principle of infinity optics which allows for a non $4f$ design, with f being the focal length of the lenses in use. However, the image generated at the first image plane RA is not magnified by the system.

The second lenses direct the beams via clean-up polarisers (CP_{1a}, CP_{1b}, CP_{2a} and CP_{2b} respectively; Comar Instruments, U.K.) onto the rectangular silver mirrors (RM_1 and RM_2 respectively; Linos GmbH, Germany) from where they are reflected onto the 90° prism mirrors (P_1 and P_2 respectively, OptoSigma, USA) and eventually onto the camera.

4.1.9 Camera

For acquiring the data presented in 5.1 and 5.2.1 a CCD camera (Imager Intense, La Vision, Germany) with a sensor size of $1376px \times 1040px$ and a pixel pitch of $6.45\,\mu m \times 6.45\,\mu m$ was used. The frame rate as specified by the supplier is $10Hz$ with a gain dependent readout noise of 4 to 6 electrons. The camera is equipped with a $12bit$ analogue-to-digital converter.

The data presented in 5.2.2 was acquired utilising an sCMOS camera (ORCA-Flash 4.0, Hamamatsu, Japan) with a sensor size of $2048px \times 2048px$ and a pixel pitch of $6.45\,\mu m \times 6.45\,\mu m$. The frame rate as specified by the supplier is $100Hz$ with a readout noise of 1.3 electrons. The camera is equipped with a $16bit$ analogue-to-digital converter.

The reason for using two different cameras is that the sCMOS camera was not available for all experiments.

When choosing a camera it is important to consider the adequacy of the sensor

pixel pitch. The pixel pitch corresponds to the sampling distance D_s in image space. The intensity distribution in image space can be considered to be a continuous function being composed of various sine waves, each with a different frequency, amplitude and phase [44]. Only if the sampling distance D_s is chosen correctly can the measurement of the intensity distribution be accurate. Choosing a sampling distance too coarse will result in aliasing, i.e. measuring sine waves that do not actually exist in the signal.

According to the Nyquist criteria aliasing can be avoided if the sampling frequency k_s exceeds the highest image frequency k_{max} by a factor of 2. In this case all frequency aliases lie beyond the transmittable frequency limit k_{max} and thus will not be imaged [44]:

$$k_s = 2k_{max} = 2\pi\frac{4NA}{\lambda_{em}} \,. \tag{4.1}$$

With a value of $510\,nm$ for λ_{em} and a magnification of $M = 100$, this yields a sampling distance in image space of $D_s = 9.1\,\mu m$. Hence, with a pixel pitch of $6.45\,\mu m \times 6.45\,\mu m$ the sampling is denser than required by a factor of 1.4. Although this is not a major drawback, choosing a camera with a larger pixel pitch can increase the dynamic range, the sensitivity and the signal-to-noise ratio.

4.2 Samples and sample preparation

The sample preparation had to be carried out carefully since the image quality in microscopy depends not only on the optical components of the illumination and detection side of the optical system respectively, but also on the properties of the sample itself. The sample, as the region from which the emission light emerges, is part of the detection side and therefore contributes to the performance of the microscope.

In general, a microscope sample consists of a slide and a cover slip. The mounting medium, in which the actual specimen is embedded, lies in between these two components. The immersion medium between the objective and the cover slip is another

important element of the imaging beam path and must be chosen correctly to avoid aberrations.

Microscope objectives are designed assuming certain conditions in the sample. A decrease in image quality can result if these conditions are not met.

Different microscope samples were used depending on the aim of the experiment. Describing the microscope samples and the protocol of their preparation is the concern of this section. Whenever possible, the sample preparation was optimised to meet the requirements of the oil immersion objective described in 4.1.1. The cover slips used were high performance cover slips (Zeiss, Germany) with a thickness of $170 \pm 5\,\mu m$. The immersion oil (Zeiss, Germany) has a refractive index of 1.5180 at $23°C$ for light with a wavelength of $546.1\,nm$.

4.2.1 Fluorescent bead sample

The parameters necessary to align the four raw picoSIM images imaged onto different regions of the same camera chip (see 4.4.1), were identified using a fluorescent bead sample provided from Zeiss. To prepare the sample, the $200\,nm$ polymer beads (Invitrogen) were first diluted in water, and the resulting solution applied to the surface of a cover slip. To ensure that the fluid disperses well, the cover slip was previously cleaned and plasma processed. Afterwards, a $24h$ drying period was ensured to allow for the attachment of the beads to the glass surface. The last step was to glue the cover slip onto the microscope slide using silicon rubber, which also acts as embedding medium.

4.2.2 Fluorescent plane sample

To characterise the sectioning performance of the system (see 5.2.1) a sample consisting of a thin, slowly bleaching and uniformly fluorescing layer (G. J. Brakenhoff, The Netherlands) was used. The thickness of the fluorescent layer is $115\,nm$. The fluorescent plane sample was initially developed for image calibration in fluorescence microscopy [45]. It contains the fluorescent dye Fluorescein embedded in a uniform polymer film.

4.2.3 Fixed biological samples

The preparation of the fixed isolated rat tibialis anterior myofibrils samples was carried out by Elisabeth Ehler (King's College London, UK).

For the biological samples underlying the data presented in 5.1.3 and 5.2.2, the musculus tibialis anterior was dissected from an adult rat, stored in solution (10 mM MES, 150 mM $NaCl$, 2 mM EGTA, 5 mM $MgCl_2$, 4.4 g glucose/litre; pH 6.1) on ice and teased into small muscle strips that were then tied in a slightly extended fashion onto little plastic plates. These were incubated over night at 4° in a 1:1 mix of 100% glycerol and 13.3 mM KH_2PO_4 pH 7.0. Afterwards, the plastic plates were transferred into a fresh glycerol KH_2PO_4 solution and then stored at -20°C. To prepare a sample for microscopy, the muscle pieces were pulled into smaller pieces with tweezers and incubated in rigor buffer (0.1 M KCl, 2 mM $MgCl_2$, 1 mM EGTA, 0.5 mM Dithiothreitol, 10 mM KH_2PO_4, pH 7.0) for an hour. They were then homogenised using a hand-held blender and spun onto poly-L-lysine coated slides (Thermo Scientific) using a cytospin (Shandon). They were immediately fixed using 4% PFA/PBS for 10 minutes. After a brief wash in PBS they were incubated with monoclonal mouse antibodies against titin (Z-disc epitope, clone T12, diluted 1:10) [46] in antibody dilution buffer (1% BSA, 20 mM Tris-base, 155 mM $NaCl$, 2 mM EGTA, and 2 mM $MgCl_2$, pH 7.5) for an hour at room temperature in a humid chamber. After several washes in PBS, the cells were incubated in the secondary antibodies for one hour at room temperature. As secondary antibodies we used Cy2-conjugated (Jackson Immunochemicals, UK) and DyLight488-conjugated (Jackson Immunochemicals, UK) goat anti-mouse immunoglobulins respectively (diluted 1:100). After washing the cells five times with PBS they were mounted in 0.1 M Tris-HCl/glycerol (3:7) and 50 mg/ml N-propyl-gallate at pH 9.5 or alternatively in gelvatol containing N-propyl-gallate [47].

4.3 Data acquisition

This section explains the data acquisition for the picoSIM data presented in 5.2. The individual steps of the data acquisition for the proof of concept studies are explained in 5.1.

Due to the four-way image splitter (see 4.1.8), one picoSIM image consists of four images of the same sample region, each with a different phase position of the effective illumination pattern and each imaged onto a different region of the camera sensor. The relative phases in the individual images are approximately 0°, 90°, 180° and 270° degrees. The raw data necessary to reconstruct an optically sectioned slice of the sample can hence be acquired in a single exposure.

For the z-stack, out of which the sectioning curve (see 5.2.1) was calculated, 60 (grating before L_5) and 40 (grating before L_3) picoSIM images were acquired, each at a different focus position of the fluorescent plane sample (see 4.2.2). Between the individual images, the objective-lens nano-positioner was moved in equidistant steps of $100\,nm$ (grating before L_5) and $300\,nm$ (grating before L_3).

Furthermore, for each experiment a series of 10 dark images was acquired, with the same exposure time as used in the actual experiment but without illuminating the sample.

Both the camera, i.e. the image acquisition, and the objective-lens nano-positioner were controlled via the open-source software μManager [48]. The acquisition of the z-stack was automated using a self written Beanshell [49] script in μManager's scripting console which is listed in appendix C.1.

4.4 Data processing

This section explains the data processing for the picoSIM data presented in 5.2. The data processing for the proof of concept studies is explained in 5.1.

For all data processing the programming environment Matlab (MathWorks, USA) and the image processing toolbox DIPimage [50] were used.

After acquiring a picoSIM image the four raw images need to be extracted and aligned into one coordinate system. The transformation matrices for this alignment were found in the course of the data registration process, which is described in the first part of this section (see 4.4.1) and for which the Flexible Algorithms for Image Registration (FAIR) toolbox [51], developed by Jan Modersitzki, Lars Ruthotto (both from the University of Lübeck, Germany) and Fabian Gigengack (University of Münster, Germany), was used.

The second part of this section (see 4.4.2) explains the reconstruction of the optically sectioned image out of the four extracted and aligned raw images. This data reconstruction was performed using a hrSIM reconstruction algorithm (see appendix A.3) written by Kai Wicker, Ondřej Mandula and Rainer Heintzmann at King's College London [27].

4.4.1 Data registration

The goal of the data registration process is to extract and align the four raw images in such a way that the sample in each of the four images lies at the same position in an overall coordinate system. In practice, three of the four extracted images need to be transformed into the coordinate system of the fourth image.

The three transformation matrices were found using an image of a 200 nm bead sample (see 4.2.1) as calibration slice. The calibration slice was acquired with the setup depicted in Fig. 4.1. However, the diffraction grating and the $\lambda/4$-plates were removed from the illumination side to avoid an incorrect alignment due to the effective illumination pattern being present in the four images.

After a background-correction (cf. paragraph "Data preprocessing" in 4.4.2) the four individual calibration images A, B, C and D were extracted from the calibration slice (Fig. 4.5). This is straightforward to do in Matlab. However, it is important to keep in mind that the three transformation matrices found by means of the calibration slice will later be applied to a true picoSIM image. This transformation will only succeed if the same ROI of the camera sensor are extracted from both the calibration

slice and the picoSIM image.

To calculate the affine transformation matrices, a multilevel parametric image registration approach was used [51]. The basic idea of the multilevel approach is to start the registration on a coarse level, where the images are smoothed by averaging over adjacent pixel values. Once accomplished on the coarse level, the result acts as a starting point for the registration on the next finer level. Due to the good starting approximation, only minor corrections are then needed on this level. Following [51], the multilevel approach necessitates fewer iterations for the optimisation and reduces the risk of being trapped in a local minimum due to diminishing fine details on the coarse level.

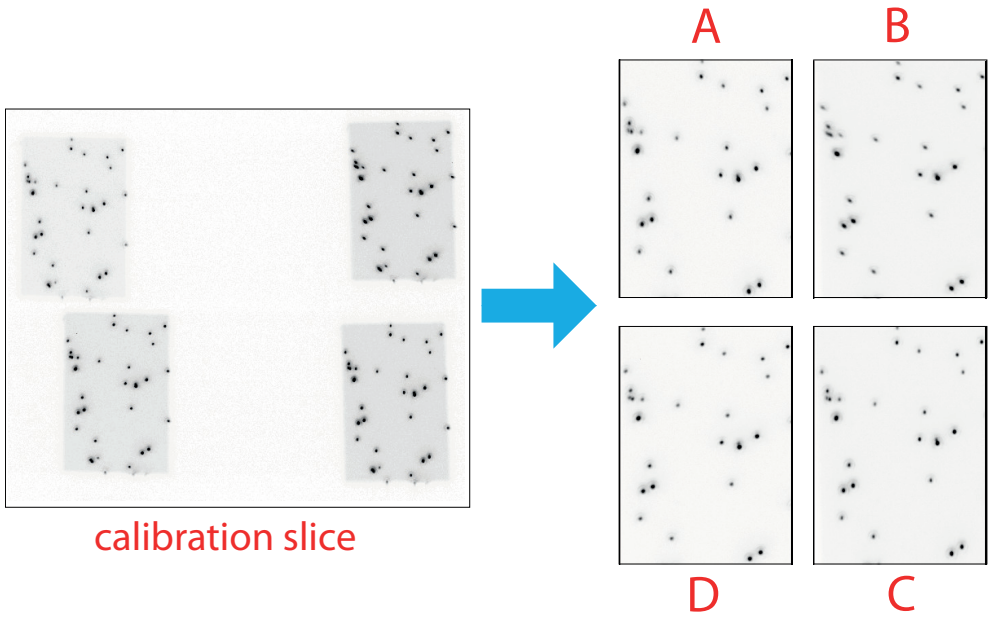

Fig. 4.5: Extracting the calibration images for the picoSIM data registration: The first step in finding the transformation matrices for the image registration in picoSIM is to extract the four calibration images A, B, C and D from the calibration slice, which is a background-corrected image of a 200 nm bead sample. For illustration purposes the colours of the images are inverted.

Applying the transformation matrices to the calibration images illustrates the effect of the image registration (Fig. 4.6). Applying the transformation matrices to the picoSIM data is prerequisite for a successful image reconstruction.

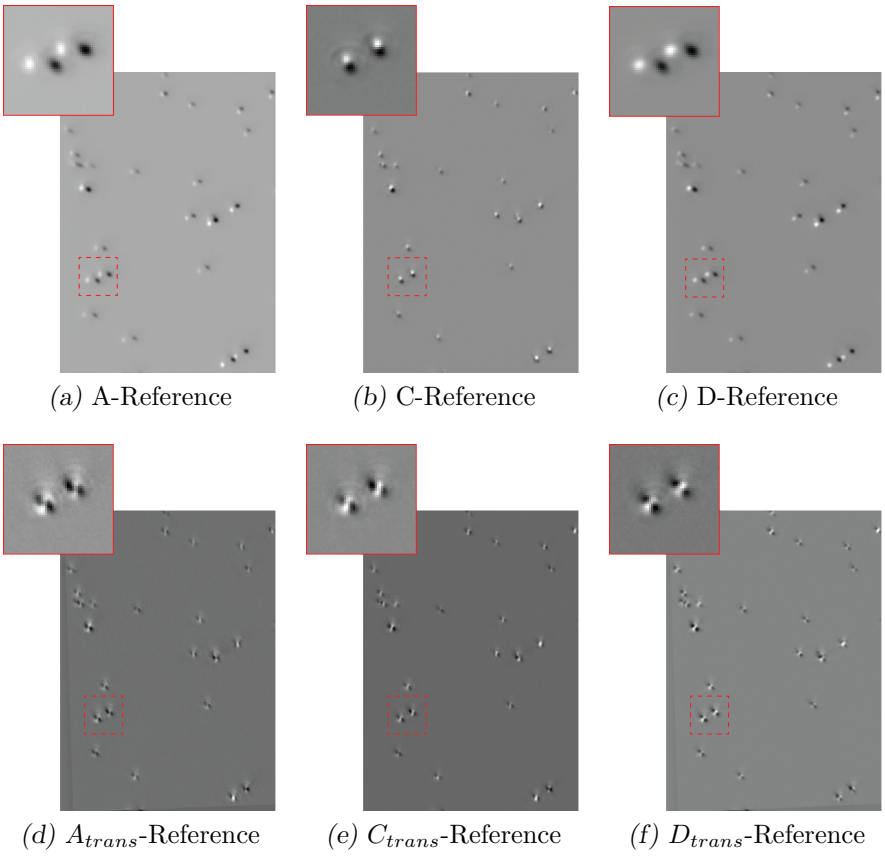

(a) A-Reference *(b)* C-Reference *(c)* D-Reference

(d) A_{trans}-Reference *(e)* C_{trans}-Reference *(f)* D_{trans}-Reference

Fig. 4.6: The effect of the picoSIM data registration: For a successful registration, three of the four previously extracted calibration images A, B, C and D need to be transformed into the coordinate system of the fourth image. Here, image B was chosen to be the reference image. The three transformation matrices, necessary to align the images A, C and D, were found utilising a multilevel parametric image registration. (a), (b) and (c) show the residual images, i.e. the difference between the calibration image in question and the reference image B, before the registration. The successful transformation is depicted in (d), (e) and (f), where the difference between the transformed calibration image A_{trans}, C_{trans} and D_{trans} and the reference image B is shown. The red-rimmed squares in the upper left corner of each sub-figure show a close up view of the image region marked with the dotted red square.

4.4.2 Data reconstruction

As already mentioned in 3.2.4, the picoSIM data reconstruction is performed employing the hrSIM reconstruction algorithm described in appendix A.3, albeit with some variations as explained below.

Considering two-beam illumination setups, the hrSIM algorithm is usually applied

to yield a lateral resolution improvement in thin samples. In order to achieve an isotropic effect in all in-plane directions, a hrSIM data set usually consists of at least three image sets per focal slice, each acquired with a different orientation of the illumination pattern. As we are solely interested in achieving optical sectioning, one picoSIM data set consists of just one image set per focal slice, acquired with one specific orientation of the effective illumination pattern. The reconstruction of an optically sectioned slice of a thick sample could also be achieved utilising the sSIM reconstruction algorithm presented in [3]. However, unlike the latter, the hrSIM algorithm is able to deal with phase values not according perfectly to theory [27]; moreover, it is less prone to artefacts compared to the sSIM algorithm. To meet our specific requirements, we amended the original version of the hrSIM algorithm to correct the varying pattern contrasts present in the raw picoSIM images (see below).

Several steps of the reconstruction process require the PSF of the system as an input parameter. The PSF used here was obtained from a simulation which is based on the vectorial high-NA theory [25, 26] and was written by Rainer Heintzmann and Peter Vermeer.

Data preprocessing

Before the actual reconstruction of the data some preprocessing was performed.

The first step was to subtract the background from the picoSIM data using a series of 10 dark images acquired, with the same exposure time as the actual picoSIM image but without illuminating the sample. The 10 dark images were averaged to one image which was then subtracted from the picoSIM image.

Afterwards, the four raw images were extracted and aligned using the transformation matrices calculated as described in the previous section. Possible brightness differences in the raw images, due to the image splitter components (see 4.1.8) not being perfectly aligned, were corrected by normalising the mean intensity of each raw image to the mean intensity of the first raw image.

As the reconstruction of the data is performed in Fourier space, the edges of the

raw images were dimmed by means of a Gaussian smoothing. This step was conducted to avoid artefacts in the fast Fourier transform (FFT) arising from sharp edges due to the periodic boundary condition of the FFT.

If more than one picoSIM image is acquired, e.g. when acquiring a z-stack of images, fluctuations in the illumination intensity and decreasing intensity due to photobleaching can cause brightness differences in the picoSIM images. To compensate for these effects, the background-correction was followed by normalising the mean intensity of each picoSIM image to one before proceeding with the steps described above.

Component separation

The first step of the component separation is to calculate the mixing matrix $\mathbf{M}$. Although the setup was designed to yield relative phases of 0°, 90°, 180° and 270° in the four raw images respectively, the exact phase values are retrieved retroactively from the acquired data to guarantee sufficient precision. Incorrect phase values would yield an imprecise separation of the individual components, leading to artefacts in the final image. The exact phase values of the experiment are calculated by means of an weighted auto-correlation of each of the Fourier-transformed raw images as explained in appendix A.4 [52].

This auto-correlation not only yields the entries of the mixing matrix $\mathbf{M}$ but also the relative contrast of the effective illumination pattern in each of the four raw input images. The original version of the algorithm assumes a constant contrast of the illumination pattern in all images. As the contrast of the effective illumination pattern in picoSIM may vary in the different raw images (see 5.1.2), the algorithm was adapted accordingly. The adapted algorithm corrects for the varying pattern contrast in the input images based on the amended mixing matrix $\mathbf{M}'$ (see appendix A.4), which not only contains the pattern phase but also the relative pattern contrast for each raw image.

The positive effect of this improvement can be shown by reconstructing a simulated set of raw images with varying pattern contrast. The image shown in Fig. 4.7b was

reconstructed using the original algorithm, grating artefacts are still visible. In contrast, in the image shown in Fig. 4.7c, reconstructed utilising the modified algorithm, the grating artefacts have been reduced.

Due to the four raw picoSIM input images, the mixing matrix is not square. Hence, its inverse $\mathbf{M}^{-1}$, needed to calculate the separated orders according to Eq. A.14, can be calculated as the Moore-Penrose pseudo inverse [53].

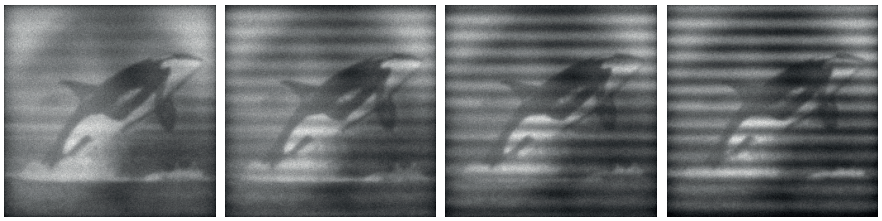

(a) Simulated raw images with 10%, 30%, 50% and 70% pattern contrast.

(b) SIM reconstruction (original version)

(c) SIM reconstruction (adapted version)

(d) Wide-field

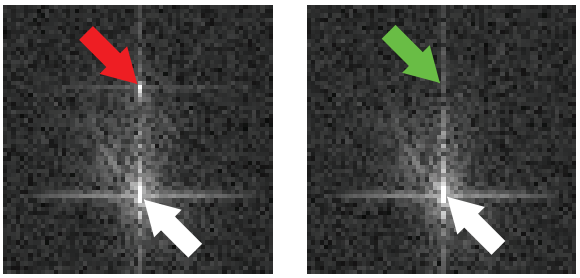

(e) Order separation (original version)

(f) Order separation (adapted version)

Fig. 4.7: Comparison between original and adapted version of the hrSIM algorithm: (a) shows a set of four simulated raw images with varying pattern contrast (10%, 30%, 50% and 70%). (b) and (c) show the results of the SIM reconstruction of this set of raw images employing the original version and the adapted version of the hrSIM reconstruction algorithm respectively. The corresponding wide-field image, calculated as the sum of the four raw images, is shown in (d). In either case, the algorithm removes the out-of-focus information. However, there are strong grating artefacts present in (b). The reason for this is the original algorithm not correcting for the varying pattern contrast in the raw images and thus not being able to separate the higher order components as can be seen in the Fourier image of the separated $+1^{st}$ order (e). The red arrow in (e) indicates information content stemming from the -1^{st} order mixing into the separated $+1^{st}$ (white arrow) order. (f) shows that the order separation performed by the adapted algorithm is improved. *Image of the orca adopted from DIPimage image library.*

Shift of components

The separated components must be shifted by $m\,\vec{k}_{illu}$ to their correct position in Fourier space. In order to find the precise subpixel shift vector $\vec{k}_{illu}$ we apply an iterative cross-correlation between the unshifted 0^{th} order component and a back-shifted higher order component in Fourier space, optimising the shift vector to maximise the peak in the origin of the cross-correlation image.

The actual shift of the separated components is done by multiplying the higher order components with a phase gradient $e^{-\imath\, m\, \vec{k}_{illu}\, \vec{r}}$ in real space.

Recombination of components and generalised Wiener filter deconvolution

Equation A.18 for the recombination of components is only directly applicable when performing a 3D reconstruction of a 3D data set.

For the experimental results presented in 5.1.3 and 5.2.2 only a 2D data set was reconstructed. The same is true for the z-stack discussed in 5.2.1 as the 3D data set was reconstructed in a slice-by-slice fashion.

Tailoring Eq. A.18 to be applicable for a 2D data set would yield:

$$\tilde{J}^{(z_0)}_{recomb}(\vec{k}_{xy}) = \frac{\sum\limits_{m=-1}^{+1} \tilde{h}^{*}_{m}(\vec{k}_{xy})\tilde{\Omega}^{(z_0)}_{m}(\vec{k}_{xy} + m\,\vec{k}_{illu})}{\gamma + \sum\limits_{m} |\tilde{h}_m|^2(\vec{k}_{xy})} \;,$$

with the projected 2D OTF:

$$\tilde{h}_m(\vec{k}_{xy}) = \int_{-\infty}^{+\infty} \tilde{h}_m(\vec{k})\, dk_z \;. \tag{4.2}$$

(As picoSIM deals with only one specific grating orientation we are omitting the grating orientation index o introduced in appendix A.3.)

However, this approach cannot be recommended, as sample information may be

needlessly disregarded [54]. Projecting the component specific 3D OTF $\tilde{h}_m(\vec{k})$ (Fig. 4.8a) along k_z yields a 2D OTF $\tilde{h}_m(\vec{k}_{xy})$ (Fig. 4.8b) with a central peak at $-m\,\vec{k}_{illu}$. Applying the modified version of Eq. A.18, and thus using $\tilde{h}_m(\vec{k}_{xy})$ as weight function, would lead to a strong contribution of an object component at the peak position of its 2D OTF. However, as becomes obvious when comparing Fig. 4.8a with Fig. 4.8b, the peak position is exactly where the component's 3D OTF suffers from the "missing cone". In contrast, other object components contain frequency information filling the "missing cone" at the frequency position in question. Consequently, suppressing a component at the peak position of its 2D OTF in favour of the other contributing components will lead to a better sectioning performance.

The 2D version of Eq. A.18 can be amended accordingly by introducing a Gaussian function [54]:

$$\tilde{g}_m(\vec{k}_{xy}) = 1 - a_m\, e^{-|\vec{k}_{xy}+m\vec{k}_{illu}|^2/2d_m^2}\ , \tag{4.3}$$

to modify the weights. The optimised function for component recombination reconstructing a 2D data set then becomes [54]:

$$\tilde{J}_{recomb}(\vec{k}_{xy}) = \frac{\sum_{m=-1}^{+1} \tilde{g}_m(\vec{k}_{xy})\,\tilde{h}_m^*(\vec{k}_{xy})\tilde{\Omega}_m^{(z_0)}(\vec{k}_{xy}+m\,\vec{k}_{illu})}{\gamma + \sum_m |\tilde{h}_m|^2(\vec{k}_{xy})\,\tilde{g}_m(\vec{k}_{xy})}\ . \tag{4.4}$$

The attenuation parameter a, the width parameter d as well as the Wiener parameter γ were found empirically. The shape of the component specific 2D OTFs under influence of the Gaussian function is depicted in Fig. 4.8c.

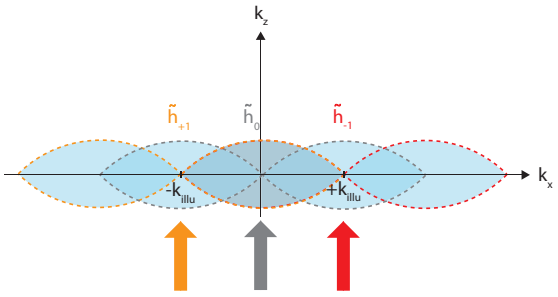

(a) Component specific OTFs $\tilde{h}_m(\vec{k})$ in 3D

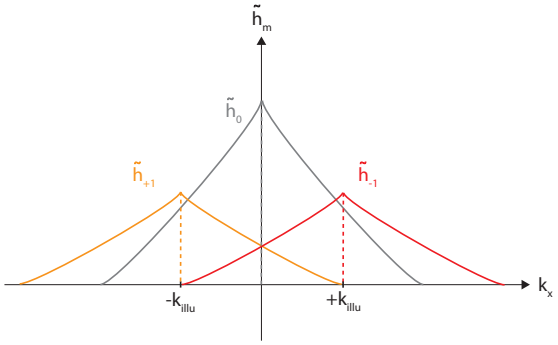

(b) Component specific OTFs $\tilde{h}_m(\vec{k}_{xy})$ in 2D

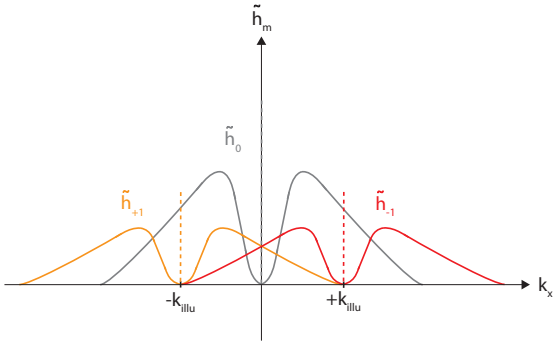

(c) Modified component specific OTFs $\tilde{h}_m(\vec{k}_{xy})$ in 2D

Fig. 4.8: Weighted averaging in 2D: (a) shows the component specific OTFs $\tilde{h}_m(\vec{k})$ in 3D. Projecting them along k_z yields their 2D equivalents as depicted in (b). Rewriting Eq. A.18 for the combination of components for a 2D data set would lead to a large contribution of a component at frequency positions where its weight function, i.e. its 2D OTF, has a high transfer strength. Comparing (a) with (b) reveals that the component in question cannot contribute any information filling the "missing cone" at these positions (indicated by the arrows). However, other components could do so. Amending the recombination formula by introducing a Gaussian function (see Eq. 4.4) corresponds to modifying the shape of the weight functions, i.e. the shape of the 2D OTFs as shown in (c), and thus leads to an improved sectioning performance. *Figure redrawn from [54].*

Apodisation

To avoid artefacts arising from the generalised Wiener filter deconvolution, the Fourier image is multiplied with the 2D version of the apodisation function introduced in appendix A.3: $\tilde{h}_{goal}(\vec{k}_{xy}) = d^{\kappa}(\vec{k}_{xy})$, with $d(\vec{k}_{xy})$ being the normalised Euclidian distance between the position $\vec{k}_{xy}$ and the support edge of the effective OTF. The parameter κ allows adjusting of the shape of the apodisation function. As explained in [27], for $\kappa = 1$ the distance function stays unchanged and retains its linear shape. Choosing a value of $\kappa < 1$ curves the distance function towards a convex shape, emphasising high frequencies, whereas a choice of $\kappa > 1$ yields a concave shape emphasising low frequencies. The value of κ was chosen to be one, yielding a linear shaped distance function $d(\vec{k}_{xy})$, similar to a conventional wide-field OTF.

Final image

An inverse FT yields the final 2D image in real space.

5. EXPERIMENTAL RESULTS AND DISCUSSION

Before the picoSIM data, for which the data acquisition and processing was described in sections 4.3 and 4.4, was acquired, the first step was a proof of concept study to show that it is possible to generate the desired polarisation distribution in the focal plane of the objective (Fig. 3.8) and to retroactively select the effective pattern position (see 5.1). For this, the image splitter in the picoSIM setup (Fig. 4.1) was replaced by a single polarisation analyser, i.e. the emission light was not split. With this variation of the original setup it can be shown that a picoSIM image resembles a conventional SIM image (see 5.1.1). To demonstrate that the phase position of the effective illumination pattern depends on the orientation of the analyser in the emission path, the analyser was rotated manually in multiple steps. After each step an image was acquired from which the pattern phase was then calculated (see 5.1.2). Finally, the three raw images necessary for the SIM reconstruction were acquired successively using a biological sample and reconstructed to obtain an optical sectioned image (see 5.1.3).

After the proof of concept study, the image splitter was mounted to acquire single-shot picoSIM images (see 5.2). To judge the sectioning performance of the setup, a z-stack of a fluorescent plane sample was acquired, from which a sectioning curve was then calculated (see 5.2.1). Finally, picoSIM was applied to fixed biological samples (see 5.2.2).

5.1 picoSIM in sequential mode: Proof of concept

Data acquisition For both the phase plot (Fig. 5.3) and the reconstruction of the biological sample data (Fig. 5.4) it was necessary to acquire images with different phase positions of the grating imaged onto the camera. The phase of the grating was

altered by manually rotating the polarisation analyser in the emission path.

For the fluorescent plane data underlying the phase plot, the analyser was rotated in steps of 10° through a total angle of 180°. At each step one image was acquired.

The three images necessary to perform the data reconstruction for the biological sample were acquired in sequence with relative orientations of the polarisation analyser of 0°, 60° and 120° leading to nominal phases of the effective pattern imaged onto the camera of 0°, 120° and 240°.

Data processing The first step in data processing was a background-correction (cf. paragraph "Data preprocessing" in 4.4.2). This step was carried out for all data presented in this section.

The images shown in Fig. 5.1 are corrected to have the same mean intensity.

Before the pattern phases were plotted (Fig. 5.3) the respective fluorescent plane images were additionally corrected for fluorescence intensity variations by normalising the mean intensity of each image to 1. This was done in order to compensate for fluctuations in the illumination intensity and decreasing intensity due to photobleaching. Moreover, the edges of the images were dimmed using a square shaped Hann window function with a flat central area. This step was conducted to avoid artefacts in the FFT arising from sharp edges due to the periodic boundary condition of the FFT. The phase of the grating was calculated in accordance with [55] from the first order peak in Fourier space. Beforehand, the value of the first order peak was divided by the value of the theoretical calculated intensity OTF at this position and half the value of the OTF-corrected zero order peak. Hence, Fig. 5.3 depicts not only the phases of the grating but also its OTF-corrected contrast, i.e. the contrast of the effective pattern in the sample rather than in the detected image, indicated by the distance of each data point from the origin.

The reconstruction of the biological sample data (Fig. 5.4) was performed in accordance with 4.4.2, albeit with some minor variations in preprocessing: only one dark image was used for the background-correction. Furthermore, as the images were ac-

quired successively, no image registration was necessary. However, a drift-correction was applied using the cross-correlation based DIPimage function "findshift". The wide-field image was calculated as the inverse FT of the separated 0^{th} order component, i.e. the unshifted wide-field component.

5.1.1 The picoSIM illumination pattern

Figure 5.1 shows the fluorescent plane data acquired with (Fig. 5.1a) and without (Fig. 5.1b) the polarisation analyser in the emission path. It can be seen that there is a weak grating existent even without the analyser being present in the setup.

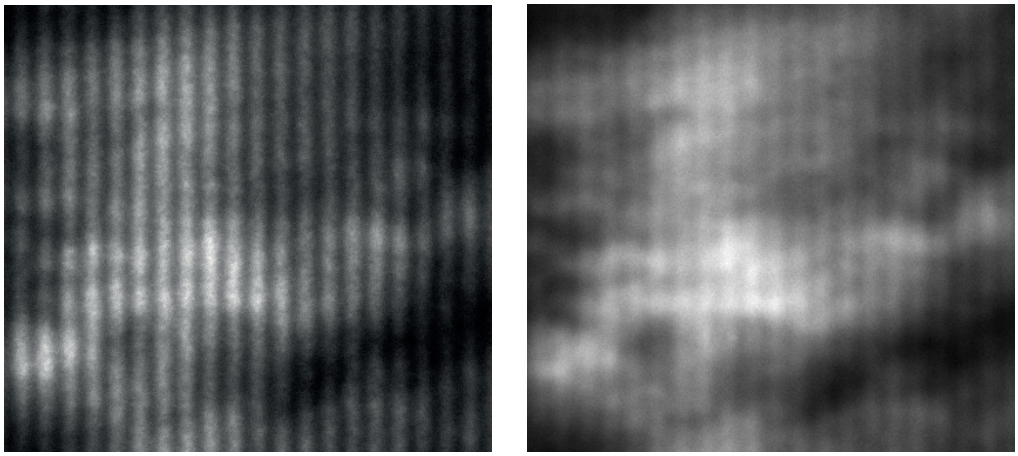

(a) With analyser *(b)* Without analyser

Fig. 5.1: The picoSIM illumination pattern: A fluorescent plane sample, illuminated with the picoSIM polarisation distribution (non-paraxial case), was imaged with (a) and without (b) a polarisation analyser positioned in the emission beam path. Camera: CCD, Laser: $130\,mW$, Grating constant in sample space: $d_s = 1.23\,\mu m$

A possible reason for this residual grating is the axial component of the illuminating polarisation distribution that was disregarded in [20]. In theory, only an illumination that satisfies the paraxial approximation yields a perfect picoSIM polarisation distribution (Fig. 3.8) without a residual grating. Due to the non-paraxial illumination (Fig. 3.9), the electric field vector, generated by either diffraction order in the sample, possesses an axial and an elliptical polarised in-plane component (Fig. 5.2A). While the superposition of the axial components of both diffraction orders leads to an intensity

distribution $I_z(x)$ (Fig. 5.2C), the superposition of their elliptical polarised in-plane components leads to the picoSIM polarisation distribution, albeit with an intensity $I_l(x)$ (Fig. 5.2C), depending on the lateral sample coordinate.

However, there are parts of the sample in which the axial components of the impinging diffraction orders will cancel out each other corresponding to a modulation contrast for $I_z(x)$ of one (Fig. 5.2C):

$$I_z(x) = \frac{a_1}{2}[1 + \cos(k_{illu}x - \varepsilon)] \,, \tag{5.1}$$

where a_1 is the peak-to-peak amplitude, ε a global phase and k_{illu} the illumination pattern's k-vector (in analogy to 3.2.2). The lateral sample coordinate x is defined in accordance with Fig. 3.8. The lateral intensity distribution $I_l(x)$ modulates in-phase with $I_z(x)$ (Fig. 5.2C):

$$I_l(x) = \frac{a_2}{2}[1 + m_l \cdot \cos(k_{illu}x - \varepsilon)] \,, \tag{5.2}$$

where m_l is the modulation contrast of $I_l(x)$.

An axial component present in the sample will lead to an excitation of fluorophores with a dipole-axis component along the optical axis. Due to the use of a high NA objective, light stemming from these fluorophores can be detected [56]. However, the shape of the 3D dipole radiation pattern suggests that the amount of light captured by the objective is reduced by a factor b compared to the light captured from fluorophores with only an in-plane dipole-axis. The residual intensity distribution $I_{NoA}(x)$, captured by the camera without the polarisation analyser in the emission path, can thus be described as:

$$I_{NoA}(x) = bI_z(x) + I_l(x) \,, \tag{5.3}$$

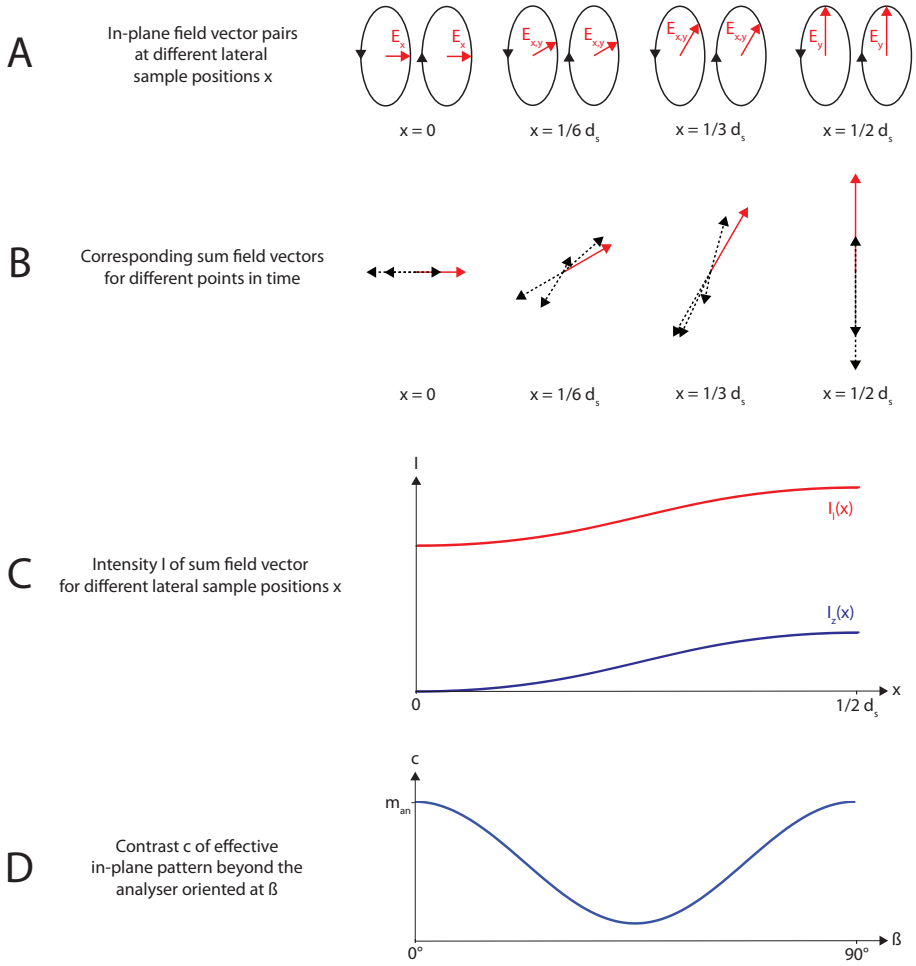

Fig. 5.2: The effect of a non-paraxial picoSIM illumination: Due to the angle of incidence of the diffraction orders on the sample, the projection of their electric field vectors along z yields an elliptical polarised in-plane component (A). The superposition of both orders leads to an in-plane sum field vector whose orientation and amplitude (corresponding to the intensity $I_l(x)$) depends on the lateral sample coordinate x (B,C). However, due to the elliptical polarisation of the orders the orientation of the in-plane sum field vector is not constant in time for all lateral sample positions. (B) shows the in-plane sum field vector at different lateral sample positions x for different points in time (dashed arrows). Its orientation is only constant for $x = 0$ and $x = 1/2d_s$. Consequently, the contrast $c = m_{an} \cdot m_\beta$ of the effective in-plane pattern beyond the analyser is not constant but varies with the orientation of the polarisation analyser in the emission path (D). The intensity of the axial intensity component $I_z(x)$ modulates in-phase with $I_l(x)$ (C). Consequently, the residual intensity distribution $I_{NoA}(x) = bI_z(x) + I_l(x)$, captured by the camera without the polarisation analyser in the emission path, corresponds to an intensity grating.

which corresponds to an intensity grating with a pattern frequency k_{illu} and a contrast c_{NoA} of:

$$c_{NoA} = \frac{c_{NoA,max} - c_{NoA,min}}{c_{NoA,max} + c_{NoA,min}} = \frac{b+1}{b+1/m_l} \,, \tag{5.4}$$

where m_l depends on the angle γ under which the illumination light is incident on the sample, i.e. the angle between either diffraction order and the optical axis:

$$m_l = \frac{1-\cos^2(\gamma)}{1+\cos^2(\gamma)} \,. \tag{5.5}$$

Consequently, the residual grating contrast c_{NoA} depends on the illumination angle γ; the greater the angle, the higher the contrast of $I_{NoA}(x)$ becomes.

For comparison of the residual grating contrast under different angles of incidence, the contrast of the residual grating c_{NoA} was experimentally compared for two different positions of the grating in the illumination path. Positioning the grating before L_3 (Fig. 4.1) corresponds to an angle of incidence on the sample of approximately $\gamma = 11°$ whereas positioning it before L_5 (Fig. 4.1) yields an angle of approximately $\gamma = 50°$. For each grating position, 20 images of different sample regions were acquired. In the course of image processing, the background offset was subtracted and a Hann window function was used to dim the edges of the images. The contrast of the residual grating c_{NoA} was obtained from:

$$c_{NoA} = \frac{2|\tilde{I}_{+1}|}{|\tilde{I}_0|} \frac{otf_0}{otf_{+1}} \,, \tag{5.6}$$

where $\tilde{I}_0$ and $\tilde{I}_{+1}$ are the complex values of the Fourier-transformed images at the position of the 0^{th}- and $+1^{st}$-order peak respectively and otf_0 and otf_{+1} are the values of the 2D OTF at the position of the 0^{th} and $+1^{st}$-order peak respectively. The second

fraction in the equation was introduced to compensate for the fact that due to the shape of the 2D OTF the transfer strength for higher frequencies is lower than the one for lower frequencies. If one were to compare the contrast of two gratings with different frequencies and identical grating contrast, the contrast of the high frequency grating would erroneously calculate to a lower value without this correction term. The OTF used for the calculation was obtained from a FT of the simulated PSF described in 4.4.2.

The mean contrast for $\gamma = 11°$ calculates to $2.2\% \pm 0.03$. As expected, the contrast for $\gamma = 50°$ calculates to a higher value of $7.3\% \pm 0.3$.

5.1.2 The phase-shift of the effective illumination pattern in picoSIM

In accordance with theory the orientation of the polarisation analyser in the emission path can retroactively select the position of the effective illumination pattern imaged onto the camera. Figure 5.3 illustrates the phase shift of the detected grating when rotating the analyser. In total, the polariser was rotated by 180° which corresponds in theory to a phase shift of the grating of 360° (cf. Eq. 3.20). As described above, the distance of each data point from the origin indicates the OTF-corrected pattern contrast (see 5.1).

Figure 5.3 reveals a varying contrast of the detected pattern stretching from a minimum value of 12.2% up to a maximum value of 19.9% out of a theoretically possible value of 50% (assuming a fluorescene anisotropy of $r_0 = 0.4$, which is the maximum possible value for a single photon process with randomly oriented fluorophores).

Assuming an illumination satisfying the paraxial approximation and thus yielding a perfect picoSIM polarisation distribution in the sample (Fig. 3.8), one would expect a circular distribution of data points centred around the origin. However, a closer inspection of the effect of the non-paraxial illumination and the polarisation analyser reveals the reason for the non-circular distribution of data points.

Following the theory outlined in 5.1.1, the intensity distribution $I_A(x)$, detected by the camera with the analyser in the emission path, can be described as a superposition

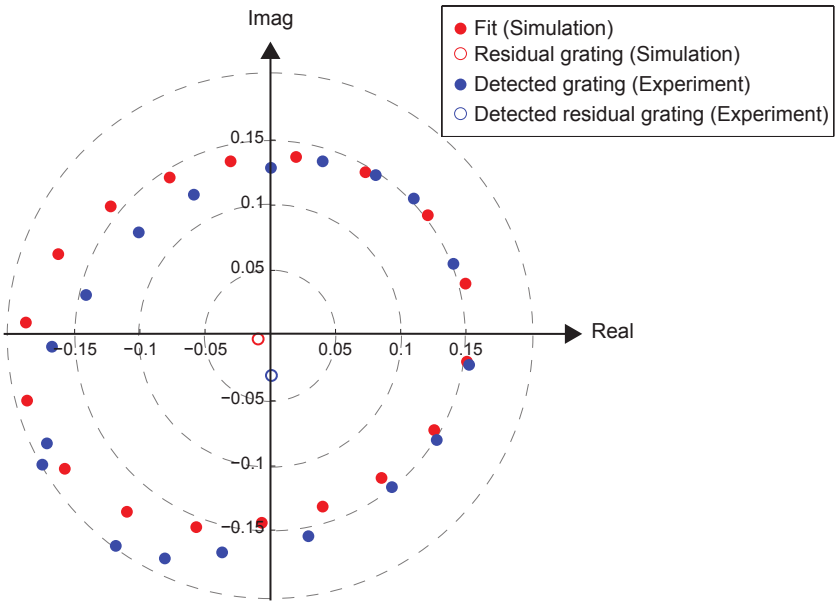

Fig. 5.3: The phase-shift of the effective illumination pattern in picoSIM: The polarisation analyser in the emission beam path was rotated manually in steps of 10° over a range of 180°. This corresponds to a 360° phase shift of the grating imaged onto the camera. The phase of the grating in each of the images (blue dots) was calculated out of the $+1^{st}$ order peak in Fourier space in such a way, that the distance of each data point from the origin corresponds to the effective pattern contrast in the sample. The phase of the residual grating (blue circle), present in the sample without a polarisation analyser positioned in the emission beam path, was calculated accordingly and plotted as well. The fit (shown in red) is based on a simulation and represents a least-square fit to the data.

between the axial and the lateral intensity distribution after being captured by the objective and filtered by the polarisation analyser:

$$I_A(x) = [\, bI_z(x) \,]_f + [\, I_l(x) \,]_f \;, \tag{5.7}$$

where the $[\,]_f$ refers to the effect of the polarisation analyser (see below).

The light stemming from the axial component $I_z(x)$ is assumed to be randomly polarised with respect to the analyser plane. Hence, only 50% of the light captured by the objective will be transmitted:

$$[\ bI_z(x)\ ]_f = \frac{1}{2} bI_z(x)\ . \tag{5.8}$$

The polarisation analyser retroactively selects the actual in-plane pattern from the lateral intensity distribution $I_l(x)$:

$$[\ I_l(x)\ ]_f = \frac{1}{2} I_l(x)[1 - m_{an} m_\beta \cos(kx + 2\beta - \varepsilon)]\ , \tag{5.9}$$

where $I_l(x)$ scales the magnitude depending on the lateral sample position, m_{an} and m_β define the contrast of the actual in-plane pattern beyond the analyser and β corresponds to the orientation of the analyser.

The parameter m_{an} accommodates for the loss in pattern contrast due to fluorescence anisotropy (see 2.6). A further reduction in contrast is possible due to the elliptical polarisation of the in-plane illumination order components. Their superposition yields an in-plane sum field vector whose orientation is not constant in time (Fig. 5.2B) for all lateral sample positions (as would be the case for an illumination satisfying the paraxial approximation). Consequently, the contrast of the effective in-plane pattern beyond the analyser depends not only on fluorescence anisotropy, but also on the orientation of the polarisation analyser in the emission path (Fig. 5.2D):

$$m_\beta = \frac{1}{1 + c_\beta}[1 + c_p \cos(4\beta)]\ , \tag{5.10}$$

where c_β is a parameter defining the modulation of m_β for varying β.

In accordance with the theory described, a simulation was written to least-square fit the data (Fig. 5.3) using the following fitting parameters:

$a_1 \cdot b$: The peak-to-peak amplitude a_1 of the axial intensity distribution $I_z(x)$ and the fraction b of $I_z(x)$ captured by the objective were combined to one fitting parameter.

ε: A global phase.

a_2: The peak-to-peak amplitude of the lateral intensity distribution $I_l(x)$.

m_l: The modulation of the lateral intensity $I_l(x)$.

m_{an}: The reduction in modulation of the in-plane pattern beyond the analyser due to fluorescence anisotropy.

c_β: The reduction in modulation of the in-plane pattern depending on the analyser orientation.

The minimisation calculated the following values for the fitting parameters:

$a_1 \cdot b$:	0.0021
ε:	19.4927
a_2:	0.1131
m_l:	0.0097
m_{an}:	0.1739
c_β:	0.1154

It can be seen from Fig. 5.3 that the contrast values of the data points on the right-hand side of the "Imag"-axis approximately correspond to the theory described. In contrast, their phase positions do not. On the left-hand side of the "Imag"-axis neither the phase positions nor the contrast values retrieved from the experimental data could be predicted perfectly by the simulation. Moreover, the phase position of the residual

grating data point severely deviates from the fit.

A possible reason for the detected phase values not being in accordance with the fit can be found in the polarisation analyser positioned right in front of the camera. If the surface of the analyser is not orthogonal to the optical axis, the emission light will be deviated and the image on the camera will be shifted. The effect on Fig. 5.3 would be a data point with a true contrast value at an incorrect phase position. To correct for this deviation in Fig. 5.3, the residual grating data point would have to be rotated by the phase deviation introduced by positioning the analyser in the emission path. However, not only does the phase position of the residual grating deviate from the simulation, but so does that of the remaining data points, indicating that the image shift on the camera is not constant. This non-constant phase error might be caused by a further misalignment due to rotating the analyser manually.

A possible reason for the incorrect contrast values is a misalignment of the $\lambda/4$-plates leading to the diffraction order being not circularly but rather elliptically polarised. For the simulation on which the fit is based, circularly polarised diffraction orders were assumed. Moreover, the contrast value for each data point was computed using a theoretical calculated intensity OTF. As this OTF deviates from the experimental OTF, the accuracy of the contrast values shown in Fig. 5.3 is limited.

Without these shortcomings, Fig. 5.3 should provide an even better knowledge of the relationship between analyser position, detected grating contrast and detected grating phase. This information could then be used to find the analyser orientations suited best for the reconstruction of the final picoSIM image.

5.1.3 The successively acquired biological sample data

As a biological application Fig. 5.4 depicts images of fixed adult rat myofibrils. Figure 5.4a shows the standard wide-field image whereas Fig. 5.4b shows the optically sectioned image. The three raw images (Fig. 5.5) necessary for the picoSIM reconstruction were acquired successively. The reconstructed image shows a thin slice of the sample that contains only in-focus information; the out-of-focus light has been removed

in the reconstruction process.

The reconstructed biological data shows that our algorithm is able to cope not only with a reduced pattern contrast and signal-to-noise due to fluorescence anisotropy but also with a varying pattern contrast in the raw images (see 5.1.2).

The importance of fluorescence anisotropy for picoSIM was described in [20]. For single photon processes, the anisotropy r can reach values up to $r_0 = 0.4$ (see 2.6). This value corresponds to a decrease in modulation contrast and therefore signal-to-noise by a factor of two compared to conventional SIM. Any value of $r_0 < 0.4$ will reduce the signal-to-noise further. The biological data presented demonstrates that the Cy2 labelling described in 4.2.3 is suitable for picoSIM. However, the illumination contrast c_{illu} in the raw images allows evaluation of the fluorescence anisotropy r_0 of the sample [20]:

$$r_0 = \frac{2c_{illu}}{3 - c_{illu}} , \tag{5.11}$$

where c_{illu} can be retrieved from the data similarly as described for c_{NoA} in Eq. 5.6. For the raw image with the best illumination contrast, the anisotropy calculates to $r_0 = 0.05$. This value only represents a lower limit as out-of-focus light disturbs the measurement of c_{illu}. Moreover, the theoretical OTF used for calculating c_{illu} leads to erroneously small values. Finally, none of the raw images may have been acquired with the optimum analyser orientation, i.e. the analyser orientation leading to the best possible illumination contrast. In theory all dye-linker combinations with a higher fluorescence anisotropy should lead to better results.

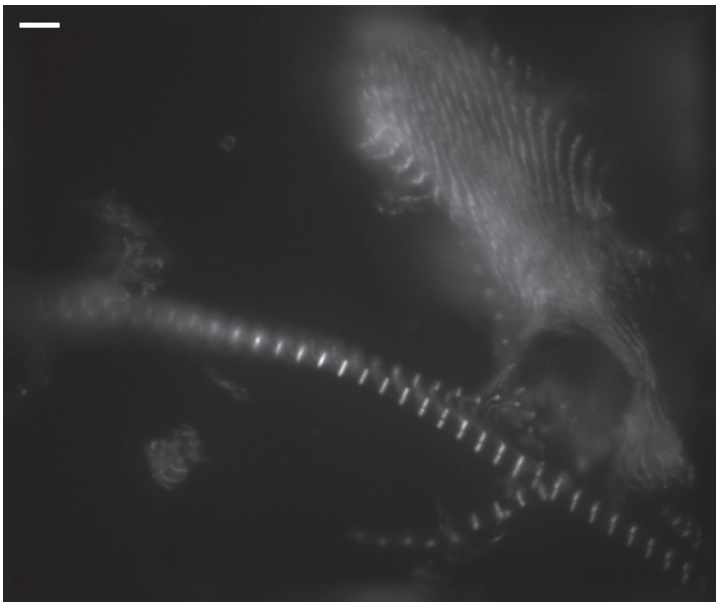

(a) Wide-field

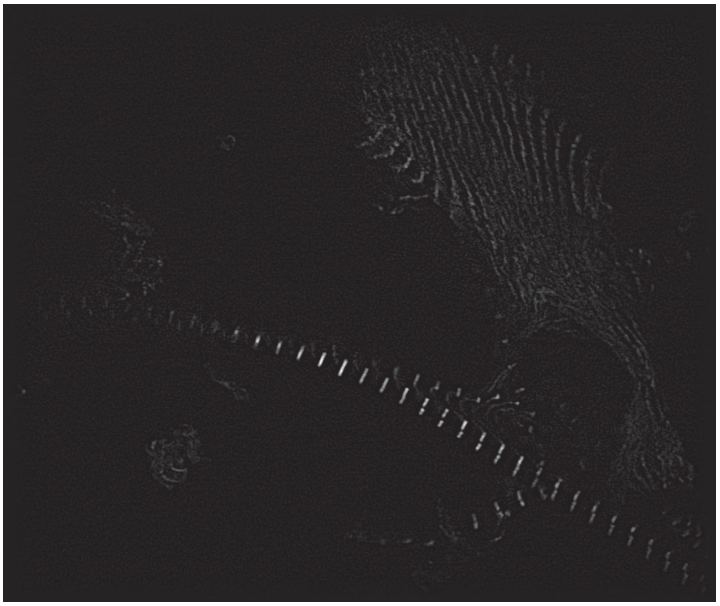

(b) picoSIM reconstruction

Fig. 5.4: Reconstruction of successively acquired biological sample data: Images of fixed adult rat myofibrils, stained with monoclonal mouse antibodies against the titin epitope T12 and secondary Cy2-conjugated anti-mouse immunoglobulin antibodies. (a) shows the standard wide-field image (calculated as the inverse FT of the separated 0^{th} order component, i.e. the unshifted wide-field component) whereas (b) shows the optically sectioned image after reconstruction of the three successively acquired raw images. Exposure time: $50ms$, Excitation wavelength: $473nm$, Camera: CCD, Laser: $130mW$, Grating constant in sample space: $d_s = 1.23\,\mu m$, Scale bar: $5\,\mu m$

Fig. 5.5: Successively acquired biological sample data: Raw images of fixed adult rat myofibrils, stained with monoclonal mouse antibodies against the titin epitope T12 and secondary Cy2-conjugated anti-mouse immunoglobulin antibodies. Exposure time: 50 ms, Excitation wavelength: 473 nm, Camera: CCD, Laser: 130 mW, Grating constant in sample space: $d_s = 1.23\,\mu m$

5.2 picoSIM: Single-shot optical sectioning

This section presents the data acquired with the picoSIM setup depitcted in 4.1. Wherever necessary variations from the standard picoSIM data acquisition and processing routines discussed in 4.3 and 4.4 are stated.

5.2.1 The sectioning performance of picoSIM

For the picoSIM sectioning curves shown in Figs. 5.6a and 5.6b, the mean intensity of each of the reconstructed slices of a z-stack, acquired using a fluorescent plane sample (see 4.2.2), was calculated and plotted against the focus position. The reconstruction was carried out in a slice-by-slice fashion in order to reduce computing time. Another benefit of this approach is that in theory it allows the optimisation of the mixing matrix for each slice individually, leading to an improved order separation and thus a final image with fewer artefacts. However, in practice this was not feasible. Due to the decreasing signal-to-noise for out-of-focus regions, it was not possible to retrieve the reconstruction parameters as described in 4.4.2 for each individual slice. Therefore, the parameters determined for the focal slice were retrieved and used for the reconstruction of all other slices.

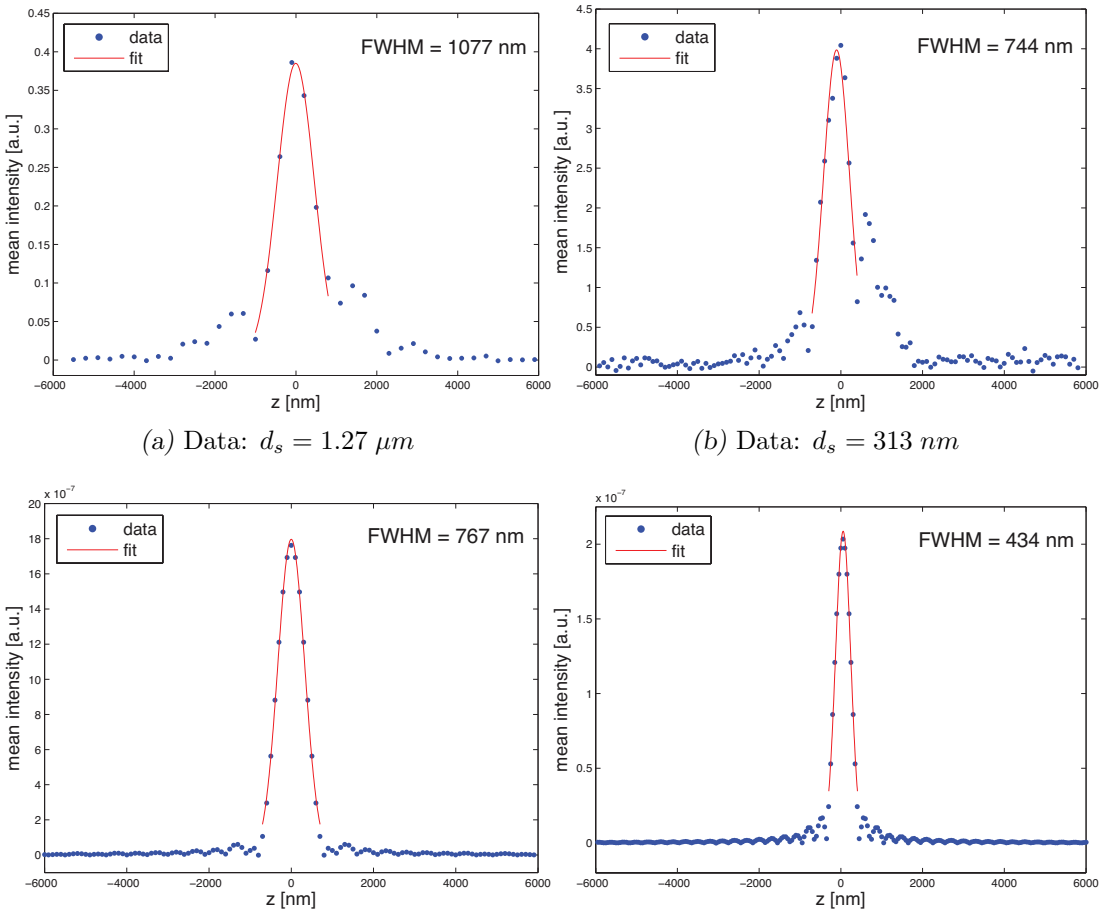

(a) Data: $d_s = 1.27\ \mu m$ *(b)* Data: $d_s = 313\ nm$

(c) Simulation: $d_s = 1.27\ \mu m$ *(d)* Simulation: $d_s = 312\ nm$

Fig. 5.6: The picoSIM sectioning performance: The data underlying (a) [(b)] consists of a stack with 40 [60] picoSIM images of a fluorescent plane sample, each acquired at a different focus position. The step size between each of the images equals 300 nm [100 nm] along the z-axis. Each of the 40 [60] images was processed utilising the hrSIM algorithm yielding a reconstructed slice. Each data point (shown in blue) represents the mean intensity of one reconstructed slice at the focus position z. For the plot shown in (c) [(d)], simulated data was processed in a similar way. A simulated wide-field PSF (see 4.4.2) was used for the simulation. The step size between the slices was chosen to be 100 nm [50 nm]. The finite thickness of the fluorescent plane sample was disregarded in the simulation. However, due to the relatively small value of 115 nm, the curves are not affected by this simplification. Furthermore, noise and a varying pattern contrast were disregarded. To calculate the FWHM, a Gaussian function (shown in red) was fitted both to the experimentally acquired and the simulated data. For the fit only the data points belonging to the central peak were considered.

Figures 5.6a and 5.6b exhibit side lobes around the central peak of the sectioning curve. These side lobes are also present in the plots shown in Figs. 5.6c and 5.6d which are based on a simulation of the experiment. However, the asymmetrical distribution of data points in Figs. 5.6a and 5.6b, as well as the varying width of the central lobe and the side lobes as compared to the simulation, reveal aberrations in the picoSIM system. The presence of astigmatism can be seen from the varying shape of the beads in the close up view in Figs. 4.6a and 4.6c. Another reason for the discrepancy between the experimental and the simulated curves is the presence of artefacts in the reconstructed data set, which arise due to the reconstruction parameters not being retrieved for each slice individually. Furthermore, it can be seen that all four curves in Fig. 5.6 exhibit only positive values. While an in-focus OTF is known to be all positive, a 2D out-of-focus OTF will exhibit negative values for some frequencies. Thus one would expect negative values in the curves to appear. The reason for the curves to remain all positive is the reconstruction algorithm assuming the same in-focus OTF independent of defocus. This results in a small positive reconstructed brightness instead of a negative value in the side lobes. However, the determined width of the central peak and thus the quality of the sectioning is unaffected by the sign of the side lobes.

The sectioning performance of the setup was judged by the FWHM of a Gaussian fit to the data. For higher accuracy only the data points belonging to the central peak were considered for the fit, yielding a FWHM of 1077 nm and 744 nm respectively. Similarly, the FWHM of the simulation calculates to 767 nm and 434 nm respectively.

The sectioning performance depends on the position of the higher order components in Fourier space, i.e. on the period length of the effective illumination pattern as described both in 3.1.2 and 4.1.6. The data underlying Fig. 5.6b was acquired with the grating positioned before L_5 (Fig. 4.1) leading to a grating constant in the sample that is finer than the optimum for optical sectioning. In accordance with theory, positioning the grating before L_3 (Fig. 4.1), i.e. using a much coarser grating than the optimum, leads to a diminished sectioning performance as can be seen in Fig. 5.6a.

5.2.2 picoSIM applied to a fixed biological sample

Figure 5.7 shows single-shot optically sectioned images acquired with different exposure times. It can be seen that picoSIM appreciably suppresses the out-of-focus light present in the wide-field images. The results show that not only the Cy2 labelling (Fig. 5.4) but also the DyLight488 labelling, described in 4.2.3, is suitable for picoSIM.

With a size of approximately $22\,\mu m \times 16\,\mu m$, the field of view is smaller than should be theoretically possible. The reason is that the image splitter (see 4.1.8) was designed to be used with an optical system utilising a telecentric design of the emission path. Due to the non-telecentric arrangement of the objective and emission tube lens in our Zeiss microscope, the chief rays beyond the tube lens are not parallel to the optical axis anymore (Fig. 5.8). Utilising the full field of view ($44.4\,\mu m \times 33.5\,\mu m$ for the CCD and $66.0\,\mu m \times 66.0\,\mu m$ for the sCMOS camera) would lead to parts of the light being blocked within the image splitter, leading to artefacts in the final image. To avoid this, the field of view had to be reduced by adjusting the rectangular aperture RA (Fig.4.4) accordingly. As this complex of problems was unknown when designing the illumination side of the picoSIM setup, the system was optimised for a field of view of $44.4\,\mu m \times 33.5\,\mu m$. Hence, illumination intensity is currently lost by illuminating sample regions not being imaged onto the camera. Redesigning the illumination side of the setup will increase the light efficiency of the system and allow for shorter exposure times. Alternatively, the image splitter could be redesigned to image a larger field of view.

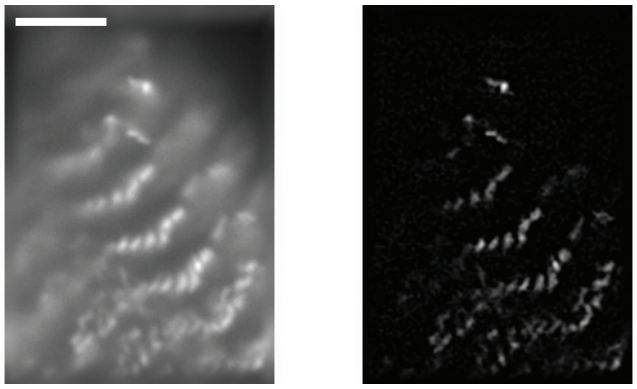

(a) Wide-field (10 ms)

(b) picoSIM reconstruction (10 ms)

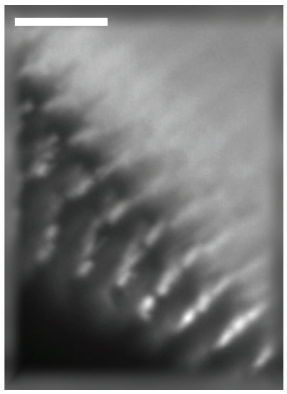

(c) Wide-field (20 ms)

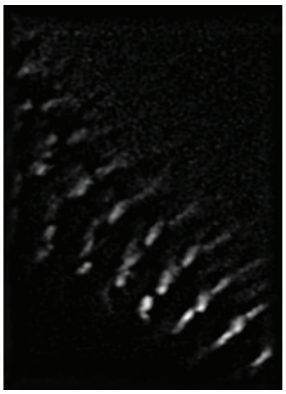

(d) picoSIM reconstruction (20 ms)

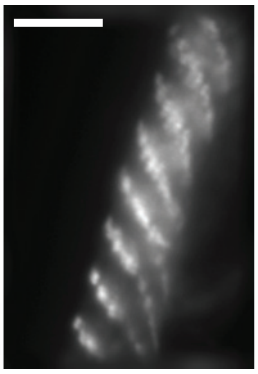

(e) Wide-field (50 ms)

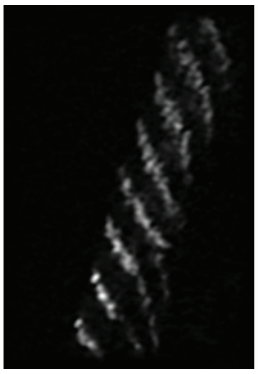

(f) picoSIM reconstruction (50 ms)

Fig. 5.7: Reconstruction of single-shot picoSIM data: Images of fixed adult rat myofibrils, stained with monoclonal mouse antibodies against the titin epitope T12 and secondary DyLight488-conjugated anti-mouse immunoglobulin antibodies. (a), (c) and (e) show the standard wide-field images (calculated as the inverse FT of the separated 0^{th} order component, i.e. the unshifted wide-field component) whereas (b), (d) and (f) show the reconstructed single-shot picoSIM images. The results show that picoSIM appreciably suppresses the out-of-focus light present in the wide-field images. Exposure time: 10 ms, 20 ms and 50 ms respectively, Excitation wavelength: 473 nm, Camera: sCMOS, Laser: 130 mW, Grating constant in sample space: $d_s = 1.23\,\mu m$, Scale bar: 5 μm

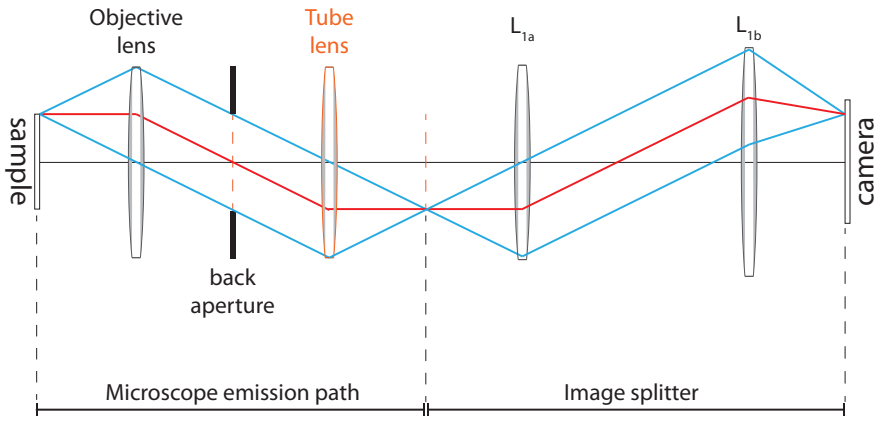

(a) Telecentric

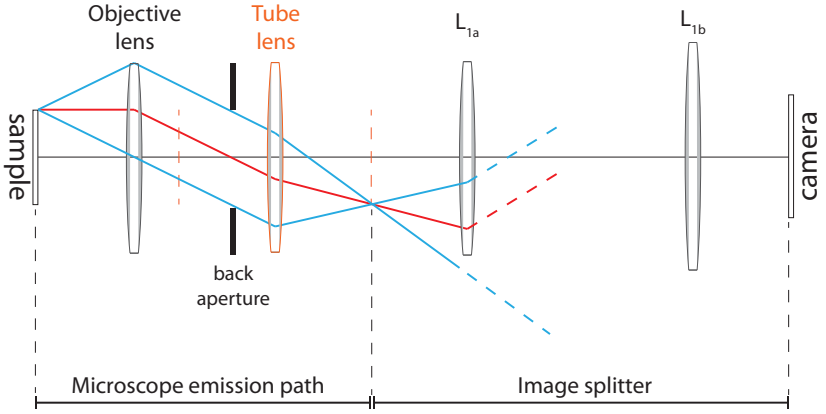

(b) Non-telecentric

Fig. 5.8: Field of view considerations: In this schematic view of the emission path for one of the four beams imaged onto the camera the chief ray is shown in red, the axial rays are shown in blue and the two focal planes of the tube lens are shown in orange. The intermediate image, generated in the back focal plane of the tube lens, is relayed onto the camera via the lenses L_{1a} and L_{1b} of the image splitter (cf. Fig. 4.4). (a) shows a setup with a telecentric arrangement of objective and tube lens. In this ideal case every single point of the field of view in the sample is imaged onto the camera. In the non-telecentric case shown in (b), the chief ray beyond the tube lens is not parallel to the optical axis anymore. Using the same image splitter as in (a) leads to part of the light being not accepted by the image splitter. The effect is a loss of sample information leading to artefacts in the image.

6. PICOSIM: CONCLUSION AND FUTURE WORK

The data presented in 5.1 shows that picoSIM works in principle. On the illumination side of the system, the interference of the circularly polarised -1^{st} and $+1^{st}$ diffraction orders yields the desired polarisation distribution in the sample, albeit with an unwanted residual grating (Fig. 5.1b). By rotating the polarisation analyser, positioned in the emission path of the optical system, it is possible to retroactively choose the effective illumination pattern position (Fig. 5.3). Out of the three successively acquired raw images, a final optically sectioned image can be calculated (Fig. 5.4).

Splitting the emission light into four beams and filtering each of them using a polarisation analyser allows one to acquire the raw images needed for a SIM reconstruction in a single exposure (Fig. 5.7).

In conclusion, picoSIM allows optical sectioned imaging with higher acquisition rates as compared to conventional SIM and confocal microscopy.

The current picoSIM setup can be optimised in various ways in order to become a good alternative for high speed optical sectioned imaging, not only in the field of fluorescence microscopy but also for reflected and scattered light.

The sectioning performance of the current picoSIM setup was judged by calculating the FWHM of the Gaussian fit shown in Fig. 5.6b. The value of $FWHM = 744\,nm$ can still be improved by replacing the laser illumination by an incoherent light source (see 3.2.4). Due to the order separation in plane $P_{3,4}$ and $P_{5,6}$ (Fig. 4.1) respectively, needed to generate the picoSIM illumination, the use of incoherent light is currently not feasible. However, in a collaboration with Prof. Stefan Nolte (Institute of Applied Physics, Jena, Germany) we are currently testing so-called nanogratings, i.e. fs-laser induced sub-wavelength structures with birefringent properties [57], which allow the gen-

eration of a position dependent polarisation distribution as needed in picoSIM. Hence, the setup components currently generating the polarisation distribution on the illumination side (see 4.1) will eventually become obsolete and be replaced by a nanograting inserted at the field diaphragm position in the illumination path of a conventional fluorescence microscope. This simplification will allow the use of incoherent light and thus improve the sectioning performance of picoSIM.

In order to increase the field of view of currently approximately 22 $\mu m \times 16\ \mu m$ (see 5.2.2), the image splitter has to be redesigned and optimised for the microscope in use. However, if all four beams are imaged onto the same camera sensor, the maximum field of view calculates to one quarter of the sensor size divided by the magnification of the system. Alternatively, the four beams could be directed onto multiple synchronised cameras, increasing the field of view up to the size of the camera sensor if four cameras are used.

In the current setup, light intensity is lost by illuminating parts of the sample that are not imaged onto the camera. To decrease the exposure time and increase the acquisition rate, the illumination side of the system has to be optimised in such a way that only the field of view imaged onto the camera is illuminated. Furthermore, finding dye-linker combinations with higher anisotropy values will increase the signal-to-noise and thus allow shorter exposure times.

Finally, in order to reduce photobleaching in live cell imaging, an acousto-optical tunable filter (AOTF) should be used to trigger the illumination parallel to the acquisition of the camera.

On the experimental side the next step will be to acquire videos of fast biological processes.

Appendix

A. MATHEMATICAL DERIVATIONS

A.1 Intensity pattern generated by two-beam illumination

A linearly polarised, monochromatic and coherent beam of light is directed onto the SIM diffraction grating with grating constant $\vec{k}_g = (k_{g,x}, 0, 0)$. When blocking the 0^{th} and all higher diffraction orders beyond the grating, only the -1^{st} and $+1^{st}$ orders will be focused to generate two foci in the back focal plane (BFP) of the objective lens. Either of these diffraction orders m ($m = \{-1, +1\}$) corresponds to a plane wave $E\,exp[\imath(\vec{k}_m \cdot \vec{r} + \varphi_m)]$ in sample space, with $\vec{k}_m$ being defined by the position of the BFP focus' projection onto the McCutchen generalised aperture. The interference of the plane waves in sample space yields the intensity pattern:

$$\begin{aligned} I(\vec{r}) &= \left| \sum_{m=\pm 1} E\,exp[\imath(\vec{k}_m \cdot \vec{r} + \varphi_m)] \right|^2 \\ &= \left[\sum_{m=\pm 1} E\,exp[\imath(\vec{k}_m \cdot \vec{r} + \varphi_m)] \right] \left[\sum_{m=\pm 1} E\,exp[\imath(\vec{k}_m \cdot \vec{r} + \varphi_m)] \right]^* \\ &= 2|E|^2 + |E|^2 \left[exp[\imath(\Delta\vec{k} \cdot \vec{r} + \Delta\varphi)] + exp[-\imath(\Delta\vec{k} \cdot \vec{r} + \Delta\varphi)] \right] , \end{aligned} \tag{A.1}$$

with $\Delta\vec{k} = \vec{k}_{+1} - \vec{k}_{-1}$ and $\Delta\varphi = \varphi_{+1} - \varphi_{-1}$. In the situation described above $\vec{k}_{+1} = (k_{g,x}, 0, k_z)$ and $\vec{k}_{-1} = (-k_{g,x}, 0, k_z)$. Equation A.1 thus becomes:

$$I(\vec{r}) = 2|E|^2[1 + cos(2k_{g,x}x + \Delta\varphi)] \, . \tag{A.2}$$

This standing wave intensity pattern has a frequency twice as high as the grating fre-

quency $k_{g,x}$, a direct consequence of blocking the 0^{th} order. Furthermore, the intensity distribution only depends on the x-coordinate and is therefore constant along the optical axis.

As we just saw, coherent illumination of the SIM diffraction grating yields one pair of coherent foci (when the $0th$ order is blocked) in the BFP of the objective. Illuminating the diffraction grating with incoherent light and blocking the 0^{th} order yields multiple such pairs of coherent foci being mutually incoherent. The distance between two BFP spots belonging to one pair is constant and corresponds to $2\vec{k}_g$. However, the position of the pairs, when projecting them onto McCutchen's generalised aperture, differs. This varying position of the pairs of spots corresponds to different illumination angles with which the sample is illuminated. One pair of spots can be treated as already described for the single pair in case of coherent illumination. The final intensity distribution in sample space is the sum of the individual intensity patterns generated by each pair. This intensity distribution will resemble the one derived for coherent light only in the focal plane of the objective; for out-of-focus regions the contrast of the intensity pattern decreases.

A.2 Filling the missing cone in sSIM

This derivation is based on [20] and [27].

To analyse the sectioning capability of sSIM we consider:

$$I_{sSIM}(\vec{r}_{xy}) = |\sum_{n=1}^{3} I_n(\vec{r}_{xy}) \quad exp(\imath\frac{2\pi n}{3})| \,, \tag{3.5}$$

which, using:

$$I_n(\vec{r}_{xy}) = [I_{em,n} \otimes h_{det}](\vec{r})\Big|_{z=0} \tag{3.3}$$

and:

$$I_{em,n}(\vec{r}) = I_{illu,n}(\vec{r})S(\vec{r}) \,, \tag{3.2}$$

can be written as:

$$I_{sSIM}(\vec{r}_{xy}) = |[(\sum_{n=1}^{3} I_{illu,n} exp(\imath\frac{2\pi n}{3})S) \otimes h_{det}](\vec{r})|\Big|_{z=0} . \tag{A.3}$$

Using $\sum_{n=1}^{3} exp(\imath\frac{2\pi n}{3}) = 0$ and Eq. 3.1 the sum becomes:

$$\begin{aligned}
&\sum_{n=1}^{3} I_{illu,n}(\vec{r}) exp(\imath\frac{2\pi n}{3}) \\
=&\sum_{n=1}^{3} \frac{A}{2}\left[\delta(z)[1+\cos(\vec{k}_{illu}\cdot\vec{r}+\frac{2\pi n}{3})]\right] exp(\imath\frac{2\pi n}{3}) \otimes h_{illu}(\vec{r}) \\
=&\sum_{n=1}^{3} \frac{A}{4}\left[\delta(z)[exp(\imath\vec{k}_{illu}\cdot\vec{r})exp(\imath\frac{2\pi n}{3}) + exp(-\imath\vec{k}_{illu}\cdot\vec{r})exp(-\imath\frac{2\pi n}{3})]\right] exp(\imath\frac{2\pi n}{3}) \otimes h_{illu}(\vec{r}) \\
=&\sum_{n=1}^{3} \frac{A}{4}[\delta(z)exp(-\imath\vec{k}_{illu}\cdot\vec{r})] \otimes h_{illu}(\vec{r}) \\
=&\frac{3}{4}A\, exp(-\imath\vec{k}_{illu}\cdot\vec{r})m(\vec{r}) ,
\end{aligned} \tag{A.4}$$

with the modulation function:

$$m(\vec{r}) = \delta(z) \otimes [h_{illu}(\vec{r})exp(\imath\vec{k}_{illu}\cdot\vec{r})] = \mathcal{F}^{-1}\{\delta(k_x)\delta(k_y)\tilde{h}_{illu}(\vec{k}-\vec{k}_{illu})\}(\vec{r}) . \tag{3.7}$$

Equation 3.5 can then be written as:

$$
\begin{aligned}
I_{sSIM}(\vec{r}_{xy}) &= \frac{3}{4}A|[exp(-\imath\vec{k}_{illu}\cdot\vec{r})m(\vec{r})S(\vec{r})]\otimes h_{det}(\vec{r})|\Big|_{z=0} \\
&= \frac{3}{4}A|exp(-\imath\vec{k}_{illu}\cdot\vec{r})\left[[m(\vec{r})S(\vec{r})]\otimes[exp(\imath\vec{k}_{illu}\cdot\vec{r})h_{det}(\vec{r})]\right]|\Big|_{z=0} \\
&= \frac{3}{4}A|[m(\vec{r})S(\vec{r})]\otimes[exp(\imath\vec{k}_{illu}\cdot\vec{r})h_{det}(\vec{r})]|\Big|_{z=0} \\
&= \frac{3}{4}A|[(mS)\otimes h_{det}^{'}](\vec{r})|\Big|_{z=0},
\end{aligned}
\tag{A.5}
$$

with the effective detection PSF:

$$
h_{det}^{'}(\vec{r}) = exp(\imath\vec{k}_{illu}\cdot\vec{r})h_{det}(\vec{r}) = \mathcal{F}^{-1}\{\tilde{h}_{det}(\vec{k}-\vec{k}_{illu})\}(\vec{r})\ . \tag{3.8}
$$

A.3 The hrSIM reconstruction process

The following paragraphs, explaining the individual steps of the reconstruction for a two-beam hrSIM system in more detail, are based on [58] and [27].

Matrix notation In order to separate M object components present in a Fourier-transformed SIM image, at least $N \geq M$ images $I_n^{(z_0)}(\vec{r}_{xy})$ (with $n = 1, 2, ..., N$) with different illumination pattern positions $I_{illu,n}(\vec{r})$ must be acquired. As a two-beam hrSIM illumination yields $M = 3$ object components of order m (with $m = -1, 0, +1$) in the Fourier-transformed image, at least $N = 3$ raw images $I_n^{(z_0)}(\vec{r}_{xy})$ (with $n = 1, 2, ..., N$) with different pattern phases ϕ_n in the sample should be acquired:

$$
I_{illu,n}(\vec{r}) = \frac{A}{2}[1+\cos(\vec{k}_{illu}\cdot\vec{r}+\phi_n)] \quad (n = 1, 2, ..., N)\ , \tag{A.6}
$$

which corresponds to:

$$\tilde{I}_{illu,n}(\vec{k}) = \frac{A}{2}\left[\delta(\vec{k}) + \frac{1}{2}[e^{-\imath\phi_n}\delta(\vec{k}+\vec{k}_{illu}) + e^{\imath\phi_n}\delta(\vec{k}-\vec{k}_{illu})]\right] \tag{A.7}$$

in k-space. The imaging process yields the following 2D image in the camera plane:

$$\tilde{I}_n^{(z_0)}(\vec{k}_{xy}) = \int_{-\infty}^{+\infty} \sum_m A_m e^{\imath m\phi_n}\left[[e^{-\imath k_z z_0}\tilde{S}(\vec{k})] \otimes \delta(\vec{k} - m\vec{k}_{illu})\right] \cdot \tilde{h}_{det}(\vec{k})\, dk_z \ . \tag{A.8}$$

Defining the m^{th} object component $\tilde{\Omega}_m^{(z_0)}(\vec{k}_{xy})$ as:

$$\tilde{\Omega}_m^{(z_0)}(\vec{k}_{xy}) \equiv A_m \int_{-\infty}^{+\infty}\left[[e^{-\imath k_z z_0}\tilde{S}(\vec{k})] \otimes \delta(\vec{k} - m\vec{k}_{illu})\right] \cdot \tilde{h}_{det}(\vec{k})\, dk_z \tag{A.9}$$

yields:

$$\tilde{I}_n^{(z_0)}(\vec{k}_{xy}) = \sum_m e^{\imath m\phi_n}\tilde{\Omega}_m^{(z_0)}(\vec{k}_{xy}) \ . \tag{A.10}$$

Considering $\tilde{I}_n^{(z_0)}(\vec{k}_{xy})$ as the n^{th} component of a vector of images $\vec{\tilde{I}}^{(z_0)}(\vec{k}_{xy})$ allows us to rewrite the above equation using a matrix notation:

$$\vec{\tilde{I}}^{(z_0)}(\vec{k}_{xy}) = \mathbf{M}\,\vec{\tilde{\Omega}}^{(z_0)}(\vec{k}_{xy}) \ , \tag{A.11}$$

with:

$$\begin{aligned}\vec{\tilde{I}}^{(z_0)}(\vec{k}_{xy}) &= \left(\tilde{I}_1^{(z_0)}(\vec{k}_{xy}),\, \tilde{I}_2^{(z_0)}(\vec{k}_{xy}), ...,\, \tilde{I}_N^{(z_0)}(\vec{k}_{xy})\right) , \\ \vec{\tilde{\Omega}}^{(z_0)}(\vec{k}_{xy}) &= \left(\tilde{\Omega}_{-1}^{(z_0)}(\vec{k}_{xy}), \tilde{\Omega}_0^{(z_0)}(\vec{k}_{xy}), \tilde{\Omega}_{+1}^{(z_0)}(\vec{k}_{xy})\right)\end{aligned} \tag{A.12}$$

and the $N \times M$ mixing matrix:

$$\mathbf{M}_{n,m} = e^{im\,\phi_n} \quad (n = 1, 2, ..., N \quad ; m = -1, 0, +1) \; . \tag{A.13}$$

Separation of object components In order to separate the object components we invert Eq. A.11:

$$\vec{\tilde{\Omega}}^{(z_0)}(\vec{k}_{xy}) = \mathbf{M}^{-1}\, \vec{\tilde{I}}^{(z_0)}(\vec{k}_{xy}) \; . \tag{A.14}$$

Matrix $\mathbf{M}_{n,m}$ has to be reversible. Hence, the grating phases $m\phi_n$ have to be chosen in such a way that all of $\mathbf{M}$'s column vectors are linearly independent. If the mixing matrix $\mathbf{M}$ is not square, i.e. if more raw images were taken than there are components to separate, the inverse $\mathbf{M}^{-1}$ can be calculated as the Moore-Penrose pseudo inverse $\mathbf{M}^{-1} = (M^\dagger M)^{-1} M^\dagger$, with the symbol † denoting the Hermitian transpose [53].

Shifting of the separated components After their separation, the object components must be shifted by $m\,\vec{k}_{illu}$ to their correct position in Fourier space, i.e. the true position of the sample information in k-space. These shifted components are:

$$\begin{aligned}\tilde{\Omega}_m^{(z_0)}(\vec{k}_{xy} + m\,\vec{k}_{illu}) &= A_m \int_{-\infty}^{+\infty} [e^{-\imath k_z z_0}\tilde{S}(\vec{k})] \cdot \tilde{h}_{det}(\vec{k} + m\,\vec{k}_{illu})\,dk_z \\ &= \int_{-\infty}^{+\infty} [e^{-\imath k_z z_0}\tilde{S}(\vec{k})] \cdot \tilde{h}_m(\vec{k})\,dk_z\ ,\end{aligned} \tag{A.15}$$

with the component specific shifted OTF:

$$\tilde{h}_m(\vec{k}) = A_m \tilde{h}_{det}(\vec{k} + m\,\vec{k}_{illu})\ . \tag{A.16}$$

Recombination of the shifted components and generalised Wiener filter deconvolution In order to obtain a near-isotropic lateral resolution enhancement in the reconstructed image, the previous steps of data acquisition and processing have to be carried out for multiple orientations o (with $o = 1, 2, .., O$ and $O \geq 3$) of the grating, yielding $O \cdot M$ separated components $\tilde{\Omega}_{o,m}^{(z_0)}(\vec{k}_{xy})$.

Noise considerations suggest recombining the separated and shifted components using a weighted averaging approach rather than a simple summation of the individual components.

Following [54], a constant mean intensity in the acquired raw images will result in the corresponding Fourier images $\tilde{I}_{o,n}^{(z_0)}(\vec{k}_{xy})$ exhibiting frequency independent noise with a standard deviation σ. After separation, each component $\tilde{\Omega}_{o,m}^{(z_0)}(\vec{k}_{xy} + m\,\vec{k}_{illu,o})$, a summation of N Fourier images whose noise add in quadrature, will exhibit frequency independent noise with a standard deviation of $\sigma = \sqrt{N}\sigma$ [54]. In contrast, the level of information that each separated and shifted component can contribute to the image is not constant but depends on the transfer strength of the shifted OTF $\tilde{h}_{o,m}(\vec{k})$ at a certain frequency position. Consequently, the signal-to-noise contribution of a component

at a specific frequency position depends on the transfer strength of the OTF at this position. At frequency positions where the component specific OTF has a low transfer strength, the component in question would contribute a high noise level but only little information to the recombined image. It is therefore advantageous to primarily use the information of a component with a higher OTF value at this position. In the process of weighted averaging, overlapping information stemming from different components is averaged with frequency dependent weights, chosen to maximise the ratio of total information transfer to total noise.

Although weighted averaging is a good way to recombine the individual sample components, it still leads to an uneven transmission of frequencies in the imaging process. A generalised Wiener filter deconvolution [59] attempts to reverse this effect by enhancing weak frequency components, thus leading to a truer representation of the image.

Applying a FT with respect to z_0 to an entire z-stack of images (acquired for evenly spaced z_0) allows to retrieve the complete 3D information of the sample and therefore the transition from 2D to 3D sample components [27]:

$$\tilde{\Omega}_{o,m}(\vec{k} + m\,\vec{k}_{illu,o}) = \tilde{S}(\vec{k})\tilde{h}_{o,m}(\vec{k})\ . \tag{A.17}$$

The recombined and filtered 3D image $\tilde{J}_{recomb}(\vec{k})$ then calculates to [54]:

$$\tilde{J}_{recomb}(\vec{k}) = \frac{\sum\limits_{o,m} \tilde{h}^*_{o,m}(\vec{k})\tilde{\Omega}_{o,m}(\vec{k} + m\,\vec{k}_{illu,o})}{\gamma + \sum\limits_{o,m} |\tilde{h}_{o,m}|^2(\vec{k})}\ , \tag{A.18}$$

where γ is the constant Wiener parameter, which has to be adjusted empirically.

Apodisation The shape of the effective OTF after Wiener filtering can cause ringing artefacts and negative values in the reconstructed image. To avoid this $\tilde{J}_{recomb}(\vec{k})$ is multiplied with an apodisation function $\tilde{h}_{goal}(\vec{k})$ attenuating higher frequencies:

$$\tilde{J}_{final}(\vec{k}) = \tilde{J}_{recomb}(\vec{k})\tilde{h}_{goal}(\vec{k}) \ . \tag{A.19}$$

The definition of $\tilde{h}_{goal}(\vec{k})$ is based on the Euclidean distance $d(\vec{k})$ between the position $\vec{k}$ and the edge of the effective OTF support. The apodisation function, which is normalised to a maximum value of one, is then $\tilde{h}_{goal}(\vec{k}) = d^{\kappa}(\vec{k})$. The parameter κ allows adjusting of the shape of the apodisation function.

Final image The final reconstructed 3D image can be obtained by an inverse FT of $\tilde{J}_{final}(\vec{k})$:

$$J_{final}(\vec{r}) = \mathcal{F}^{-1}\{\tilde{J}_{final}(\vec{k})\}(\vec{r}) \ . \tag{A.20}$$

A.4 Estimating the mixing matrix by means of an weighted autocorrelation of the Fourier-transformed raw images

This derivation is based on [52].

For the experimental results presented in 5.1.3 and 5.2.2 only a 2D data set was reconstructed. The same is true for the z-stack discussed in 5.2.1 as the 3D data set was reconstructed in a slice-by-slice fashion. Consequently, this derivation is based on a 2D consideration approximating the image formation in Fourier space as:

$$\tilde{I}(\vec{k}_{xy}) = \tilde{S}(\vec{k}_{xy})\tilde{h}(\vec{k}_{xy}) \ , \tag{A.21}$$

with:

$$\tilde{S}(\vec{k}_{xy}) = \int_{-\infty}^{+\infty} \tilde{S}(\vec{k}) \, dk_z \ , \tag{A.22}$$

and:

$$\tilde{h}(\vec{k}_{xy}) = \int_{-\infty}^{+\infty} \tilde{h}(\vec{k})\, dk_z \; . \tag{A.23}$$

(As opposed to the true 3D image formation described in 2.4)

The weighted auto-correlation of a 2D Fourier image $\tilde{A}(\vec{k}_{xy})$ at the position $\vec{k}_0$ is defined as:

$$C_w(\vec{k}_0) = [\tilde{A}(\vec{k}_{xy}) \star_w \tilde{A}(\vec{k}_{xy})](\vec{k}_0) = \frac{\iint_{-\infty}^{+\infty} w(\vec{k}'_{xy})\tilde{A}(\vec{k}'_{xy})\tilde{A}^*(\vec{k}_0 + \vec{k}'_{xy})dk'_x dk'_y}{\iint_{-\infty}^{+\infty} w(\vec{k}'_{xy})dk'_x dk'_y} \; , \tag{A.24}$$

with $\star_w$ denoting the weighted correlation operator. Calculating the weighted auto-correlation for one fixed position $\vec{k}_0$ yields a result with better signal-to-noise when dealing with noisy images as compared to the un-weighted approach [27].

To estimate the phase of the effective illumination pattern in the picoSIM raw images, the weighted auto-correlation of each Fourier image $\tilde{I}_n(\vec{k}_{xy})$ at the position $-\vec{k}_{illu}$ needs to be calculated:

$$\begin{aligned} C_{w,n}(-\vec{k}_{illu}) &= [\tilde{I}_n(\vec{k}_{xy}) \star_w \tilde{I}_n(\vec{k}_{xy})](-\vec{k}_{illu}) \\ &= \frac{\iint_{-\infty}^{+\infty} w(\vec{k}_{xy})\tilde{I}_n(\vec{k}_{xy})\tilde{I}_n^*(\vec{k}_{xy} - \vec{k}_{illu})dk_x dk_y}{\iint_{-\infty}^{+\infty} w(\vec{k}_{xy})dk_x dk_y} \; , \end{aligned} \tag{A.25}$$

with:

$$\tilde{I}_n(\vec{k}_{xy}) = \sum_m A_{n,m} e^{\imath m \phi_n} \left[\tilde{S}(\vec{k}_{xy}) \otimes \delta(\vec{k}_{xy} - m\vec{k}_{illu}) \right] \cdot \tilde{h}_{det}(\vec{k}_{xy}) \ , \tag{A.26}$$

where $A_{n,m}$ is the amplitude of the m^{th} order (with $m = -1, 0, +1$) in the n^{th} image (with $n = 1, 2, ..., N$). Equation A.26 corresponds to Eq. A.8 modified for the reconstruction of a 2D data set. By introducing $A_{n,m}$, Eq. A.26 accommodates for the varying pattern contrast in the individual raw picoSIM images. Choosing the weights to be $w(\vec{k}_{xy}) = \tilde{h}^*_{det}(\vec{k}_{xy})\, \tilde{h}_{det}(\vec{k}_{xy} - \vec{k}_{illu})$ yields:

$$\begin{aligned} C_{w,n}(-\vec{k}_{illu}) = & \frac{1}{\iint_{-\infty}^{+\infty} \tilde{h}^*_{det}(\vec{k}_{xy}) \tilde{h}_{det}(\vec{k}_{xy} - \vec{k}_{illu}) dk_x dk_y} \iint_{-\infty}^{+\infty} \Big[A_{n,0} A_{n,-1} e^{\imath \phi_n} |\tilde{S}(\vec{k_{xy}})|^2 \\ & + A_{n,0} A_{n,+1} e^{\imath \phi_n} |\tilde{S}(\vec{k}_{xy} - \vec{k}_{illu})|^2 + \Delta \Big] |\tilde{h}_{det}(\vec{k}_{xy})|^2 |\, \tilde{h}_{det}(\vec{k}_{xy} - \vec{k}_{illu})|^2 dk_x dk_y \ , \end{aligned} \tag{A.27}$$

with Δ containing correlations between sample components and random noise (expectation value 0) as well as auto-correlations of the sample components at frequency positions $\vec{k} \neq 0$ (expectation value very small compared to the $\vec{k} = 0$ case). Disregarding Δ and the denominator which is constant for every $\tilde{I}_n(\vec{k}_{xy})$ leads us to:

$$\begin{aligned} C_{w,n}(-\vec{k}_{illu}) = & A_{n,0} A_{n,-1} e^{\imath \phi_n} \iint_{-\infty}^{+\infty} |\tilde{S}(\vec{k}_{xy})|^2 |\tilde{h}_{det}(\vec{k}_{xy})|^2 |\tilde{h}_{det}(\vec{k}_{xy} - \vec{k}_{illu})|^2 dk_x dk_y \\ & + A_{n,0} A_{n,+1} e^{\imath \phi_n} \iint_{-\infty}^{+\infty} |\tilde{S}(\vec{k}_{xy} - \vec{k}_{illu})|^2 |\tilde{h}_{det}(\vec{k}_{xy})|^2 |\tilde{h}_{det}(\vec{k}_{xy} - \vec{k}_{illu})|^2 dk_x dk_y. \end{aligned} \tag{A.28}$$

Shifting the integrand of the first integral by $+\vec{k}_{illu}$ allows simplification of Eq. A.28 to:

$$C_{w,n}(-\vec{k}_{illu}) = 2\,A_{n,0}A_{n,1}e^{\imath\phi_n}\iint_{-\infty}^{+\infty}|\tilde{S}(\vec{k}_{xy}-\vec{k}_{illu})|^2|\tilde{h}_{det}(\vec{k}_{xy})|^2|\tilde{h}_{det}(\vec{k}_{xy}-\vec{k}_{illu})|^2dk_xdk_y\ , \tag{A.29}$$

where:

$$A_{n,1} := A_{n,+1} = A_{n,-1}\ . \tag{A.30}$$

As $e^{\imath\phi_n}$ is the only complex value in Eq. A.29, we can directly retrieve the phase ϕ_n of the effective illumination pattern in $I_n(\vec{r}_{xy})$ from $C_{w,n}(-\vec{k}_{illu})$.

The contrast $c_{illu,n}$ of the effective illumination pattern in $I_n(\vec{r}_{xy})$ can be calculated as:

$$c_{illu,n} = \frac{2A_{n,1}}{A_{n,0}}\ . \tag{A.31}$$

As we normalised the mean intensity of each raw image to the same value in the cause of the data preprocessing, $A_{n,0}$ can assumed to be constant for every n and is set to:

$$A_{n,0} \equiv 1\ . \tag{A.32}$$

Hence, the contrast of the pattern in each of the images only depends on $A_{n,1}$. Defining $\tilde{I}_1(\vec{k}_{xy})$ as reference image, comparing Eq. A.29 for different Fourier images $\tilde{I}_n(\vec{k}_{xy})$, allows to infer $A_{n,1}$ relatively to $A_{1,1}$ and thus the relative contrast of the pattern in each of the raw images $I_n(\vec{r}_{xy})$:

$$\frac{|C_{w,1}(-\vec{k}_{illu})|}{|C_{w,n}(-\vec{k}_{illu})|} = \frac{A_{1,1}}{A_{n,1}} \,, \tag{A.33}$$

and hence:

$$\begin{aligned} A_{n,1} &= f_n A_{1,1} \,, \\ f_n &:= \frac{|C_{w,n}(-\vec{k}_{illu})|}{|C_{w,1}(-\vec{k}_{illu})|} \,. \end{aligned} \tag{A.34}$$

With:

$$A_{n,m} = f_n A_{1,1}, \quad (for \quad m = -1, +1) \tag{A.35}$$

and defining the m^{th} object component $\tilde{\Omega}_m(\vec{k}_{xy})$ as:

$$\tilde{\Omega}_m(\vec{k}_{xy}) = \left[\tilde{S}(\vec{k}_{xy}) \otimes \delta(\vec{k}_{xy} - m\vec{k}_{illu})\right] \cdot \tilde{h}_{det}(\vec{k}_{xy}) \,, \tag{A.36}$$

eq. A.26 becomes:

$$\tilde{I}_n(\vec{k}_{xy}) = \sum_m A_{n,m} e^{\imath m \phi_n} \tilde{\Omega}_m(\vec{k}_{xy}) \ . \tag{A.37}$$

Introducing the matrix notation in accordance with appendix A.3:

$$\vec{\tilde{I}}(\vec{k}_{xy}) = \mathbf{M}' \, \vec{\tilde{\Omega}}(\vec{k}_{xy}) \ , \tag{A.38}$$

yields the new $N \times M$ mixing matrix:

$$\mathbf{M}'_{n,m} = A_{n,m} e^{\imath m \, \phi_n} \quad (n = 1, 2, ..., 4 \quad ; m = -1, 0, +1) \ , \tag{A.39}$$

which not only contains the pattern phase ϕ_n but also the relative pattern contrast f_n for each raw image $I_n(\vec{r}_{xy})$.

B. SETUP ALIGNMENT

Before the experiments could be conducted, the experimental setup had to be built on an optical table. The major part of this step was the alignment of the optical components. The alignment of the illumination side of the system was carried out first (see B.1). After initial experiments which showed that picoSIM works in principle (see 5.1), the four-way image splitter was assembled with the components described in 4.1.8 and aligned accordingly (see B.2). The last step was to mount the image splitter and the camera to the microscope and to align the detection side of the system (see B.3).

B.1 Alignment of the illumination side

The following paragraphs describe the individual steps of the alignment process of the illumination side. The abbreviations refer to the components described in 4.1 and depicted in Fig. 4.1. The alignment of the illumination side of the system can be divided into four different steps:

1. Modifying the Axiovert 200 M microscope stand

2. Defining the optical axis

3. Positioning the lenses

4. Positioning the $\lambda/4$-plates

Modifying the Axiovert 200 M microscope stand

In order to build the picoSIM setup it was necessary to remove the components of the original illumination path up to the filter cube from the Axiovert 200 M. Since all respective components of the illumination path are attached to one structural element, this was straightforward. Furthermore, the dichromatic beam splitter and the emission filter described in 4.1.7 were inserted in the filter cube situated in the reflector turret. The built-in Zeiss tube lens was kept in the emission path. Finally, the nano-positioner was mounted and the sample stage was elevated by means of custom-made spacers.

Defining the optical axis

Before the lenses could be positioned, the optical axis had to be defined using the illumination laser. The first step was to fix the laser at the correct height, i.e. the height that enables to couple it into the microscope. Afterwards, the position of the first lens L_1 was roughly estimated. The laser was positioned on the optical table in such a way that the laser beam could be reflected to the position of L_1 by means of two alignment mirrors (not depicted in Fig. 4.1). The mirrors (Thorlabs, USA), which can be tilted in two dimensions, enable the adjustment of the angle and the position of the laser beam as it enters the setup. Before coupling the laser beam into the microscope, the dichromatic beam splitter DB_{ill} had to be positioned in such a way that the AOI on it is 45°. The orientation of the beam splitter was chosen as described in section 4.1.7.

After the preliminary preparation the laser beam could be coupled into the microscope. The beam has to meet two important requirements to be coupled in correctly. First, it has to pass the centre of the objective's back aperture. Second, the angle under which it is incident on the back aperture has to be 0°, i.e. it has to be incident orthogonally to the aperture plane. To identify whether these alignment requirements are met, the objective was removed and substituted by an alignment target (Fig. B.1) and a mirror (Fig. B.2). Both the target and the mirror were attached to the objective's precision thread. The alignment target enables one to judge whether the beam passes the centre of the back aperture, while the mirror reveals any deviation from the

ideal AOI. If the reflected beam coincides with the incoming beam, the AOI is correct. Whether the reflected beam coincides with the incoming beam was ascertained by means of an aperture positioned in the beam path. The AOI is correct if both the incoming and the reflected beam pass the aperture. The alignment mirrors were used to adjust the beampath until both requirements are met.

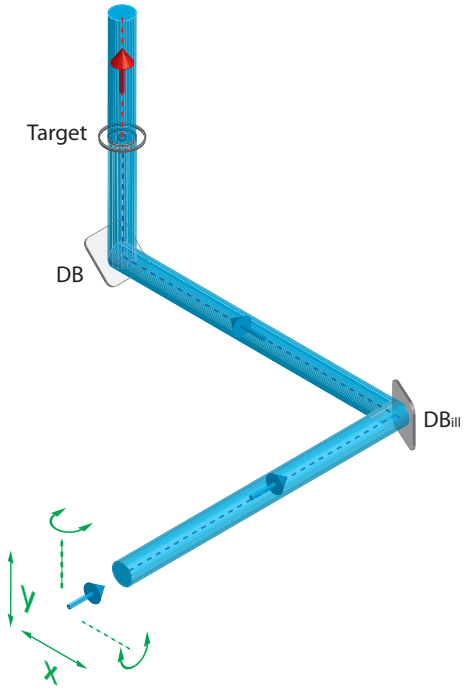

Fig. B.1: Defining the optical axis using a target: Depicted is the illumination beam path at the beginning of the alignment process at which it only consists of the two dichromatic beam splitters DB_{ill} and DB. The incoming laser beam (indicated by the blue dotted line and the blue arrows) passes a target, fixed at the objective position. The target allows one to judge whether the beam of light passes the centre of the objective thread (indicated by the red dotted line and the red arrow). Two alignment mirrors (not depicted) can be used to change both the position and the orientation of the incoming laser beam in the directions indicated by the green arrows.

The next step was to check whether the laser beam is parallel to the optical table. This is important since the degrees of freedom offered by the lens mounts is limited. Only a beam that is parallel to the table will pass the lenses orthogonally. If it turns out that the laser beam is not parallel to the table, the microscope stand must be tilted accordingly. Afterwards, the position and the AOI of the beam incident on the back

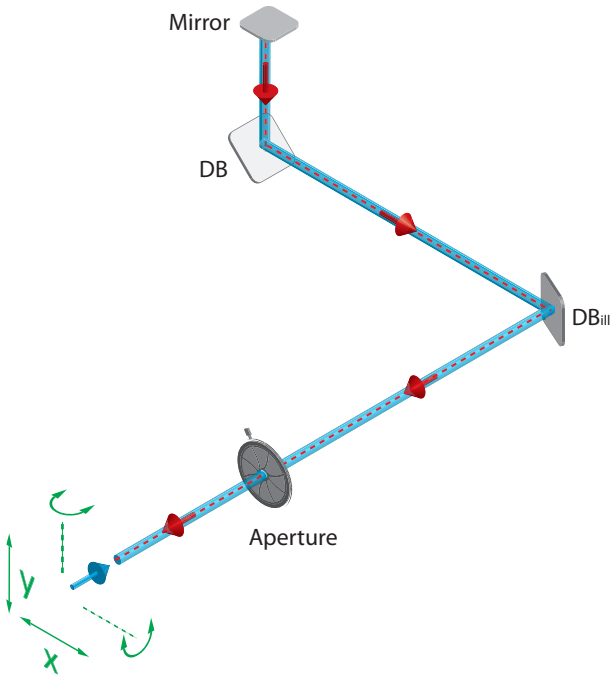

Fig. B.2: Defining the optical axis using a mirror: Depicted is the illumination beam path at the beginning of the alignment process at which it only consists of the two dichromatic beam splitters DB_{ill} and DB. The incoming laser beam (indicated by the blue arrow) is reflected by a mirror, fixed at the objective position. To judge whether the AOI of the beam of light equals 0°, a small sized aperture was positioned in the setup. Two alignment mirrors (not depicted) can be used to change both the position and the orientation of the incoming laser beam in the directions indicated by the green arrows. If the reflected beam (indicated by the red dotted line and the red arrows) passes the same aperture as the incoming beam, the AOI is correct.

aperture of the objective needs to be readapted.

Finally, two apertures with variable diameter (not depicted in Fig. 4.1) were integrated in the beam path before the position of L_1 to mark the optical axis. Due to the fact that there is only one way for a laser beam to pass through two point-like holes, the optimised beam path was defined unambiguously by this action.

After the optical axis was defined by the correctly aligned laser beam, the lenses were positioned.

Positioning of the lenses

Before positioning the lenses of the illumination side of the system, one has to make sure that the objective is at the correct z-position. Since the alignment of the setup must be optimised for the conditions present when conducting the experiments, the objective lens nano-positioner was moved to its centre position and the objective was moved to its focus position.

The first step was to move the objective out of the beam path and mark the laser spot reflected by the dichromatic beam splitter DB where it hits the ceiling of the laboratory (Fig. B.3). Afterwards, the objective was moved back to its correct position in the beam path.

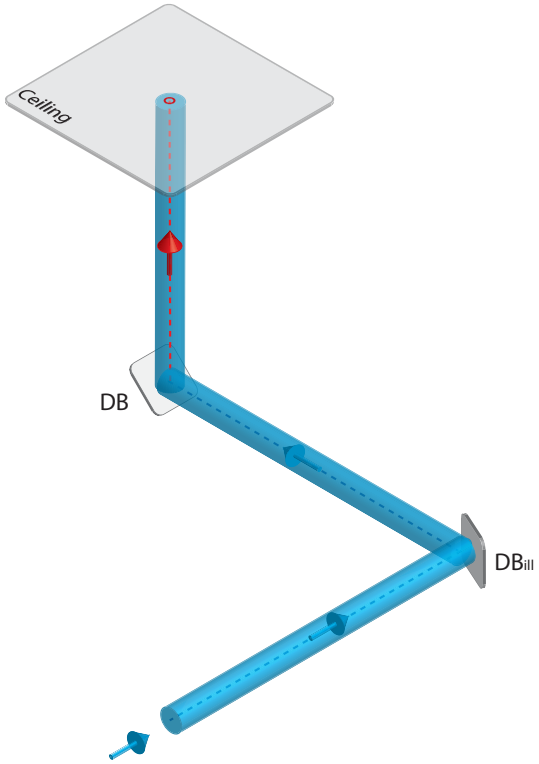

Fig. B.3: Marking of the optical axis: Depicted is the illumination beam path at the beginning of the alignment process at which it only consists of the two dichromatic beam splitters DB_{ill} and DB. After the optical axis was defined by alignment of both the AOI and the position of the incoming laser beam (indicated by the blue dotted line an the blue arrows), the position of the laser beam, reflected by DB (indicated by the red dotted line an the red arrow), was marked where it hits the ceiling.

The illumination side was aligned in reverse, i.e. the illumination tube lens L_7 was positioned first, the first lens of the setup L_1 last. There are four demands that had to be taken into account when integrating each of the lenses:

1. The incoming laser beam must pass through the lens in its centre.

2. After positioning the lens, the laser beam must still hit the spot marked on the ceiling.

3. The distance to the lens positioned prior to the actual lens must equal the sum of the focal lengths of the two respective lenses (telecentric setup).

4. The beams reflected by each spherical surface of the lens must coincide with the incoming beam.

A cage alignment plate (Thorlabs, USA) was used to ensure that the laser beam passes through the centre of the respective lens (Fig. B.4).

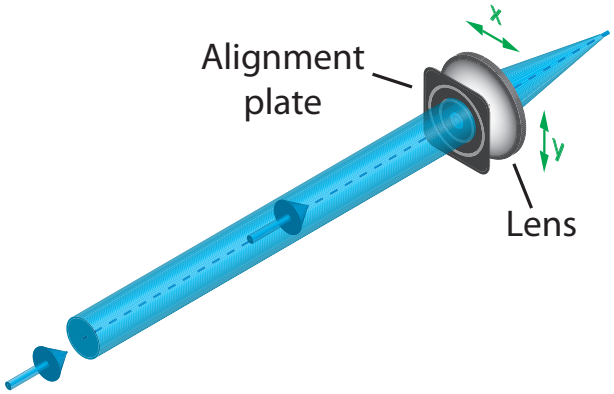

Fig. B.4: Centring of a lens: To judge whether the incoming laser beam (indicated by the blue dotted line an the blue arrows) hits the centre of the lens, an alignment plate was attached to the lens. The position of the lens in the x- and y-direction was adjusted accordingly.

If the lens was positioned correctly, the laser beam would still hit the marked spot on the ceiling. For higher precision in the x and y direction, $x-y$ translation mounts with a micrometer sensitivity were used to mount the lenses. Whether the laser beam still hits the same spot on the ceiling after positioning of a lens was judged visually. Obviously, the position of the laser beam was easier to judge when the beam emerging from the objective was collimated. This was the case after positioning of the illumination tube lens L_7 and in the following for every other lens. As the optical table and the ceiling are uncoupled, the method is difficult to accomplish when the optical table is floated. Hence, the table was defloated for the alignment process.

All lenses of the illumination side of the system were positioned in a telecentric arrangement, i.e. the distance between two consecutive lenses corresponded to the sum of their focal lengths. A shearing interferometer (Thorlabs, USA) was used to check whether two consecutive lenses were positioned correctly on the optical axis (Fig. B.5). A shearing interferometer is a device to test the collimation of a beam of light [60]. A collimated laser beam that passes two lenses will be collimated again if the two lenses are in telecentric arrangement. The shearing plate is only applicable for beam diameters that are sufficient in size. To ensure the practicality of the device, it was necessary to increase the diameter of the laser beam by means of a beam expander (not depicted in Fig. B.5). The beam expander was positioned right in front of the laser in such a way that the widened and collimated laser beam passes the two apertures inserted to define the optical axis. The beam expander was removed after the alignment process.

In order to check the angle of incidence on a lens, the diameter of one of the apertures, inserted to define the optical axis, was reduced until only a little fraction of the beam diameter, increased by the beam expander, entered the setup. The lens had to be aligned in such a way that the beam reflected by the lens passes the aperture (Fig. B.6). Due to the long distance between the respective lens and the aperture this corresponds to an AOI on the lens of approximately 0°.

The first lens to be positioned was L_7. Due to the small focal length of the objective, which caused the diameter of the emerging laser beam to be very small, it was not

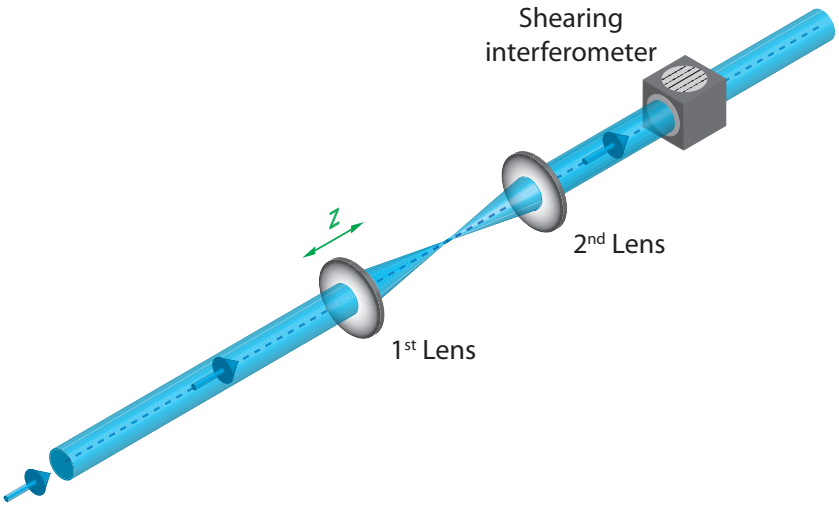

Fig. B.5: Telecentric lens arrangement: To judge whether the distance between two lenses equals the sum of their focal lengths, a shearing interferometer was used. The shearing interferometer was positioned in such a way that the incoming and collimated laser beam (indicated by the blue dotted line an the blue arrows) passes it after passing the 1^{st} and the 2^{nd} lens. Here, the 2^{nd} lens is the lens that was already aligned whereas the 1^{st} lens is in the process of alignment. The z-position of the 1^{st} lens is adjusted until the shearing interferometer indicates that it is being passed by a collimated beam of light.

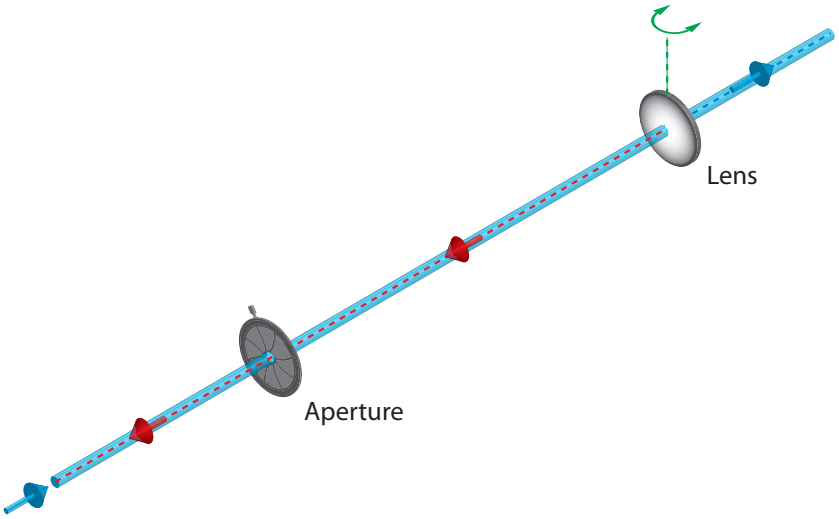

Fig. B.6: Orientation of a lens: To judge the correct orientation of a lens, an aperture was used. The incoming beam (indicated by the blue dotted line an the blue arrows) passes both the aperture and the lens. The orientation of the lens is adjusted (indicated by the green arrow) until the beam reflected by the lens (indicated by the red dotted line an the red arrows), passes the aperture as well.

possible to check its correct z-position by using the shearing interferometer as described above. Instead, the z-position of L_7 was adjusted by observing the size of the laser spot at the ceiling. The beam was assumed to be collimated when the spot size was as small as possible. The steps 1, 2 and 4 were accomplished as described above.

The remaining lenses were positioned and aligned accordingly.

Positioning of the $\lambda/4$-plates

Before the mounted $\lambda/4$-plates were positioned in the illuminating beam path, they needed to be oriented correctly. The alignment was accomplished after the polarising filter *Pol* was included in the setup and for each $\lambda/4$-plate separately. As described in 4.1.5, the angle between the incident linearly polarised light and the fast axis of the wave plate must be $-45°$ ($+45°$) to generate right-circularly (left-circularly) polarised light respectively. The labelling of the fast axis allowed for a rough estimation of the correct orientation. For higher precision, a rotatable polarising filter was positioned on the sample stage of the microscope. The light intensity beyond the polariser was measured by means of a power meter. If the orientation of the wave-plate in the beam path is correct, the light emerging on-axis from the objective will be circularly polarised. Circularly polarised light will lead to no intensity variation when rotating the polariser positioned on the sample stage. Hence, the wave-plate was oriented in such a way that rotating the polarising filter led to the least possible intensity fluctuation detected by the power meter. This procedure was conducted for each wave-plate.

The custom-made mounting device (see 4.1.5) along with the correctly aligned $\lambda/4$-plates was positioned in plane $P_{3,4}$ and $P_{5,6}$ of the setup respectively, where the 0^{th} order and all higher orders were blocked. The carriers of the mounting device were positioned in such a way that the $\pm 1^{st}$ orders pass the clear apertures of the respective wave-plate undisturbed.

B.2 Alignment of the four-way image splitter

The four-way image splitter and all its components described in this paragraph are depicted in Fig. 4.4.

The basic alignment of the image splitter was conducted before it was attached to the microscope. The alignment procedure was eased by using the alignment pinholes delivered along with the image splitter. Note that only the mirrors $M_{1a} - M_{1d}$ and $M_{2a} - M_{2e}$ and the rectangular mirrors RM_1 and RM_2 can be adjusted in all degrees of freedom. The adjustment of all other components is limited. The correct mounting of the $\lambda/2$-plate, the polarising beam splitters PBS_1 and PBS_2 and the clean up polarisers CP_{1a}, CP_{1b}, CP_{2a} and CP_{2b} was accomplished before they were included in the device.

The first step was to couple a laser into the bare device using two alignment mirrors. The first alignment pinhole AP_1 and an iris aperture screwed on the microscope mount of the image splitter were used for defining the optical axis. In particular, it was ensured that the laser beam enters the image splitter parallel to its ground plate.

Afterwards, the beam splitter BS, the mirrors $M_{1a} - M_{1d}$ and $M_{2a} - M_{2e}$, the $\lambda/2$-plate and the polarising beam splitters PBS_1 and PBS_2 were mounted and aligned using the alignment pinholes $AP_2 - AP_7$.

The next step was to position the imaging lenses L_{1b}, L_{1c}, L_{2b} and L_{2c} along with the respective clean up polarisers CP_{1a}, CP_{1b}, CP_{2a} and CP_{2b} and adjust the relative z-position of the lenses. For this purpose the light emerging from a distant tree, which was assumed to be parallel, was coupled into the image splitter. The camera was then positioned in focal distance behind L_{2b} and L_{2c} to capture the light focused by each of the lenses. The relative z-position of the lenses was optimised until the two images of the tree on the camera were simultaneously in focus. The same was accomplished for the lenses L_{1b} and L_{1c}.

To find the absolute z-position of the four imaging lenses within the image-splitter, the device was equipped with the rectangular mirrors RM_1 and RM_2 and with the prism mirrors P_1 and P_2. The four components were aligned in such a way that they reflected the light passing the lenses L_{1b}, L_{1c}, L_{2b} and L_{2c} onto the camera attached

to the camera mount of the image splitter. The z-position of the camera was adjusted until the images focused by the lenses L_{2b} and L_{2c} were in focus. With the aid of their movable mount, the z-positions of the lenses L_{1b} and L_{1c} were then optimised until all four images on the camera were in focus.

The final step was to insert the lenses L_{1a} and L_{2a}. To adjust their z-position, the rectangular aperture at the entrance of the image splitter (i.e. the intermediate image plane) was illuminated using an incoherent light source. The correct z-position of the lenses was found when the edge of the aperture RA appeared sharp on all four images on the camera.

B.3 Alignment of the detection side

After the basic alignment, the four-way image splitter and the camera were attached to the microscope.

To ensure that the emission light enters the image splitter correctly, the built-in halogen lamp of the microscope and a low magnification objective were used to image a coarse and bright sample onto the camera. Beforehand, the microscope was set up for Köhler Illumination. The sample was then viewed using the eyepiece and moved until a striking feature was situated in the centre of the field of view. The image of the sample was then inspected at the entirely opened intermediate image plane (i.e. the position of the rectangular aperture RA in Fig. 4.4). The image splitter was positioned in such a way that the system is parfocal and the striking feature is in the centre of the aperture. The last step was to position the second dichromatic beamsplitter DB_{em} (Fig. 4.1) in the emission path.

C. COMPUTER SCRIPTS

C.1 Beanshell script for the acquisition of a z-stack in μManager

```
// file location
acqName = "name";
rootDirName = "C:/name";

// number of slices
nrSlices = 20;

// distance in um between slices
distance = 0.1;

// number of channels (should be two or less)
nrChannels = 1;

// Number of timepoints
nrFrames = 1;
//// Time between timePoints (in Ms);
//intervalMs = 1100;

// clear all previous acquisitions
gui.closeAllAcquisitions();
gui.clearMessageWindow();

// get image properties
long width = mmc.getImageWidth();
long height = mmc.getImageHeight();
long depth = mmc.getBytesPerPixel();

```

```
28 // move focus device to centre position and store centre position as a
       reference to return to after acquiring the stack
29 mmc.setPosition(mmc.getFocusDevice(), 125);
30 mmc.sleep(50.0); // wait for ...ms
31 zPos = mmc.getPosition(mmc.getFocusDevice());
32
33 // Move focus device down so that the centre position will be in the
       centre of the stack
34 double basePos = zPos - (distance * (nrSlices / 2));
35 mmc.setPosition(mmc.getFocusDevice(), basePos);
36 mmc.sleep(50.0);
37
38 // prepare new acquisitions
39 gui.openAcquisition(acqName, rootDirName, nrFrames, nrChannels, nrSlices);
40
41 // open acquisition window
42 gui.initializeAcquisition(acqName, (int) width, (int) height, (int) depth)
       ;
43
44 // get exposure time and binning
45 exposure = mmc.getExposure();
46 binning = mmc.getProperty(mmc.getCameraDevice(), "Binning");
47
48 for (slice=0; slice < nrSlices; slice++) {
49
50   int frame = 0;
51   int channel = 0;
52   int counter = 0;
53
54   wait = exposure + 50;
55   gui.snapAndAddImage(acqName, frame, channel, slice);
56   mmc.sleep(wait);
57
58   pos = mmc.getPosition(mmc.getFocusDevice());
59   gui.message("Position: "  + pos);
60   double pos = pos + distance;
```

```
61    mmc.setPosition(mmc.getFocusDevice(), pos);
62    mmc.sleep(50);
63 }
64
65 // move focus device back to centre position after finishing z stack
66 mmc.setPosition(mmc.getFocusDevice(), 125);
```

D. ABBREVIATIONS AND SYMBOLS

D.1 List of abbreviations

2D:	Two-dimensional
3D:	Three-dimensional
AOI:	Angle of incidence
AOTF:	Acousto-optical tunable filter
APSF:	Amplitude point spread function
ATF:	Amplitude transfer function
BFP:	Objective's back focal plane
CCD:	Charge-coupled device camera
FAIR:	Flexible algorithms for image registration
FFT:	Fast Fourier transform
FT:	Fourier transform
FWHM:	Full width at half maximum
GFP:	Green Fluorescent Protein
hrSIM:	High resolution structured illumination microscopy
MSE:	Mean squared error
OPM	Oblique plane microscopy
OTF:	Optical transfer function
picoSIM:	Polarised illumination coded structured illumination
PSF:	Point spread function
ROI:	Region of interest
sCMOS:	Scientific complementary metaloxidesemiconductor camera
SIM:	Structured illumination microscopy

SPIM: Selective plane illumination microscopy

sSIM: Structured illumination microscopy for optical sectioning

TIRFM: Total internal reflection microscopy

D.2 List of mathematical symbols and variables

z: Coordinate along the optical axis

x, y: Lateral coordinates

k: Spatial frequency

k_{max}: Maximum frequency that can be transmitted by the microscope

d_{min}: Abbe limit of resolution

λ_{em}: Wavelength of emission light

NA: Numerical aperture of the objective lens

f^*: Complex conjugate of f

$\otimes$: Convolution operator

$h(\vec{r})$: Point spread function

$\tilde{f}$: Fourier transform of f

$\tilde{h}(\vec{k})$: Optical transfer function

$\mathbf{M}$: $N \times M$ Matrix $\mathbf{M}$

δ: Dirac delta function

$\vec{k}_{illu}$: Illumination pattern's k-vector in reciprocal sample coordinates

$\imath$: Imaginary unit

$\mathcal{F}^{-1}$: Inverse Fourier transform

d_s: Grating constant in sample space

D_s: Sampling distance

k_s: Sampling frequency

$\star_w$: Weighted cross-correlation operator

E. SETUP PARAMETERS

Parameters for the setup depicted in Fig. 4.1:

Objective:	Plan-Apochromat 100 × /1.4 Oil DIC, ∞/0.17
Effective focal length objective lens:	
	$f_{obj} = 1.645\,mm$ (as calculated)
Pupil diameter:	$D = 4.61\,mm$ (as calculated)
Laser wavelength:	$\lambda = 473\,nm$ (as specified by the supplier)
Laser beam diameter:	approximately $2\,mm$ (as measured)
Laser power:	$130mW/600mW$ (as specified by the supplier)
Grating constant:	$12.5\,\mu m$ (as specified by the supplier)
Grating constant in sample space:	
	$1.23\,\mu m$ (as calculated for the grating positioned before L_3)
	$308\,nm$ (as calculated for the grating positioned before L_5)
Focal lengths Lenses:	$f_1 = 150\,mm,\ f_2 = 30\,mm,\ f_3 = 50\,mm,\ f_4 = 200\,mm,$
	$f_5 = 50\,mm,\ f_6 = 300\,mm,\ f_7 = 200\,mm$

F. SELECTED CONFERENCE CONTRIBUTIONS

"Single-shot optical sectioning using polarised illumination coded Structured Illumination Microscopy (picoSIM)", Oral presentation at SPIE Photonics West. San Francisco, CA, February 2013.

"Single-shot optical sectioning using polarization-coded structured illumination microscopy", Oral presentation at DGMP conference on Medical Physics. Vienna, Austria, September/October 2011.

"Improving the performance of conventional structured illumination microscopy", Poster presentation at DokDok conference. Naumburg, Germany, March 2011.

Bibliography

[1] E. Hecht, *Optics*, 4th ed. (Addison Wesley, 2002).

[2] D. H. Goldstein, *Polarized Light*, 2nd ed. (Marcel Dekker, Inc., New York, 2003).

[3] M. A. A. Neil, R. Juškaitis, and T. Wilson, "Method of obtaining optical sectioning by using structured light in a conventional microscope," Opt. Lett. **22**, 1905–1907 (1997).

[4] D. Appelt and R. Heintzmann, "Structured Illumination Microscopy (SIM)," in *Encyclopedia of Biophysics*, G. Roberts, ed. (Springer, 2013).

[5] W. B. Amos, J. G. White, and M. Fordham, "Use of confocal imaging in the study of biological structures," Appl. Opt. **26**, 3239–3243 (1987).

[6] M. Minsky, "Microscopy apparatus," (1961). US patent 3013467.

[7] W. Denk, J. Strickler, and W. Webb, "Two-photon laser scanning fluorescence microscopy," Science **248**, 73–76 (1990).

[8] M. Petràň, M. Hadravsky, M. D. Egger, and G. R., "Tandem-scanning reflected-light microscope," J. Opt. Soc. Am. **58**, 661–664 (1968).

[9] R. Juškaitis, T. Wilson, M. A. A. Neil, and M. Kozubek, "Efficient real-time confocal microscopy with white light sources," Nature **383**, 804–806 (1996).

[10] A. Ichihara, T. Tanaami, K. Isozaki, Y. Sugiyama, Y. Kosugi, K. Mikuriya, M. Abe, and I. Uemura, "High-speed confocal fluorescence microscopy using a Nipkow scanner with microlenses for 3-D imaging of single fluorescence molecule in real time," Bioimages **4**, 57–62 (1996).

[11] T. Wilson, R. Juškaitis, M. A. A. Neil, and M. Kozubek, "Confocal microscopy by aperture correlation," Opt. Lett. **21**, 1879–1881 (1996).

[12] R. Heintzmann and C. Cremer, "Laterally modulated excitation microscopy: Improvement of resolution by using a diffraction grating," Proceedings of the Society of Photographic Instrumentation Engineers **3568**, 185–196 (1999).

[13] M. G. L. Gustafsson, "Surpassing the lateral resolution limit by a factor of two using structured illumination microscopy," J. Microsc. **198**, 82–87 (2000).

[14] K.-B. Im, S. Han, H. Park, D. Kim, and B.-M. Kim, "Simple high-speed confocal line-scanning microscope," Opt. Express **13**, 5151–5156 (2005).

[15] A. Vaziri and C. V. Shank, "Ultrafast widefield optical sectioning microscopy by multifocal temporal focusing," Opt. Express **18**, 19,645–19,655 (2010).

[16] D. Oron, E. Tal, and Y. Silberberg, "Scanningless depth-resolved microscopy," Opt. Express **13**, 1468–1476 (2005).

[17] J. Huisken, J. Swoger, F. D. Bene, J. Wittbrodt, and E. H. K. Stelzer, "Optical Sectioning Deep Inside Live Embryos by Selective Plane Illumination Microscopy," Science **305**, 1007–1009 (2004).

[18] H. Siedentopf and R. Zsigmondy, "Über Sichtbarmachung und Größenbestimmung ultramikroskopischer Teilchen, mit besonderer Anwendung auf Goldrubingläser," Journal de Physique Théorique et Appliquée **2**, 692–702 (1903).

[19] C. Dunsby, "Optically sectioned imaging by oblique plane microscopy," Opt. Express **16**, 20,306–20,316 (2008).

[20] K. Wicker and R. Heintzmann, "Single-shot optical sectioning using polarization-coded structured illumination," J. Opt. **12** (2010).

[21] J. W. Goodman, *Introduction to Fourier Optics* (McGraw-Hill Companies, 1968).

[22] E. Abbe, "Beiträge zur Theorie des Mikroskops und der mikroskopischen Wahrnehmung," Archiv für Mikroskopische Anatomie **9**, 413–468 (1873).

[23] B. E. A. Saleh and M. C. Teich, *Fundamentals of Photonics* (John Wiley & Sons, 1991).

[24] J. Mertz, *Introduction To Optical Microscopy* (Roberts & Company Publishers, 2010).

[25] A. Egner and S. W. Hell, "Equivalence of the Huygens-Fresnel and Debaye approach for the calculation of high aperture point-spread function in the presence of refractive index mismatch," J. Microsc. **193**, 224–249 (1999).

[26] B. Richards and E. Wolf, "Electromagnetic Diffraction in Optical Systems. I. An Integral Representation of the Image Field," Proc. R. Soc. London, Ser. A **253**, 349–357 (1959).

[27] K. Wicker, "Increasing resolution and light efficiency in fluorescence microscopy," Ph.D. thesis, King's College London, UK (2010).

[28] P. P. Ewald, "Introduction to the dynamical theory of X-ray diffraction," Acta Crystallogr., Sect. A **25**, 103–108 (1969).

[29] C. W. McCutchen, "Generalized aperture and the three-dimensional diffraction image," J. Opt. Soc. Am. **54**, 240–244 (1964).

[30] L. Rayleigh, "Investigations in optics with special reference to the spectroscope," Philosophical Magazine **8**, 261 (1879).

[31] C. M. Sparrow, "On spectroscopic resolving power," Astrophysical Journal **44**, 76–86 (1916).

[32] R. Heintzmann, T. M. Jovin, and C. Cremer, "Saturated pattern excitation microscopy - a concept for optical resolution improvement," Opt. Soc. Am. A **19**, 1599–1609 (2002).

[33] M. G. L. Gustafsson, "Nonlinear structured-illumination microscopy: Wide-field fluorescence imaging with theoretically unlimited resolution," Proc. Natl. Acad. Sci. **102**, 13,081–13,086 (2005).

[34] E. H. Rego, L. Shao, J. J. Macklin, L. Winoto, G. A. Johansson, N. Kamps-Hughes, M. W. Davidson, and M. G. L. Gustafsson, "Nonlinear structured-illumination microscopy with a photoswitchable protein reveals cellular structures at 50-nm resolution," Proc. Natl. Acad. Sci. U. S. A. **109**, E135–E143 (2012).

[35] W. Singer, M. Totzeck, and H. Gross, *Handbook of Optical Systems*, vol. 2 (Wiley-VCH, 2005).

[36] J. R. Lakowicz, *Principles of Fluorescence Spectroscopy*, 4th ed. (Kluwer Academic/Plenum Publishers, 1999).

[37] J. R. Lakowicz, I. Gryczynski, Z. Gryczynski, E. Danielsen, and M. J. Wirth, "Time-resolved fluorescence intensity and anisotropy decays of 2,5-diphenyloxazole by two-photon excitation and frequency-domain fluorometry," **96**, 3000–3006 (1992).

[38] A. L. Mattheyses, M. Kampmann, C. E. Atkinson, and S. M. Simon, "Fluorescence Anisotropy Reveals Order and Disorder of Protein Domains in the Nuclear Pore Complex," Biophys. J. **99**, 1706–1717 (2010).

[39] R. Swaminathan, C. P. Hoang, and A. S. Verkman, "Photobleaching recovery and anisotropy decay of green fluorescent protein GFP-S65T in solution and cells: cytoplasmic viscosity probed by green fluorescent protein translational and rotational diffusion," Biophys. J. **72**, 1900–1907 (1997).

[40] M. G. L. Gustafsson, L. Shao, P. M. Carlton, C. J. R. Wang, I. N. Golubovskaya, W. Z. Cande, D. A. Agard, and J. W. Sedat, "Three-dimensional resolution doubling in wide-field fluorescence microscopy by structured illumination," Biophys. J. **94**, 4957–4970 (2008).

[41] R. Heintzmann and K. Wicker, "Imaging system," (2010). WO patent 2010128307.

[42] S. Hwang and Y. Lee, "Simulation of an oil immersion objective lens: A simplified ray-optics model considering Abbes sine condition," Opt. Express **16**, 363–370 (2008).

[43] R. Fiolka, L. Shao, E. H. Rego, M. W. Davidson, and M. G. L. Gustafsson, "Time-lapse two-color 3D imaging of live cells with doubled resolution using structured illumination," Proc. Natl. Acad. Sci. USA **109**, 5311–5315 (2012).

[44] R. Heintzmann, "Band limit and appropriate sampling in microscopy," in *Cell biology: a laboratory handbook*, J. E. Celis, ed. (Elsevier, 2006).

[45] J. M. Zwier, G. J. Van Rooij, J. W. Hofstraat, and G. J. Brakenhoff, "Image calibration in fluorescence microscopy," J. Microsc. **216**, 15–24 (2004).

[46] D. O. Fürst, M. Osborn, R. Nave, and K. Weber, "The organization of titin filaments in the half-sarcomere revealed by monoclonal antibodies in immunoelectron microscopy: a map of ten nonrepetitive epitopes starting at the Z line extends close to the M line," J. Cell. Biol. **106**, 1563–1572 (1988).

[47] J. Messerli, M. E. Eppenberger-Eberhardt, B. M. Rutishauser, P. Schwarb, P. von Arx, S. Koch-Schneidemann, H. M. Eppenberger, and J. C. Perriard, "Remodelling of cardiomyocyte cytoarchitecture visualized by three-dimensional (3D) confocal microscopy," Histochemistry **100**, 193–202 (1993).

[48] A. Edelstein, N. Amodaj, K. Hoover, R. Vale, and N. Stuurman, "Computer control of microscopes using μ-Manager," Curr. Protoc. Mol. Biol. **14**, 1–7 (2010).

[49] P. Niemeyer, "Beanshell," (2008). URL `http://www.beanshell.org`.

[50] "DIPimage," URL `http://www.diplib.org`.

[51] J. Modersitzki, *FAIR: Flexible Algorithms for Image Registration* (SIAM publications, 2009).

[52] K. Wicker (2012). Private communication.

[53] R. Penrose, "A generalized inverse for matrices," P. Camb. Philos. Soc. **51**, 406–413 (1955).

[54] K. Wicker, O. Mandula, G. Best, R. Fiolka, and R. Heintzmann, "Phase optimisation for structured illumination microscopy," Opt. Express **21**, 2032–2049 (2013).

[55] S. A. Shroff, J. R. Fienup, and D. R. Williams, "Phase-shift estimation in sinusoidally illuminated images for lateral superresolution," J. Opt. Soc. Am. A **26**, 413–424 (2009).

[56] D. Axelrod, "Fluorescence Polarization Microscopy," in *Methods in Cell Biology*, D. L. Taylor and W. Y. L, eds., pp. 333–325 (Academic Press Inc., 1989).

[57] C. Vetter, "Femtosecond-Laser induced nanogratings in fused silica - a versatile platform for birefringent polarization control," Master's thesis, Friedrich Schiller University Jena, Germany (2012).

[58] O. Mandula, "Pattern excitation microscopy," Master's thesis, Charles University Prague, CZ & King's College London, UK (2008).

[59] N. Wiener, *Extrapolation, Interpolation and Smoothing of Stationary Time Series with Engineering Applications* (The MIT Press, Cambridge (Mass.); Wiley and Sons, New York; Chapman & Hall, London, 1949).

[60] W. C. Sweatt, "Rotatable shear plate interferometer," Opt. Eng. **29**, 1157–1160 (1990).